The Pennsylvania State University

The Graduate School

Department of Energy and Mineral Engineering

UNDERSTANDING HYDROLOGICAL AND GEOCHEMICAL CONTROLS ON SOLUTE CONCENTRATIONS AT LARGE SCALE

A Dissertation in

Petroleum and Natural Gas Engineering

by

Chen Bao

Submitted in Partial Fulfillment

of the Requirements

for the Degree of

Doctor of Philosophy

May 2016

The dissertation of Chen Bao was reviewed and approved* by the following:

Li Li
Associate Professor of Petroleum and Natural Gas Engineering
Dissertation Co-advisor
Chair of Committee

Susan Brantley
Distinguished Professor of Geosciences
Dissertation Co-advisor

Turgay Ertekin
Professor of Petroleum and Natural Gas Engineering
Head of Department of Energy and Mineral Engineering

Derek Elsworth
Professor of Energy and Geo-Environmental Engineering

Christopher Duffy
Professor of Civil and Environmental Engineering

*Signatures are on file in the Graduate School

ABSTRACT

The spatiotemporal variations in solute concentrations within a watershed can provide valuable understandings on the hydrogeochemical processes in the system, e.g. the residence time of the water, retention of contaminants and weathering rates of minerals. However, such understandings are often prevented by the complexities in the process coupling and challenges in modeling such couplings at watershed scale.

This dissertation presents an integrated approach to study this system. A fully coupled finite volume hydrological, land surface and reactive transport model: RT-Flux-PIHM has been developed. Based on Flux-PIHM, which simulates the terrestrial water cycle and the surface energy balance, the additional RT module explicitly models mass transfer and geochemical reactions, including mineral dissolution, precipitation, and ion exchange. As such, RT-Flux-PIHM is the first numerical model that provides the integration of land surface, hydrological, mass transfer and biogeochemical reaction at large scale.

The model was verified and then applied at the Susquehanna Shale Hills watershed (0.08 km^2), a National Science Foundation (NSF) Critical Zone Observatory (SSHCZO). Based on existing conceptual framework on major hydrogeochemical processes and extensive measurements at the site (Herndon et al., 2015; Jin et al., 2011a), RT-Flux-PIHM reproduces the spatiotemporal evolution of solute concentrations which matched field observations.

The chloride concentration is controlled by inputs from rain and the hydrological connectivity of watershed. The watershed is well connected in the wet seasons, which allows fast flushing of chloride. In contrast, the less connected watershed in the summer sees “trapping” of chloride in less connected area. Large rainfall events connect the whole watershed and wash out these “old water” pockets of high Cl concentrations – however, by the time the water emits at the

stream mouth it is diluted significantly. This seasonal change in hydrological connectivity at the watershed scale essentially regulates the chloride concentration.

Existing studies show the slope of the log-log concentration discharge (CQ) plot of chloride is ranging from 0 to -0.25 however it is unclear what controls the variations. Numerical experiments are conducted to elucidate the hydrological controls on the Cl CQ relationship. The chemostasis of chloride is dependent on the capability of the watershed to effectively mitigate the concentration variations induced by transition between source waters, e.g., from valley floor and swale subsurface flow to upslope subsurface flow, or from subsurface flow to deeper groundwater flow. Larger water storage leads to more chemostatic behavior while larger precipitation level and coarser soil both lead to stronger dilution behavior. However, transport parameters such as macro pore conductivity changed the Cl CQ slope only marginally.

Mg concentrations, however, are regulated by the interplay between clay dissolution and groundwater influx as sources and discharge as sink while ion exchange acts as the storage buffer. Faster clay dissolution in the wet season with more abundant water is accompanied by more diluted groundwater influxes to the stream at the mouth by more discharge. In the dry summer, the slower clay dissolution is accompanied by less diluted groundwater influxes at the stream mouth and lower discharge. Cation exchange buffers the Mg concentration by storing tens of times higher Mg on exchange sites than in pore water. Large rainfall events flush out significant amount of stored Mg on the exchange sites while also diluting the waters, leading to similar Mg concentrations in the stream waters in large and small rainfall events. In general, the multiple processes work together to generate the relatively consistent concentrations for both solutes.

In sum, the development of RT-Flux-PIHM enables studies on the hydrogeochemical dynamics at large scale, offering process-based modeling that integrates different processes while at the same time can separate and interrogate the importance of each mechanism.

TABLE OF CONTENTS

Chapter 1 Introduction 1

Chapter 2 Development of RT-Flux-PIHM 9

1. Introduction 9
2. Development of RT-Flux-PIHM 13
    2.1 Model Structure Overview 13
    2.2 The Land-surface Module Noah Land Surface Model 16
    2.3 The Hydrological Module PIHM 18
    2.4 Reactive Transport Processes in RT 20
    2.5 Numerical Implementation 24
3. Model Verification 26
4. Model Demonstration 29
5. Conclusion 35
6. Numerical Treatment of RTM 36
    6.1 Mass Action Law 36
    6.2 Debye–Hückel Model For Species Activity 38
    6.3 Influences of Temperature on Kinetic Reactions 39
    6.4 Finite Volume Based Reactive Transport Model 39
    6.5 Sequential Non-Iterative Approach (SNIA) 42
    6.6 Local Jacobian Matrix for Kinetic Reactions 44
    6.7 Speciation For Equilibrium Controlled Reactions 46
    6.8 Total Variation Diminishing 49
    6.9 Adaptive time stepping 50
    6.10 Code Structure in RT 50

Chapter 3 Decoding Concentration-discharge Relationship of Chloride and Magnesium at the Shale Hills Critical Zone Observatory 52

1. Introduction 53
2. The Model, the Site, and Data-Model Integration 57
3. Hydrological and Geochemical Processes in SSHCZO 62
    3.1 Hydrological processes in 2009 62
    3.2 Transport of the non-reactive tracer chloride 64
    3.3 Reactive Transport of Magnesium 65
4. Results 71
    4.1 Chloride 71
    4.2 Magnesium 76
5. Discussion 86
6. Conclusions 89

Chapter 4 Hydrological Controls on the Chloride Concentration Discharge Relationship 92

1. Introduction 92
2. Method 95

2.1 Shale Hills Critical Zone Observatory (SSHCZO) 95
2.2 RT-Flux-PIHM model 98
2.3 Dynamic End-Member Mixing Analysis (dEMMA) 99
2.4 Watershed Box Model 101
2.5 Hydrological Connectivity 103
2.6 Sensitivity Analysis 104
3. Results and Discussions 106
3.1 Watershed Connectivity and the Role of Big Precipitation Events 106
3.2 Stream Chloride Concentration 110
3.3 Hydrological Connectivity and $[Cl]_D$-Q_D relationship 115
4. Sensitivity Analysis 116
4.1 Soil Porosity 116
4.2 Soil Van Genuchten Parameter β 119
4.3 Macropore Conductivity K_{mac} 122
4.4 Precipitation 123
5. Conclusion 124

Chapter 5 Summary 126

Chapter 6 Future Research 130

Appendix A User Manual of RT-Flux-PIHM 133

1. Introduction to the input files of RT-Flux-PIHM 133
2. Input File Format 134
2.1 projectName.txt 134
2.2 *.chem 134
2.3 *.cdbs 140
2.4 *.cini 140
2.5 *.prep 140
3. Output File Format 142
3.1 *.conc 142
3.2 *.btcv and *index.btcv files 143
3.3 *.vol 143

Appendix B RT source code details 144

1. Data Structure and Library <rt.h> 144
2. RT component main code <rt.c> 145
3. Transport functions <os3d.c> 146
4. Reaction Functions <react.c> 146

Appendix C Examples of RT-Flux-PIHM Input Files 149

1. Chloride Non-Reactive Transport 149
2. Magnesium Reactive Transport 153

LIST OF FIGURES

Figure 1-1 “Rapid mobilization of old water”: a) rainfall and stream discharge b) chloride concentration in stream and in rainwater for Tanllwyth stream at Plynlimon, Wales. Stream discharge is responsive to rainfall events, however chloride concentration is largely unaffected by rainfall event and rainwater chloride concentration, although chloride is controlled by rainfall input. Figure from (Kirchner, 2003) 2

Figure 1-2 “Variable chemistry of old water”: Semilog plots of concentrations of reactive species as functions of stream discharge at Upper Hore stream at Plynlimon, Wales. Concentrations of reactive species are dependent on stream discharge, but such relationship varies among different species. Figure from (Kirchner, 2003) 3

Figure 2-1 Processes included in RT-Flux-PIHM. Flux-PIHM simulates the hydrological and land surface dynamics (precipitation, canopy interception, infiltration, recharge, overland flow, subsurface lateral flow, river flow, and surface energy balance) at the watershed scale using the finite volume method. The RT module takes the water output from Flux-PIHM and simulates the multi-component reactive transport processes, allowing hydrological and geochemical coupling. The discretized mesh structure for the Susquehanna Shale Hills Critical Zone Observatory (SSHCZO) is depicted at the bottom. Geochemical processes, including mineral dissolution and precipitation, ion exchange, surface complexation, and aqueous complexation, are included in the RT module. 13

Figure 2-2 Input, output, and process coupling within RT-Flux-PIHM. The Flux-PIHM module solves the hydrological and land surface dynamics. The RT module reads flow and water distributions from Flux-PIHM and specified initial chemistry of water and solid phases, and outputs the spatial and temporal evolution of aqueous and solid phase compositions based on the hydrological conditions and geochemical thermodynamics and kinetics. 14

Figure 2-3. RT-Flux-PIHM is a data-intensive model intended to investigate the multi-physics interactions at watershed scale. Five types of input files are required: initial conditions, boundary conditions, static inputs, forcing data and calibration files. In additional to data required by Flux-PIHM, RT module need initial geochemical conditions, reaction network, geochemical database, and forcing chemistry to simulate the geochemical processes. 16

Figure 2-4. Comparison of results from RT and CrunchFlow. A: spatial distribution of solutes on day 2 (half residence time) for advection-only case. B: breakthrough curves (BTC) for advection-only case. RT and CF generated almost identical results except for slight difference at the sharp concentration front. Magnesium originally in the column was all adsorbed onto surface sites so no magnesium broke through at the outlet before 1.9 days. The sharp front suggests good remediation of numerical dispersion. C: spatial distribution of solutes on day 2 in the case with advection, diffusion and dispersion. D: breakthrough curves for the case with advection,

diffusion and dispersion. RT and CF generated essentially identical solutions in both cases. 28

Figure 2-5. Spatial distribution of key topographic and soil properties in SSHCZO based on extensive field surveys and existing modeling work calibrated by using multivariate field measurements. A: depth to bedrock [m]; B. surface elevation [m]; C: identified soil series; D: Zones of different geochemical initial conditions assigned based on field measurements (Jin et al., 2010). 30

Figure 2-6 At selected time (before, during and after the rainfall event under investigation), . A: water storage h_u in the unsaturated zone [m^3/m^2]; B: water storage h_g in the saturated zone [m^3/m^2]; C: [Cl] [μmol/L-pore water]; D: chlorite dissolution rate [μmol/g-soil/d]; E: [Mg] in pore water for w/ CEC case [μmol/L-pore water]; F: Mg on exchange sites, w/ CEC case [μmol/L-pore water]; G: [Mg] in pore water for w/o CEC case [μmol/L-pore water]. 32

Figure 2-7. Predicted discharge, concentrations, and fluxes as a function of time during a large rainfall event on oct. 24, 2009. A: discharge and [Cl], [Mg] (w/ CEC and w/o CEC) at the stream outlet. B: solute outflux as a function of time. 33

Figure 2-8. CQ hysteresis plots from hourly output of RT-Flux-PIHM simulation from Oct. 22 to 26, 2009, when a large precipitation event occurred on Oct. 24. Black arrows indicate the rising limb (arrow pointing to the right) and recession limb (arrow pointing to the left). 34

Figure 2-9 A polyhedron 42

Figure 2-10 Schematic plot of Gupta TVD for unstructured grid 49

Figure 2-11 Flow chart of RT-Flux-PIHM. [**h**] is the vector of water storages in the field; [**T**] is the vector of temperature in the field. [**C**] is the vector of primary species concentration in the field; [**U**] is the vector of total species concentration in the field. A nested Newton Raphson iteration is performed to solve for concentration evolution resulted from reactions. 51

Figure 3-1 A schematic of processes that are incorporated in different modules (shown in different colors) in RT-Flux-PIHM. The model allows systematic understanding of rates and fluxes at the pedon, hillslope, and watershed scales. The watershed, Shale Hills, is located within the Susquehanna Shale Hills Critical Zone Observatory (SSHCZO). 57

Figure 3-2 Topography of the extensively instrumented SSHCZO. Here we only show the sampling points where key hydrological and geochemical measurements were used in this work. Stream discharge measured at the weir (white square, data available from 2006 to 2012) and the groundwater table depth measured at the groundwater well in the stream riparian zone (grey square, data available from 2007 to 2013) were used to calibrate the land surface hydrological component of the coupled model for 2009 (Duffy, 2013). Water chemistry was measured at 1) lysimeter nests

at the south planar sites -- valley floor (SPVF), middle slope (SPMS) and ridge top (SPRT) (data available from Apr. 1st 2008 to Oct. 20th 2011), and at south swale sites -- valley floor (SSVF), middle slope (SSMS) and ridge top (SSRT) (data available from Nov. 9th, 2007 to Oct. 20th, 2011); 2) stream water in the weir at the stream mouth (data available from Oct. 20th, 2006 to Feb. 18th 2011) (Brantley and Sullivan, 2014; Brantley, 2013b, a; Brantley, 2013f, d, e, c; Brantley, 2013g). Measured soil water chemistry was used to calibrate the reactive transport model. The swales are hillslope zones of convergent flow whereas the planar hillslopes are zones of non-convergent flow. 59

Figure 3-3 Data sources and the structure of data-model integration. The yellow box indicates data from a national database, and the green box indicates data from measurements. Font color indicates connections between data and model. For example, orange colored data provide input or constraints on the orange-colored land surface model. Similarly, the blue colored and brown-colored data are input and/or constraints for the hydrological and reactive transport models with corresponding colors. 60

Figure 3-4 A: Temporal evolution of measured daily precipitation [m/d], simulated discharge normalized by watershed area [m/d] and simulated total ET [m/d]. B: Temporal evolution of simulated net watershed water storage in the saturated and unsaturated zones [m^3/m^2](Shi et al., 2013a). Here daily water storages, a measure of water content, indicate similar total precipitation across different seasons however higher ET in the summer, leading to wetter watershed (higher water storage) in spring and winter and dry watershed (lower water storage) in the summer..... 63

Figure 3-5 Temporal evolution of average chloride data (open circles) and modeling output (red lines) from Apr. 1st to Dec. 31st, 2009. A: concentrations at the stream mouth; B through G: concentrations in 6 lysimeter sites, including the 3 South Planar sites (SPRT, SPMS, SPVF) and 3 South Swale sites (SSRT, SSMS, SSVF) (Figure 3-2). Grey areas indicate ±one standard deviation for the measured pore water chemistry. 71

Figure 3-6 Spatial profiles in April, August, and December in 2009. A: water saturation (soil moisture) in the unsaturated zone [m^3/m^3]; B: water storage h_g in the saturated zone [m^3/m^2]; C: depth from ground surface to water table (DWT) [m]; D: local Cl concentration in pore water [μmol/L] (calculated as a volume weighted average over the saturated and unsaturated zones); Chloride concentrations are lower in or near the valley floor and swales where water is more abundant and connected to the stream. E: Chloride total mass (pore water volume × Cl concentration) over the entire watershed, daily chloride influx from the throughfall and outflux (discharged, C×Q) [mol/d]. 74

Figure 3-7 CQ relationships for measured and predicted chloride in 2009. The grey diagonal line indicates a CQ relationship if simple dilution dominates the system. 76

Figure 3-8 A. Temporal evolution of modeled and measured magnesium concentrations in stream water (A). (B-G) Temporal evolution of modeled and measured pore water

Mg concentration in different sampling locations, including the 3 South Planar sites (SPRT, SPMS, SPVF) and 3 South Swale sites (SSRT, SSMS, SSVF). 78

Figure 3-9 A: Predicted spatial distribution of chlorite dissolution rate [μmol/g/d] on Apr. 1st, Aug. 1st and Dec. 1st, 2009; B: Temporal evolution of the watershed-average dissolution rate of and chlorite [μmol/g/d] and watershed-average total water storage in saturated and unsaturated zones [m^3/m^2]. Watershed-averaged dissolution rates were calculated from the change per day in the mineral mass (μmol) in the entire SSHCZO (normalized by the total mass (g) of each mineral in SSHCZO). 79

Figure 3-10 Total water storage, wetted surface area, dissolution rates, and average [Mg] at the watershed scale as a function of discharge. The dissolution rates rise proportionally with the discharge, water storage, and wetted surface area, leading to larger dissolved Mg mass. This increase in dissolved Mg flux however is counterbalanced by larger total water storage, leading to relatively constant average [Mg] at the watershed scale. 80

Figure 3-11 A: spatial profiles of [Mg] in pore water [μmol/L]; B: [Mg] on exchange sites μmol/g]; C: Daily input (bottom solid lines) from rain water (blue), clay dissolution (black), groundwater (green), and output fluxes from stream discharge (red, C×Q, mol/d). Mg primarily comes from dissolution and GW influx, while discharge flushes out Mg, especially in big rainfall events. D: Mg mass evolution: Mg mass in pore water (solid black line) and on exchange sites (solid green line) calculated by summing up Mg mass over the entire watershed. Total Mg is the sum of Mg in pore water and on exchange site. The exchange sites store an order of magnitude more Mg mass than pore water. 81

Figure 3-12 Comparison of data (circles) and model prediction of stream outlet Mg concentration in 4 scenarios: dissolution only (dashed green), dissolution with cation exchange (solid green), dissolution with groundwater influx (dashed red), dissolution with both GW and CEC (solid red, best fit case shown in figure 8). 83

Figure 3-13 Effects of three important parameters in determining the CQ relationship for Mg. A: The effect of varying specific surface area (SSA) without including the groundwater (GW) influx. B: Effect of varying cation exchange capacity (CEC) without including GW influx. C: Same as A except including a GW influx. The red dots are output from the best fit model with GW and with SSA and CEC in the base case (1X SSA and 1X CEC). D: Same as B except including the GW influx. 84

Figure 3-14 Schematics of different controls on determining the chemostasis of CQ in stream water. When the dissolution flux ($Flux_D$, light and aqua blue) is much larger than the Mg flux from the ground water ($Flux_G$, dark blue color), chemostasis is more likely to occur because mass flux from clay dissolution increase proportionally to water volume and Q . When $Flux_D << Flux_G$, dilution is more likely to occur because of the constant, unresponsive groundwater influx to hydrological events. 87

Figure 4-1. Spatial distribution of key topographic and soil properties in SSHCZO based on extensive field surveys and existing modeling work calibrated by using

multivariate field measurements (Jin et al., 2010; Lin, 2006; Shi et al., 2013b): A, depth to bedrock [m]; B, surface elevation [m]; C, identified soil series; D, soil average effective porosity in each element [m^3/m^3]. 96

Figure 4-2 Schematic plot of the three methods used in this work. Left: Finite volume based distributed RT-Flux-PIHM model that simulates the coupled hydrological land surface process and the non-reactive transport of chloride. Middle: Dynamic end-member mixing analysis (dEMMA) where end-members are mixed at the stream outlet. (Q_S, $[Cl]_S$) are the flow rate [$m^3/(m^2d)$] and concentration [mol/m^3] of surface runoff; (Q_L, $[Cl]_L$) are the flow rate [$m^3/(m^2d)$] and concentration [mol/m^3] of subsurface flow; (Q_G,$[Cl]_G$) are the flow rate [$m^3/(m^2d)$] and concentration [mol/m^3] of deeper groundwater influx. Right: Watershed scale "box" model where end-members are mixed in a simplified linear reservoir. (Q_E, $[Cl]_E$) are the rate [$m^3/(m^2d)$] and concentration [mol/m^3] of evapotranspiration; (Q_P, $[Cl]_P$) are the flow rate [$m^3/(m^2d)$] of precipitation and throughfall concentration [mol/m^3]; (Q_G,$[Cl]_G$) are the flow rate [$m^3/(m^2d)$] and concentration [mol/m^3] of deeper groundwater influx. Q_D [$m^3/(m^2d)$] is the discharge and [Cl] [mol/m^3] is the chloride concentration in discharge and in the linear reservoir. 98

Figure 4-3 A: water storage in the saturated zone (m^3/m^2); the saturated zone in subsurface drives lateral flow velocity based on Darcy's law; B: velocity of lateral saturated zone flow from RT-Flux-PIHM in logarithm color scale. White arrows indicate the directions of the lateral flows. Most saturated zone flows are directed towards the nearest stream or swales. Lateral flows on ridges are often directly flowing along the ridge towards the outlet of the stream; C: spatial pattern of flow velocities when 75^{th} percentile velocity was used as a threshold; D: [Cl] concentration in the subsurface; E: omnidirectional connectivity as a function of separation (distance between grid blocks) at different times and the corresponding integral connectivity scale (I_{CS}) [m]; F: I_{CS} and precipitation as a function of time. The I_{CS} here is in logarithmic scale. The three dates selected here has no significant preceding rainfall events to exclude the impact of preceding rainfalls. Sudden increase in hydrological connectivity correlates to big rainfall events. 107

Figure 4-4 A: water storage in the saturated zone [m^3/m^2], which drives lateral flow velocity based on Darcy's law in RT-Flux-PIHM; B: velocity of lateral saturated zone flow in logarithm color scale; The white arrows indicate the directions of the lateral flows. C: spatial pattern of flow velocity when 75^{th} percentile velocity was used as a threshold; D: [Cl] concentration in the subsurface; F: I_{CS} [m] and precipitation as functions of time. 109

Figure 4-5 A: contributions of different flow types to the stream as functions of time for dynamic EMMA method, flow rates are from RT-Flux-PIHM simulation. B: stream chloride concentration in data and calculated based on the dynamic EMMA method, together with chloride concentrations in different flows. C: stream chloride concentration predicted by RT-Flux-PIHM and by dEMMA with actual data. 111

Figure 4-6 A: Inputs, outputs and storage of watershed in the watershed box model. The inputs include precipitation Q_P [$m^3/(m^2d)$] and deeper groundwater influx Q_G

[$m^3/(m^2d)$]. The outputs include stream discharge Q_D [$m^3/(m^2d)$] and evapotranspiration Q_E [$m^3/(m^2d)$]. The input and output fluxes are in logarithmic scale. The storage of linear reservoir h [m^3/m^2] (grey curve) drops in summer due to elevated evapotranspiration. B: The stream discharge $[Cl]_D$ in data and calculated based on RT-Flux-PIHM, and based on watershed box model, together with chloride concentrations in different flows. 114

Figure 4-7 $[Cl]_D$-Q_D relationship under high (I_{CS}>10m, blue circles) and low (I_{CS}≤10m, red circles) watershed hydrological connectivity. Simple linear regression statistics are performed for all data points, the high connectivity periods and low connectivity periods. 115

Figure 4-8 Under five different effective porosity conditions, the actual porosity in the field is equal to the GCC multiplies the base case soil porosity distribution, A: contributions of different flows to the stream; B: temporal evolution of I_{CS} [m] in logarithmic scale, evaluated based on hydrological connectivity function using the base case 75 percentile lateral subsurface flow as thresholds (0.18 m/d), the median of I_{CS} is also reported on plot; C: temporal evolution of $[Cl]_D$ (data and RT-Flux-PIHM simulation), $[Cl]_S$, $[Cl]_L$ and $[Cl]_G$; D: log-log plot of $[Cl]_D$-Q_D relationships, slopes *a* for simple linear regressions of each trendline (black for all data, red for low connectivity phase and blue for high connectivity phase) are also reported on plots. 116

Figure 4-9 Slopes *a* for high connectivity phases in different porosity conditions are linearly correlated to the median I_{CS}. 118

Figure 4-10 Same as figure 4-8, but under different soil Van Genuchten β conditions manipulated by varying GCC for β. 120

Figure 4-11 Slopes *a* for high connectivity phases in different β conditions are linearly correlated to the median I_{CS}. 121

Figure 4-12 Same as figure 4-8, but under different soil K_{mac} conditions. 122

Figure 4-13 Same as figure 4-8, but under different precipitation conditions 123

Figure 5-1 Spatial patterns of soil organic carbon storage (A) and the frequency of being hydrological connected (B). A is adapted from (Andrews et al., 2011) 131

LIST OF TABLES

Table 2-1 Reactions and thermodynamic and kinetic parameters (Wolery, 1992) 27

Table 2-2 Simulation Conditions 27

Table 2-3 Chemical conditions 27

Table 2-4 Reactions and reaction thermodynamics and kinetics 30

Table 2-5 Compatibility of Spatial Discretization Methods In A Coupled System 41

Table 3-1 Key reactions in the model and their kinetic and thermodynamics parameters 68

Table 3-2 Initial pore water chemistry and mineral compositions used in simulations 69

Table 3-3. The total bias* (%) between model output and measured concentrations. 72

Table 3-4 Average Mg concentrations and slope of CQ curve 85

Table 4-1 RT-Flux-PIHM model parameters for the SA, their a priori values and ranges of plausible GCCs. The references are 1) (Beven and Binley, 1992) 2) (Gupta et al., 1999) 3) (Anderton et al., 2002) 4) (Tang et al., 2006) 5) (Shi et al., 2013c) 104

Table 4-2 List of GCC values in single parameter SA test 105

ACKNOWLEDGEMENTS

I would like to express my deepest gratitude to Dr. Li Li for her guidance, understanding, patience, and support during my graduate studies at Penn State. In retrospect, I feel extremely lucky to have her as my mentor and Ph.D. advisor. When I was attempting to change my research topic during my second year, despite all the adverse effects that she faced, she tried her best to understand my motivation and made great efforts for me to continue working on another research project that fit my long term career goals, which leads to this dissertation. Her mentorship was paramount in both my research and my life. She is a great mentor, not just in how to do research, but also in how to be an effective communicator, how to connect to people and how to improve oneself in general. She is also a role model in working ethics and in interpersonal relationship. I owe her a debt of gratitude for everything she had done for me and I sincerely hope I won't disappoint her in the future.

I would like to thank the members of my doctoral committee for their input, valuable discussions and accessibility. Dr. Brantley has been both a conscious quality control inspector and an enthusiastic cheerleader. Dr. Ertekin prepared me with the foundations of numerical simulation. Dr. Elsworth has always been kind and encouraging. Dr. Duffy has been giving me many helpful and constructive advices, pointing me to numerous useful literatures, models and numerical techniques. This work will not be possible if not for all those helps.

I would like to thank the department of Energy and Mineral Engineering for the quality, width and depth of my Ph.D. education. The Petroleum and Natural Gas Engineering faculties have been great resources for me throughout these years. Dr. Ertekin is very professional and effective in his teaching. He is always kind, caring and humorous, which flattened the learning curves significantly. Dr. Ayala is the most enthusiastic professor I have ever seen and his teaching philosophy has always been an inspiration.

I would also like to thank all the members of the Dr. Li's research group. Hongfei Wu has been a great resource when I started C programming. Fatemeh and her husband Safa were always patient and helpful to me in the laboratory and in the office. It has been great pleasure working with Changhe Qiao, Li Wang, Cai Zhang, Hang Wen, Dacheng Xiao and Wei Zhi in Dr. Li's group. Within the PIHM modeling group, Yuning Shi, Yu Zhang, Lele Shu, Lorne, Felipe, Gustavo have all been very helpful in the development, debugging and testing of RT-Flux-PIHM. I also thank Dr. Pamela Sullivan, Dr. Lixin Jin, Xin Gu for their input on geochemical model in Shale Hills Critical Zone Observatory.

Finally, I would like to thank my wife Yan Huang. Her support, encouragement, enthusiasm for life, cheerful personality, patience and unwavering love were undeniably the bedrock of my life. When I am occasionally in bad moods, she is tolerant. When I am feeling frustrated, she is always encouraging. I also thank my father, Weijun Bao, who has always been supportive and encouraging to me.

This research was supported by NSF Critical Zone Observatory program grants to CJD (EAR 07-25019) and SLB (EAR 12-39285, EAR 13-31726). This support is greatly appreciated.

Chapter 1

Introduction

Many scientific endeavors and engineering applications involve tracking and predicting the transport, reaction and fate of chemical species within the flowing phase in natural systems or in laboratories. Such problems include diagenetic and weathering of the rocks that forms our earth (Johnson et al., 2004; White and Brantley, 2003), subsurface hazardous material disposal (Van der Lee et al., 1992; Zachara et al., 2002), environmental remediation (Arbogast et al., 1996; Fang et al., 2009; Jamieson-Hanes et al., 2012; Li et al., 2011; Li et al., 2010; Li et al., 2009; Runkel and Kimball, 2002; Scheibe et al., 2009; Wu et al., 2006; Yabusaki et al., 2011), enhanced oil recovery (Banat, 1995; Qiao et al., 2014a, b), CO_2 sequestration (Audigane et al., 2007; Bachu, 2000; Brunet et al., 2013; Johnson et al., 2004; Xu et al., 2003), groundwater quality deterioration due to CO_2 sequestration (Frye et al., 2012), chemical flooding (Shah, 1977), etc..

In many of such efforts, flow dynamic, mass transfer process and geochemical reactions are intricately coupled. Materials are transported by advection and dispersion due to the bulk motion of fluid within porous media, which creates spatiotemporal variations in the aqueous chemistry and fluid composition in pore space. Depending on the local aqueous chemistry, geochemical reactions alter porosity and permeability of the porous media (Brunet et al., 2013). Sometimes chemical species will also alter the wettability of the mineral surface, causing changes in relative permeability (Qiao et al., 2014b). Such alterations in turn controls the bulk motion of fluid in the field (Brunet et al., 2013). These feedbacks between processes can exist in different spatial scales, ranging from pore scale, core scale, and up to the field scale. Therefore, we are often presented with coupled systems where transport phenomena and chemical reactions are intertwined.

One of such problems is the hydro-geochemical evolution in watersheds. The Critical Zone (CZ), defined as the near-surface layer of the earth between tree canopy and the top of bedrock, is vital in sustaining life (Brantley et al., 2006). In the CZ, multiple physical and biogeochemical processes corporate to shape the Earth's surface and control its functioning (Stallard, 1998). Surface hydrologic processes (e.g., precipitation, infiltration, evapotranspiration, surface runoff and channel flow) determine water fluxes and serves as a fundamental control on other physical, geochemical and biological processes. Biogeochemical processes, on the other hand, alters the properties of rocks and soils, ultimately influencing hydrological processes (Brantley et al., 2013a). The interplay between hydrological and geochemical processes is perplexing and poorly understood at the watershed scale. For example, the hydrology and geochemistry communities have long been puzzled by the double paradox (Kirchner, 2003). One is the "rapid mobilization of old water", reflecting the fact that streamflow responds rapidly to the size of the rainfall events, while the concentrations of passive tracers (e.g., chloride) and various cations remain relatively constant (chemostatic behavior) (e.g., (Clow and Mast, 2010; Godsey et al., 2009)). The other is the "variable chemistry of old water", reflecting that watersheds release "old" waters of different chemical composition in rainfall events of different size.

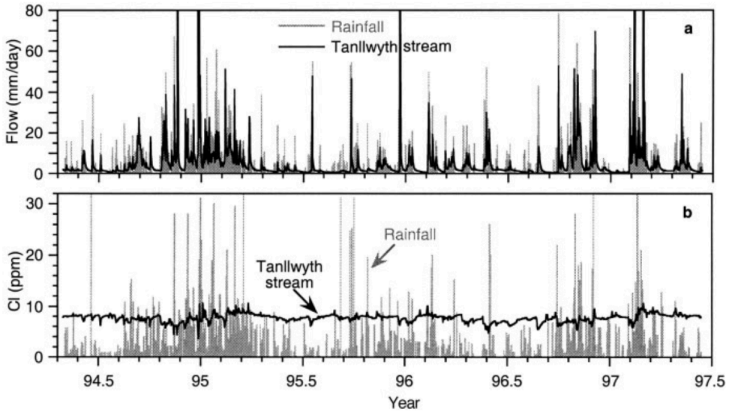

Figure 1-1 "Rapid mobilization of old water": a) rainfall and stream discharge b) chloride concentration in stream and in rainwater for Tanllwyth stream at Plynlimon, Wales. Stream discharge is responsive to rainfall events, however chloride concentration is

largely unaffected by rainfall event and rainwater chloride concentration, although chloride is controlled by rainfall input. Figure from (Kirchner, 2003)

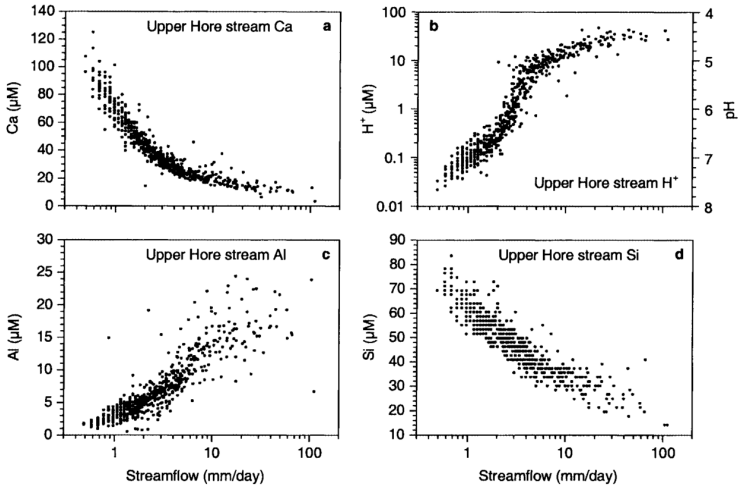

Figure 1-2 “Variable chemistry of old water”: Semilog plots of concentrations of reactive species as functions of stream discharge at Upper Hore stream at Plynlimon, Wales. Concentrations of reactive species are dependent on stream discharge, but such relationship varies among different species. Figure from (Kirchner, 2003)

Resolving these puzzles requires an integrated and process-based understanding of the intricate interactions between hydrological and geochemical processes at the watershed scale (Beven, 1989; Beven, 2002; Kirchner, 2006). Such tools, however, do not yet exist. Three sets of equations to model flow dynamic, mass transfer process and geochemical reactions need be solved together in such a model.

The hydrology community has utilized distributed models for more than five decades (Gan et al., 2006; McDonnell et al., 2007; VanderKwaak and Loague, 2001) to understand coupled hydrological processes including rainfall infiltration, run off, surface and subsurface water interactions, snow melting, and river hydrodynamics (Abbott et al., 1986; Beven, 1989; Kumar et al., 2009b; Qu and Duffy, 2007; Quinn et al., 1991; Singh, 1995). With the incorporation of surface energy conservation, recent introduction of land surface processes into hydrological models marks a new advance toward more accurate representation of evapotranspiration (Maxwell and Miller, 2005; Shi et al., 2013b).

With the development of distributed hydrological models, pollutant transport models are also devised in order to predict and control detrimental effects of pollutants. Li and Duffy presented a simulator that models pollutant transport in a two dimensional finite volume setting for a range of physical and numerical conditions (Li and Duffy, 2012) based on works of (Jawahar and Kamath, 2000; Toro, 1992; Zoppou and Roberts, 1999). Solute and water quality models have been developed as add-ons to hydrological models to understand environmental impacts of contaminants (Arnold and Soil, 1994; Donigian Jr et al., 1995; Santhi et al., 2001). These models, however, use empirical and simplified correlations to represent reactions without incorporating physics-based multi-component reaction network and rigorous reaction thermodynamics and kinetics representations based on geochemical theory (Steefel et al., 2005).

The geochemistry community developed the mathematical and numerical frameworks for multi-component reactive transport modeling (RTM) over three decades ago (Lichtner, 1985; Parkhurst et al., 2003; Steefel and Lasaga, 1994; Yeh and Tripathi, 1989; Zysset et al., 1994). These physically based models solve the advection-dispersion-reaction equations (ADR) for explicit spatial distribution and temporal evolution of multiple chemical components. RTMs have since advanced to become powerful tools to understand complex flow, transport, and biogeochemical processes relevant to environment, water, and energy, including global geochemical cycling (Goddéris et al., 2010; Jacques et al., 2006; Mayer et al., 2002; Moore et al., 2012; Person et al., 1996; Steefel et al., 2005), environmental remediation (Bao et al., 2014; Tang et al., 2013), and energy production (Audigane et al., 2007; Qiao et al., 2014a). RTMs have mostly been applied to understand subsurface processes ranging from as small as the pore scale (microns) to as large as field scales (100 meters) (Atchley et al., 2014; Beisman et al., 2015; Navarre-Sitchler et al., 2013).

The rapid developments of the three fields have led to the possibility to elucidate the

interplay of hydrological and geochemical process at the watershed scale. However, several key assumptions must be made before coupling models. First of all, the water dynamics in the natural shallow subsurface is essentially different than deep groundwater. In the shallow subsurface, the exchange between soil water, ground water, stream and rain water is swift and frequent (Morrice et al., 1997; Yang et al., 2000). When such exchange happens, mixing of chemicals may not follow a uniform pattern. Some chemical species are supposedly non-reactive and are transported conservatively (Peters et al., 1998). On the other hand, some reactive species are subject to cation exchange reactions, which will control the aqueous concentration of the reactive species and also leads to retardation of transport (Duffy and Cusumano, 1998; Jin et al., 2011a). For a model that is operating on field scale, although we still consider the effects of cation exchange reactions for reactive species for the cell centered volume averaged system of each finite element, lower scale effects are not explicitly treated. That is, our model is only as good as our mesh is. Secondly, the subsurface region that we most care of is variably saturated. The fully saturated zone and partially wetted zone should therefore be treated separately in both transport and geochemical reactions. However, although the influence of saturation have long been discussed and treated in transport processes (Goldberg and Higuchi, 1969; Goldberg et al., 1967), it is still clear that how saturation conditions affect geochemical reactions and key assumptions on how kinetic rates depends on saturation must be made (Xu et al., 2000). Thirdly, it is important to define "solute" as only the chemical species that is non-colloid, which means, the concentration of solute should only be measured after the sample passes filters of certain threshold, e.g. 45 μm. Therefore, some of the data retrieved from literature or field measurement should be used with caution since it is possible certain "concentration" measurements contain both solute and colloid. In addition, forests uptakes (Douglas et al., 1992), roots respiration (Dobrowolski et al., 1990), even worms' and animals' activities (Jordan et al., 1997) contributes to the dynamics of shallow water and its chemistry. Such "higher order" interactions are generally inadequately formulated.

In this work, we developed the code RT-Flux-PIHM that integrates a multi-component reactive transport module (RT) with Flux-PIHM (Shi et al., 2013b), the distributed hydrological model Penn State Integrated Hydrological Model (PIHM) with a land surface module adapted from the Noah Land Surface Model (LSM). The reactive transport module enables the simulation of geochemical reactions including mineral dissolution and precipitation, redox reaction, surface complexation, cation exchange and aqueous complexation. Combined with the capability of Flux-PIHM in simulating hydrological and land surface processes, the RTM module in RT-Flux-PIHM expands our capabilities to simulate the closely coupled hydrogeochemical processes. This model was evaluated for the Susquehanna Shale Hills watershed (0.08 km^2), a National Science Foundation (NSF) Critical Zone Observatory (SSHCZO). SSHCZO has been established to advance critical zone understanding with extensive field measurements and simulation works (Brantley et al., 2006; Duffy et al., 2009). In particular, data collected in SSHCZO has facilitated the conceptual framework that takes into account major hydrogeochemical processes at the site (Jin et al., 2011a). The capabilities developed through RT-Flux-PIHM will provide insights on the spatially-explicit hydrogeochemical dynamics in the watershed.

By matching the field observation and studying the spatial-explicit hydrogeochemical dynamics in this watershed, we identify the key hydrological and geochemical controls on selected solute concentrations in the field and in the stream. Prior to this work, many researches have developed models to explain the controlling mechanisms of solute concentration in stream water. E.g. for non-reactive species chloride, Stallard and Murphy explained the slightly dilution behavior of chloride concentration discharge relationship (Stallard and Murphy, 2014) based on End-Member mixing analysis (EMMA) (Hooper et al., 1990) and concluded that the CQ of chloride is controlled primarily by the repeated mixing of rainwater and soil water reservoir. Kirchner found that the chemostatic CQ relationship could arise from a special type of water residence time distribution that is corresponding to the field scale advection dispersion process if

the dispersivity is at the scale of the hillslope length (Kirchner et al., 2000, 2001). For reactive, weathering-derived elements, Stallard and Murphy suggested that the stream concentration is weighted average of the concentration of soil water, which is a product of weathering and the rainfall deposition (Stallard and Murphy, 2014). Maher et al. further noted that the stream solute concentration for weathering elements capped by the thermodynamic limit of the weathering reaction and is regulated by hydrological activities. Damkohler number could be used in the latter case to quantify the competition between removal of product by flux and generation of elements by reaction and to predict stream solute concentration (Maher and Chamberlain, 2014). Jin Lixin et al. speculated that cations in stream water and soil water are likely controlled by the cation exchange reaction that is prevalent in soils (Jin et al., 2011a). Godsey and her colleagues used a permeability-porosity-aperture model to explain the chemostasis of cations by assuming an exponential decrease of porosity, permeability and fracture aperture along depth (Godsey et al., 2009).

In recent years, there has been an ongoing discussion on how watershed hydrological connectivity impacts the generation of runoff and controls the solute transport as the small watershed responds to rainfall and snowmelt events (Jencso et al., 2009; McGuire and McDonnell, 2010; Western et al., 2004). Based on field observations, Herndon et al. (2015) argued that concentration of solutes that is not bio-active is homogeneous across the watershed and the concentrations of bioactive solutes is heterogeneous and correlate to the distribution of organic matters. The stream drains different water pools in different seasons due to changes in hydrological connectivity, which controls the solute concentration discharge relationship (Herndon et al., 2015).

Based on these existing models and conceptual models, we intend to use RT-Flux-PIHM as process-based modeling effort that integrates different processes while at the same time can separate and interrogate the importance of each mechanism.

Chapter 2 contains a discussion on the coupled problem, the numerical methods to solve the governing equations for the coupled system. Chapter 3 is an application of this model at Shale Hills watershed. Chapter 4 discusses the watershed characteristics that control the solute concentration discharge relationship, using chloride as an example of non-reactive species. Some of the chapters are parts of submitted manuscripts and have been heavily edited by co-authors. Chapter 5 gives the summary of current work. Chapter 6 is a discussion on future works. Details on the algorithm, the code and the usage of this code are provided in appendix.

Chapter 2

Development of RT-Flux-PIHM

Abstract

We developed RT-Flux-PIHM, a code that augments existing simulation capabilities of hydrological processes (PIHM) and land-surface interactions (FLUX) by adding a multi-component reactive transport module (RT) that simulate geochemical processes including aqueous complexation, surface complexation, mineral dissolution and precipitation, and cation exchange. The code was verified against the widely-used reactive transport code CrunchFlow. We demonstrate the use of RT-Flux-PIHM by applying it to understand the hysteresis of concentration and discharge relationship of the non-reactive tracer chloride and the reactive magnesium during a large rainfall event in the Susquehanna Shale Hills Critical Zone Observatory (SSHCZO). The results show the significant role of a large rainfall event in flushing out and exporting the chemicals out of the watershed. Ion exchange offers buffering capacities and maintains relatively constant Mg concentration in the stream outlet. RT-Flux-PIHM offers unprecedented capabilities of carrying out virtual experiments at the watershed scale to understand key controls of hydrogeochemical processes in a spatially-explicit manner.

1. Introduction

Hydrological and geochemical process dynamics at the watershed scale is complex. Surface hydrologic processes partition rainwater into atmosphere, plants, surface water (river), and subsurface water reservoirs (soil and ground water) (Brooks et al., 2015). The water movement in soils and shallow groundwater drives abiotic reactions including mineral dissolution and precipitation and surface and aqueous complexation and biotic reactions such as soil carbon

decomposition, ultimately exporting reaction products out of the watersheds (Jin et al., 2010). The interactions between hydrological and geochemical processes modify water chemistry, which are important indicators of water quality (Kirchner and Neal, 2013), chemical weathering rates (Gaillardet et al., 1999; Navarre-Sitchler and Brantley, 2007; White, 1995), biogeochemical activities (Boyer et al., 1997), and elemental cycling (Kump et al., 2000).

Hydrogeochemical dynamics at the watershed scale, however, has been a long-standing puzzle. For example, efforts of explaining concentration and discharge relationship date back to about half a century ago where a working model was proposed to explain 4 decades of stream chemistry data (Cl) from the Hubbard Brook forest in New Hampshire (Johnson et al., 1969). More than 3 decades later, the "rapid mobilization of old water", the fact that streamflow responds rapidly to the size of the rainfall while the concentrations of some chemicals are barely responsive, is still not well understood (Godsey et al., 2009; Kirchner, 2003). Understanding complex interactions between water, energy, and fluxes at the watershed scale requires an integrated framework and a systematic view of process coupling. Such integration tools require efforts across hydrology, hydrogeology, and biogeochemistry (Duffy et al., 2014).

In subsurface biogeochemistry, multi-component Reactive Transport Models (RTMs) originated in the 1980s (Chapman, 1982; Chapman et al., 1982). RTMs couple flow and transport calculation within a full geochemical thermodynamic and kinetic framework (Steefel et al., 2015), therefore enabling explicit tracing of spatial and temporal evolution of biogeochemical species in fluid and solid phases. Built upon the theoretical framework for reaction thermodynamics and kinetics (Lichtner, 1985, 1988), RTM development took gigantic stride in the 1990s showcasing the emergence of various RTM codes that become extensively used in the past decades (Bethke, 1996; Hammond et al., 2014; Lichtner et al., 1996; Mayer et al., 2002;

Ortoleva et al., 1987; Steefel and Lasaga, 1994; Van Cappellen and Wang, 1996; White and Oostrom, 2000; Xu et al., 1999; Yeh and Tripathi, 1989).

RTMs have been used across a diverse array of environments involving both porous and fractured media (as reviewed in MacQuarrie and Mayer, 2005; Steefel et al., 2005). They have simulated a wide range of processes, including flow, solute transport, mineral dissolution and precipitation, ion exchange, surface complexation, as well as biotic processes such as microbe-mediated redox reactions, biomass growth and decay. Such models have been applied to understand processes on various topics, including chemical weathering (Bolton et al., 1996; Brantley and Lebedeva, 2011; Maher et al., 2009; Moore et al., 2012), biogeochemical cycling in coastal marine sediments (Dale et al., 2008; Krumins et al., 2013; Regnier et al., 1997), environmentally biostimulation (Druhan et al., 2012; Li et al., 2010; Yabusaki et al., 2011), natural attenuation (Liu et al., 2008; Mayer et al., 2001), geological carbon sequestration (Atchley et al., 2013; Brunet et al., 2013; Navarre-Sitchler et al., 2013; Tutolo et al., 2015; Xu et al., 2003), nuclear waste storage (Saunders and Toran, 1995; Soler and Mader, 2005), and energy production (Audigane et al., 2007; Qiao et al., 2015). RTM studies have so far mostly focused on process at spatial scales from pores (Fang et al., 2011; Kang et al., 2006; Li et al., 2008; Molins et al., 2014; Scheibe et al., 2015) to field scales at tens of meters (Li et al., 2011), and more recently at the watershed or catchment scale of hundreds of meters (Beaulieu et al., 2011; Beisman et al., 2015; Navarre-Sitchler et al., 2013). Regional scale RTMs have recently been linked to global vegetation models to understand the role of climate change in controlling weathering over periods of 10^0 to 10^3 years (Goddéris et al., 2013; Godderis et al., 2006; Roelandt et al., 2010).

The hydrology community, on the other hand, has utilized distributed models for more than five decades to understand hydrological processes including rainfall infiltration, runoff, surface water and subsurface water interactions, snow melting, and river hydrodynamics (Abbott

et al., 1979; Abbott et al., 1986; Beven, 1989; Freeze and Harlan, 1969; Gan et al., 2006; James, 1972; Jarboe and Haan, 1974; Kumar et al., 2009; McDonnell et al., 2007; Qu and Duffy, 2007b; Quinn et al., 1991; Singh, 1995; Therrien et al., 2010; VanderKwaak and Loague, 2001). With the integration of surface energy balance, recent introduction of land surface processes into hydrological models marks a new advance toward more accurate representation of evapotranspiration (Maxwell and Miller, 2005; Shi et al., 2013). Solute and water quality models have been developed as add-ons to hydrological models to understand environmental impacts of contaminants (Arnold and Soil, 1994; Donigian Jr et al., 1995; Santhi et al., 2001). These models use empirical and simplified correlations and do not incorporate physics-based multi-component reaction network and rigorous reaction thermodynamics and kinetics representations (Davison et al., 2014).

Although multi-component reactive transport has recently started to be coupled with large-scale hydrological processes (Beisman et al., 2015; Yeh et al., 2006), a full integration among land surface interactions, surface and subsurface hydrological processes, and multi-component reactive transport is still lacking. Here we develop the code RT-Flux-PIHM that integrates a multi-component reactive transport module (RT) with Flux-PIHM (Shi et al., 2013), the distributed hydrologic model Penn State Integrated Hydrological Model (PIHM) (Qu and Duffy, 2007a) with a land surface module adapted from the Noah Land Surface Model (LSM) (Figure 1). The reactive transport module includes mineral dissolution and precipitation, surface complexation, cation exchange and aqueous complexation. The process integration can be used to identify important processes and to elucidate dominant controls of watershed process dynamics. Flux-PIHM and for RT model, followed by the numerical schemes employed in the RT model.

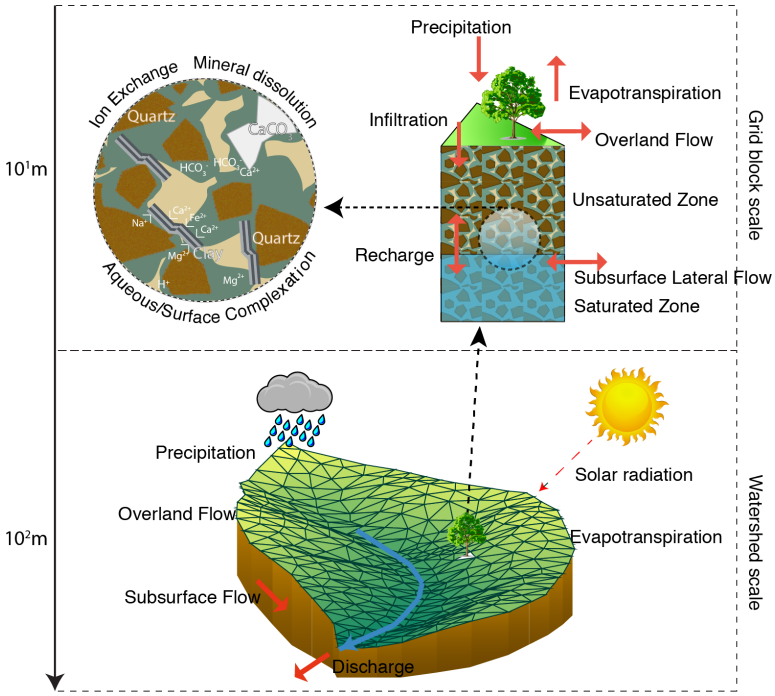

Figure 2-1 Processes included in RT-Flux-PIHM. Flux-PIHM simulates the hydrological and land surface dynamics (precipitation, canopy interception, infiltration, recharge, overland flow, subsurface lateral flow, river flow, and surface energy balance) at the watershed scale using the finite volume method. The RT module takes the water output from Flux-PIHM and simulates the multi-component reactive transport processes, allowing hydrological and geochemical coupling. The discretized mesh structure for the Susquehanna Shale Hills Critical Zone Observatory (SSHCZO) is depicted at the bottom. Geochemical processes, including mineral dissolution and precipitation, ion exchange, surface complexation, and aqueous complexation, are included in the RT module.

2. Development of RT-Flux-PIHM

2.1 Model Structure Overview

RT-Flux-PIHM discretizes the simulation domain into unstructured prismatic elements, which allows the accurate representation of the watershed topography and boundaries. Detailed

processes and equations of Flux-PIHM are in literature (Qu and Duffy, 2007a; Shi et al., 2013) . Here we briefly discuss the key aspects that are important to understand the rest of the paper.

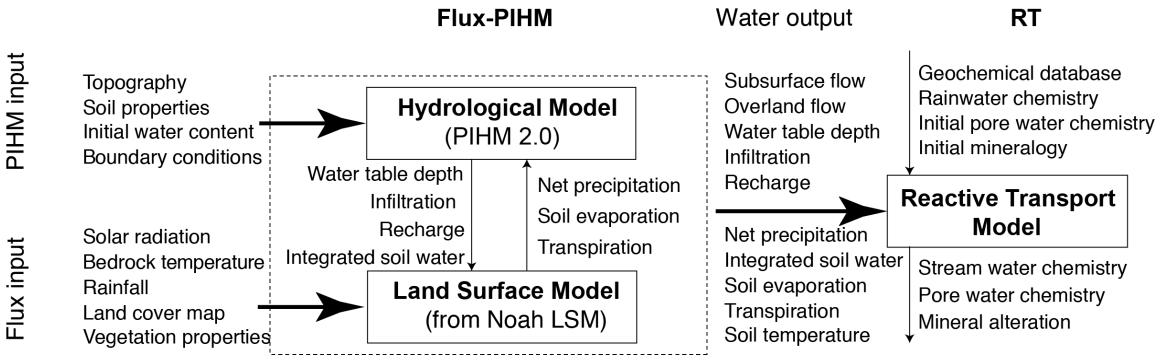

Figure 2-2 Input, output, and process coupling within RT-Flux-PIHM. The Flux-PIHM module solves the hydrological and land surface dynamics. The RT module reads flow and water distributions from Flux-PIHM and specified initial chemistry of water and solid phases, and outputs the spatial and temporal evolution of aqueous and solid phase compositions based on the hydrological conditions and geochemical thermodynamics and kinetics.

RT-Flux-PIHM contains three modules: The Noah LSM (the surface heat flux module), PIHM, and RT (Figure 2-2). The Noah LSM is the land-surface module that solves energy balance at the land surface (Chen and Dudhia, 2001; Shi et al., 2013). It simulates surface heat fluxes (sensible, latent, and ground heat fluxes), canopy water balance, internal soil heat and moisture fluxes, and snow processes. When coupled with PIHM, the net precipitation, soil evaporation, and transpiration calculated by Noah feed into PIHM for the calculation of surface and groundwater interactions (surface runoff, infiltration, recharge, subsurface lateral flow, channel routing) (Figure 2-2). The Noah LSM and PIHM are closely coupled in Flux-PIHM. The RT module uses the water distribution and flow rates from Flux-PIHM and solves the Advection Dispersion Reaction (ADR) equations for the spatial and temporal evolution of aqueous and solid phase composition. The alteration in aqueous and mineralogical composition is assumed to have negligible impacts on hydrological processes at the time scale of months to years. RT component

typically takes larger time steps than the Flux-PIHM component. Flux information is stored and averaged before each RT time stepping.

The current coupling strategy maintains mass balance in both surface and subsurface processes for water and chemical species. Momentum is conserved in subsurface processes where Darcy's law or Richard's equation governs the flow dynamics. In surface hydrological processes, approximation is used therefore momentum is not strictly conserved (Qu and Duffy, 2007). Energy balance is achieved in the soil up to 200 cm deep by considering the vertical heat conduction within each prismatic element (Shi et al., 2013).

To physically simulate these dynamic processes, multiple types of input data are required, as shown in Figure 2-3. Flux-PIHM takes in watershed characteristics, initial conditions and boundary conditions, and time-series forcing data. Watershed characteristics include topography (e.g., soil depth, surface elevation), soil properties (e.g., soil type, soil hydraulic conductivity, porosity, macropore conductivity, Van Genuchten parameters), and vegetation properties (e.g., land cover type, rooting depth, maximum stomatal resistance) (Shi et al., 2013). Watershed initial and boundary conditions include the initial water distribution, soil temperature, land surface temperature, water table depth, snow cover, canopy storage and watershed boundary fluxes. Time series forcing data include precipitation, air temperature, relative humidity, wind speed, downward solar radiation, downward longwave radiation, surface air pressure and leaf area index (LAI). RT takes in the geochemical characteristics of rainwater, soil water, soil, as well as the thermodynamics and kinetics of geochemical reactions. A set of control and calibration files are required to facilitate the history matching using the global calibration coefficient approach (Pokhrel and Gupta, 2010).

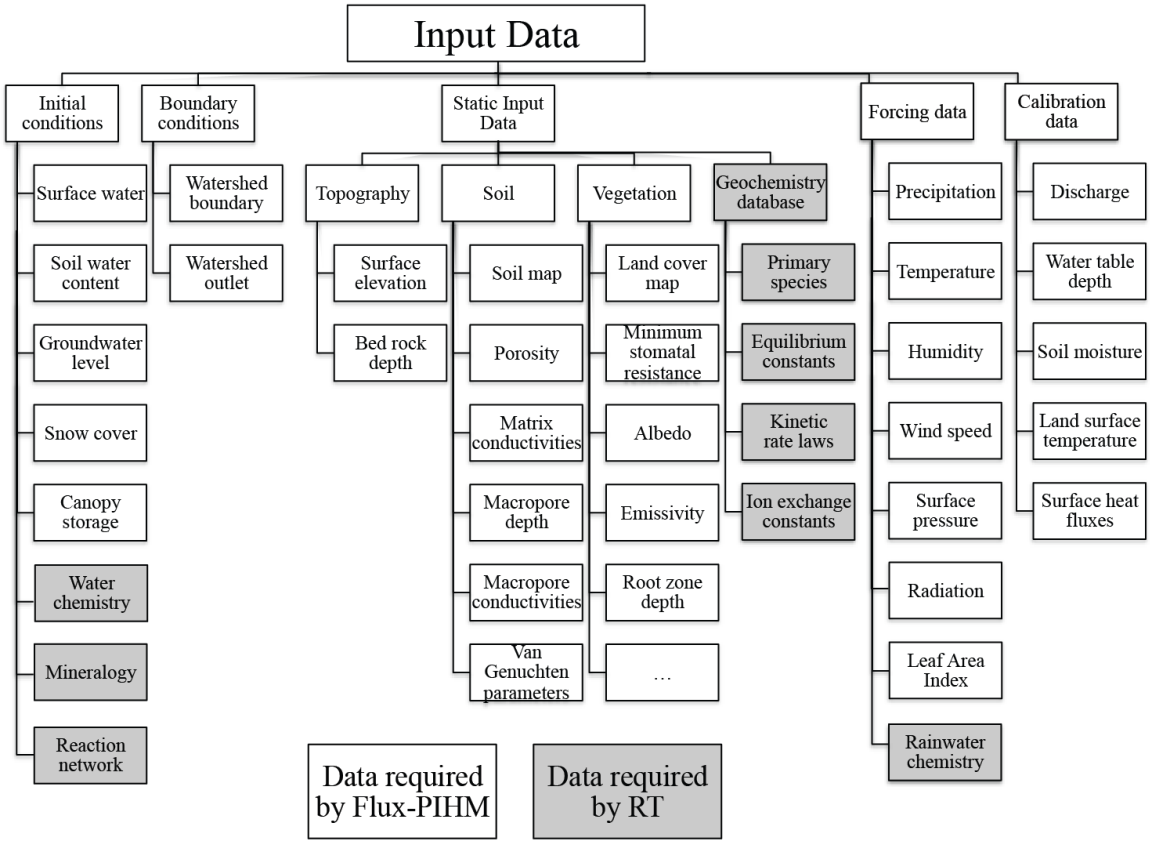

Figure 2-3. RT-Flux-PIHM is a data-intensive model intended to investigate the multi-physics interactions at watershed scale. Five types of input files are required: initial conditions, boundary conditions, static inputs, forcing data and calibration files. In additional to data required by Flux-PIHM, RT module need initial geochemical conditions, reaction network, geochemical database, and forcing chemistry to simulate the geochemical processes.

2.2 The Land-surface Module Noah Land Surface Model

The Noah LSM implemented in Flux-PIHM includes the Penman potential evaporation scheme (Mahrt and Ek, 1984), a multiple-layer soil model (Mahrt and Pan, 1984), the canopy model (Pan and Mahrt, 1987), the canopy resistance model by Noilhan and Planton (1989) and Jacquemin and Noilhan (1990). Here we present the formulations for soil temperature, evapotranspiration, and net precipitation in the Noah LSM, which interact with PIHM and RT. Details of the Noah LSM and the coupling between the Noah LSM and PIHM can be found in literature (Chen and Dudhia, 2001; Shi et al., 2013).

The Noah LSM solves the soil temperatures T_s at four vertically discretized soil layers (0~10 cm, 10~40 cm, 40~100 cm, 100~200 cm) in each prismatic finite volume:

$$C(\Theta)\frac{\partial T_s}{\partial t} = \frac{\partial}{\partial z}\left[K_t(\Theta)\frac{\partial T_s}{\partial x}\right] \tag{1}$$

where Θ is the soil water content [$m^3\ m^{-3}$], T is the soil temperature [Kelvin] and z is the depth of soil [m]; the volumetric heat capacity C [$J\ m^{-3}\ K^{-1}$] and the thermal conductivity K_t [$W\ m^{-1}\ K^{-1}$] are both functions of volumetric soil water content and also depend on the heat capacity of water, soil and air (Pan and Mahrt, 1987). The total evapotranspiration E is given by

$$E = E_{\mathbf{soil}} + E_c + E_t, \tag{2}$$

where E_{soil} is the evaporation from soil, E_c is the evaporation from canopy interception, and E_t is the canopy transpiration, all in unit of [$W\ m^{-2}$)]. The soil evaporation is formulated as

$$E_{\text{soil}} = (1-\sigma_f)\left(\frac{\Theta_1 - \Theta_w}{\Theta_{ref} - \Theta_w}\right)^{fx_s} E_p, \tag{3}$$

where E_p is the potential evapotranspiration [$W\ m^{-2}$] calculated using the modified Penman potential evaporation scheme (Mahrt and Ek 1984), σ_f is the vegetation fraction [$m^2\ m^{-2}$], Θ_{ref} is the soil field capacity [$m^3\ m^{-3}$], Θ_w is the soil wilting point [$m^3\ m^{-3}$], and the soil evaporation coefficient $fx_s = 1$. The canopy evaporation is calculated as

$$E_c = \sigma_f\left(\frac{h_v}{h_{v\max}}\right)^{fx_c} E_p, \tag{4}$$

where h_v is the storage of canopy interception [m^3 m^{-2}], $h_{v\max}$ is the maximum canopy water capacity [m^3 m^{-2}] which is a function of leaf area index (LAI), and the canopy evaporation coefficient $fx_c = 0.5$.

The canopy transpiration is determined by

$$E_t = \sigma_f B_c \left[1 - \left(\frac{h_v}{h_{v\max}} \right)^{fx_c} \right] E_p, \tag{5}$$

where B_c is a function of canopy resistance that is affected by solar radiation, vapor pressure deficit, air temperature, and root zone soil moisture.

The dripping rate from the vegetation is calculated by:

$$D = \begin{Bmatrix} k_D \exp(b \frac{h_v}{h_{v\max}}), h_v \in (0, h_{v\max}) \\ k_D \exp(b) + \frac{h_v - h_{v\max}}{\Delta t}), h_v \in (h_{v\max}, \infty) \end{Bmatrix} \tag{6}$$

where D is the dripping rate [$m^3/(m^2$ s)]; k_D is the reference dripping rate [$m^3/(m^2$ s)]; parameter b is a fitting parameter.

The net precipitation (precipitation not intercepted by the canopy) is:

$$p_{net} = (1 - \sigma_f) p + D \tag{7}$$

where p is the total precipitation on the model grid [$m^3/(m^2$s)].

2.3 The Hydrological Module PIHM

PIHM solves for three principal unknowns that describe the water distribution in each prismatic element: water storage at surface h_s [m^3/m^2] (water that builds upon land surface and

forms overland flow), water storage in the unsaturated zone h_u [m^3/m^2], and water storage in the saturated zone h_g [m^3/m^2], where each storage volume is normalized by the base area of the prismatic element. The surface water storage in element *i* depends on flow rates in and out of the element *i*:

$$\frac{dh_{s,i}}{dt} = p_{net} - q_{infiltration} - E_{soil} - \sum_{j=1,N_{i,1}}^{N_{i,3}} q_{s,ij} \tag{8}$$

where the rates of net precipitation (p_{net}), infiltration from land surface to unsaturated zone ($q_{infiltration}$), evaporation from soil (E_{soil}) if surface water is present, and lateral surface flow from element *i* to *j* ($q_{s,ij}$) are all normalized by the base area of the finite element [$m^3/(m^2\ s)$]. $N_{i,1\sim3}$ is the index of the neighboring elements of *i*. The flux rates p_{net} and *e* are computed in the land surface module (Noah LSM) while $q_{s,ij}$ is calculated based on a diffusion wave approximation of the 2D St. Venant equation (Gottardi and Venutelli, 1993). The surface water determines the amount of overland flow.

Water storage in the unsaturated and saturated zones of element *i* are calculated as follows:

$$\theta \frac{dh_{u,i}}{dt} = q_{infiltration} - q_{recharge} - E_{soil} - E_t \tag{9}$$

and

$$\theta \frac{dh_{g,i}}{dt} = q_{recharge} - q_{bedrock} - \sum_{j=N_{i,1}}^{N_{i,3}} q_{g,ij} \tag{10}$$

where θ is the porosity [m^3 pore space /m^3 porous medium]; $q_{recharge}$ is the area-normalized recharge rate into the saturated zone, E_{soil} is soil evaporation if surface water is absent and E_t is the transpiration of canopy from unsaturated zone, $q_{bedrock}$ is the downward flow rate into bedrock [$m^3/(m^2$ s)], although $q_{bedrock}$ is considered zero in the model; $q_{g,ij}$ is the area normalized lateral flow rate [$m^3/(m^2$ s)] from element i to j in the saturated zone, which is calculated using Darcy's law. The soil evaporation term E_{soil} is subtracted from surface water if surface water is present (Eq.8). Otherwise, it will be taken from the soil unsaturated zone. In the unsaturated zone, lateral flow rates are assumed to be zero and only vertical flow occurs, a common assumption for flow in the unsaturated zone (Zhu et al., 2012). The division between the unsaturated and saturated zone essentially represents the hydrological dynamics in the soil layer where water is sometimes sufficient to saturate surficial layers, allowing horizontal flow (interflow) to the stream. Within each element, the saturated and unsaturated zones are divided by the (perched) water table in the soil layer. Because the position of the water table is variable in time and space, so are the thicknesses of the saturated and unsaturated zones. Flux-PIHM assumes a zero flux boundary condition at the top of the bedrock. Recharge and infiltration are calculated based on steady-state Richard's equation (Duffy, 2004). An integration over the unsaturated zone using the Van Genuchten type soil moisture characteristic is performed to simplify the calculation of recharge and infiltration (Qu and Duffy, 2007a; Van Genuchten, 1980). Macropore flow (vertical and horizontal) is simulated from the land surface to a predefined macro pore depth (Beven and Germann, 1982; Shi et al., 2013).

2.4 Reactive Transport Processes in RT

Reactive transport equations. The RT module solves the mass conservation equations for chemical species in the water phase in the subsurface. It considers advective and dispersive transport and geochemical reactions using the finite volume method (Xu et al., 2006). Chemical

reactions include equilibrium-controlled and kinetically controlled reactions. In this work, equilibrium-controlled reactions include aqueous complexation, cation exchange and surface complexation while mineral dissolution and precipitation are considered as kinetically controlled. This leads to a natural partitioning into primary (basis) species that are the building blocks of the chemical system and secondary species whose concentrations are calculated from primary species concentrations using laws of mass action for equilibrium-controlled reactions (Lichtner, 1985).

Following the classic reactive transport formulation, advection dispersion reaction (ADR) equations are written only for the primary species (basis set) (Lichtner, 1996; Steefel and Lasaga, 1994; Yeh and Tripathi, 1989). An example equation is shown here for one of the *np* primary chemical species *m* in a subsurface element *i*:

$$\frac{\partial}{\partial t}(S_w \theta V C_m) - \sum_{j=N_{i,1}}^{N_{i,x}} (-A_{ij} D_{ij} \nabla C_m + A_i q_{ij} C_m) - V R_m - SS_m = 0, \qquad m = 1,...,np \tag{11}$$

where S_w is water saturation [m^3 water /m^3 pore space]; V is the total volume of the element i; C_m is the aqueous concentration of m [mol /m^3 water]; A_{ij} is the grid interface area shared by element i and j; D_{ij} is the norm [m^2/s] of combined dispersion / diffusion tensor normal to the shared surface; A_i is the base area of element i; q_{ij} are the normalized flow rates across the shared surfaces [m/s], which are also the right hand side terms in equation 10, 11 and 12, including lateral flow rates, recharge rate and infiltration rate; $\underline{N_{i,x}}$ is the indices of the elements sharing surfaces with element i. Values of x is 2 for unsaturated zone (infiltration, recharge) and is 4 for saturated zone (recharge plus three lateral flow directions)). Here R_m is the total rate of kinetically-controlled reactions with species m and can be a summation of rates from multiple reactions that involve m [mol /(m^3 s)]; SS_m is the additional total sinks or sources [mol /s]. This can include chemical species entering or leaving a finite volume through rainfall, dust deposition,

snowfall, and groundwater influx into the stream. In equation (11), $S_w = 1$ for saturated zone and $S_w < 1$ for unsaturated zone.

Each prismatic grid block have unsaturated and saturated layer in the soil zone that is divided by the transient water table. The porous medium volume of each layer could be written as a function of water storage in the Flux-PIHM convention:

$$V = \begin{cases} h_u A_i / S_w, & \text{unsaturated zone} \\ h_g A_i, & \text{saturated zone} \end{cases} \tag{12}$$

Assuming constant porosity we can further write the above equation (11) into equations for the unsaturated zones:

$$\frac{\theta \Delta (h_u C_m)}{\Delta t} = \sum_{j=N_{i,1}}^{N_{i,3}} (-\frac{A_{ij}}{A_i} D_{ij} \nabla C_m + q_{ij} C_m) + \frac{h_u R_m}{S_w} + \frac{SS_m}{A_i} \tag{13}$$

And for the saturation zone:

$$\frac{\theta \Delta (h_g C_m)}{\Delta t} = \sum_{j=N_{i,1}}^{N_{i,4}} (-\frac{A_{ij}}{A_i} D_{ij} \nabla C_m + q_{ij} C_m) + h_g R_m + \frac{SS_m}{A_i} \tag{14}$$

These two equations therefore handle the moving boundary between unsaturated zone and saturated zone within each prismatic soil column. Adding these two equations also yields the mass conservation of the entire prismatic element.

Reaction rate laws. For kinetically-controlled mineral dissolution and precipitation reactions, the rates are calculated based on the Transition State Theory (TST) (Helgeson et al., 1984; Lasaga, 1984):

$$R_k = A_k k_k (1 - \frac{IAP}{K_{eq}}) \quad (15)$$

Here R_k is the rate of mineral k (mol/(m^3 s)), A_k is the surface area of mineral k per volume of porous media [m^2/m^3] that is reacting at any given time; k_k is the intrinsic rate constant [mol /(m^2 s)]; IAP is the ion activity product for the reaction and K_{eq} is the equilibrium constant. The mineral surface area in the unsaturated zone is strongly affected by soil moisture (Clow and Mast, 2010). Here we assume this area depends on S_w raised to a power of n:

$$A_k = A_k^0 S_w^n \quad (16)$$

Here A_m^0 is the mineral surface area per volume of porous media under saturated conditions. Under unsaturated conditions the water tends to wet the surface everywhere but the water films do not flow and the surface area therefore assumes those films are at chemical equilibrium and are not experiencing net reaction. Note that for the same reaction rate R_k, the increase of reaction product concentration over time in the unsaturated zone will be $1/S_w$ times higher than in the saturated zone. If we assume R_k decrease proportionally to S_w^n, then the increase in product concentration in unsaturated zone will be the same as, smaller than or larger than in the saturated zone when $n = 1$, $n<1$ and $n>1$, respectively. So depending on the value of this exponent, product concentration in the unsaturated may accumulate at different paces compared to the saturated zone. In this work we use an n value of 2/3 to take into account the conversion between volume and area (Mayer et al., 2002). Secondary minerals that have the

potential to precipitate out are assigned an initial volume of 10^{-8} mol/m^3 porous media to allow the occurrence of precipitation when condition permits. Dissolving minerals are forced to stop dissolution when its volume fraction reaches this value.

Concentrations of dissolved inorganic carbon are calculated using Henry's law and the partial pressure of CO_2 in soil gas (Hasenmueller et al., 2013; Jin et al., 2014). Activities are calculated using the Debye–Hückel equation (Debye and Hückel, 1923). Surface complexation and cation exchange reactions are modeled following the non-electrostatic approach and Vanselow conventions, respectively (Dzombak, 1990; Vanselow, 1932).

2.5 Numerical Implementation

The RT module follows a sequential non-iterative approach (SNIA) that has been widely used (Walsh et al., 1984; Yeh and Tripathi, 1989) and is efficient in integrating subsurface flow simulation with reactive transport algorithms (Jacques et al., 2006). The SNIA is a derivative of the operator-splitting method that decouples ADR equation and solves transport and reaction steps separately (Xu et al., 1999; Zysset et al., 1994). The transport step is solved using the forward Euler method while the reaction step is solved iteratively using the Crank–Nicolson and Newton Raphson method. In the reaction step, the local matrices accounting for the mass balance of all primary species in each finite volume are assembled and solved using a matrix solver in SUNDIALS (Hindmarsh et al., 2005).

The accuracy of the SNIA approach depends on multiple factors including spatial discretization, time stepping, and flow conditions. Performance index (PI) is used to optimize the time stepping and to minimize numerical errors and improve convergence. PI is set to be less than 0.05 for every shared surface between elements to minimize the operator splitting error associated with temporal discretization (Jacques et al., 2006; Perrochet and Bérod, 1993):

$$\left(\frac{q_{ij}A_i}{A_{ij}}\right)^2 \frac{\Delta t}{D_{ij}} < 0.05 \quad (17)$$

Here Δt is the time duration in each step. The maximum time step is set to be five minutes (Jacques et al., 2006). The use of small PI and maximum time step requires a longer computational time however improves the SNIA accuracy.

In the reaction step, the RT module uses concentrations from the previous time step as the initial guess to iteratively solve for the concentration of the current time step. The spatial heterogeneity in hydrological processes can cause significant non-convergence problems. For example, the flow rates between two neighboring elements can vary from 0.01 to 4000 m^3/d. When flow rates are fast, time steps are reduced to facilitate convergence. Reducing the time steps based on the fastest flow, however, would essentially prevent the model from marching forward. Therefore, sub time step interpolation is used in the fast-flow regime to obtain a closer initial guess when non-convergence is encountered. During such interpolation, time step in the kinetic reaction solver for a particular gird block is continuously decreased until a convergence is reached. Then the solver proceeds to solve for chemical concentrations using the reduced time step until it catches up to the time step of the flow field. Numerical dispersion is also a serious concern for large-scale transport simulations with large grid blocks and fast flow dominated by convection (Li and Duffy, 2012). A total variation diminishing technique (TVD), which is third-order accurate in smooth regions, is used to reduce the extent of numerical dispersion (Gupta et al., 1991).

The typical mesh size in RT-Flux-PIHM is between10 and 100 m. RT-Flux-PIHM is designed to be conceptually simple and computationally economic. The standalone Flux-PIHM component solve for the land surface hydrological processes in the Shale Hills Critical Zone

Observatory (SSHCZO) for one year within three hours with one-minute time step on an Intel ® Xeon ® CPU E5-2670 @ 2.60GHz. Depending on the complexity of the reaction network, the intensity of the external forcing and source, the time required for RT-Flux-PIHM simulation for one year vary between four hours to several days. The time step for Flux-PIHM component is by default set to one minute. The maximum time step for RT component is by default set to five minute. The RT component adaptively adjusts its time step during simulation so the maximum time step user specifies is only suggestive.

3. Model Verification

To verify the implementation of RT, we compared its solutions to the extensively used reactive transport code CrunchFlow under a variety of flow and reaction conditions (Steefel and Lasaga, 1994). Results from RT and CrunchFlow for a one dimensional column experiments packed with calcite grains undergoing acidic solution injection are compared. The setup of the column, initial and inlet condition are summarized in Table 2-1. The kinetic reaction is calcite dissolution. Magnesium participates in ion exchange. Sodium and chloride are considered as conservative tracers. Bicarbonate acid serves as a buffer in the injected solution. Secondary species simulated are OH^-, CO_3^{2-}, $CO_2(aq)$. In total, six primary species, three secondary species (and three aqueous complexation reaction), one kinetic reaction and one adsorption reaction were simulated.

In the first case, we show an advection-only case by setting very small diffusion coefficient (1.0×10^{-20} cm^2/s) and dispersivity (1.0×10^{-20} m). Such an advection-only case will test the ability of the code to capture the sharp concentration front. In CrunchFlow, the OS3D mode is best suited to model advection-only problems. In RT module, the total variation diminishing (TVD) option is used to capture sharp fronts. In the second case, we include diffusion and

dispersion processes to test the code's ability to model solute transport. All other conditions are same as the first case except that diffusion coefficient is 1.0×10^{-5} cm^2/s and dispersivity is 0.1 m (Gelhar et al., 1992).

Table 2-1 Reactions and thermodynamic and kinetic parameters (Wolery, 1992)

Aqueous speciation	$\log_{10}K_{eq}$		
$H^+ + HCO_3^- == CO_2(aq) + H_2O$	6.34		
$HCO_3^- == H^+ + CO_3^{2-}$	-10.33		
$H_2O == H^+ + OH^-$	-13.99		
Ion exchange	$\log_{10}K_{eq}$		Site density (mol/m^2)
$>SOMg^+ + H^+ == >SOH + Mg^{2+}$	3.40		1×10^{-4}
Kinetic reactions	$\log_{10}K_{eq}$	$\log_{10}k$ ($mol/m^2/s$)	Specific surface area (SSA, m^2/g)
Calcite + $H^+ == Ca^{2+} + HCO_3^-$	1.85	-9.19	0.01

Table 2-2 Simulation Conditions

Darcian flux	m/day	2.00	Primary species	6
porosity		0.40	Mineral	1
Cementation exponent		1	Secondary species	3
Total column length	m	10.00	Ion exchange	1
Grid size	m	0.10	Kinetic Reactions	1
Number of cells		100		

Table 2-3 Chemical conditions

Conditions	inlet	initial
Aqueous	Unit: (M)	Unit: (M)
Na^+	1.00×10^{-7}	1.00×10^{-3}
Ca^{2+}	5.00×10^{-3}	1.00×10^{-7}
HCO_3^-	1.00×10^{-2}	1.00×10^{-7}
pH	4.00	7.00
Cl^-	3.00×10^{-3}	1.50×10^{-3}
Mg^{2+}	2.00×10^{-3}	1.00×10^{-7}
Mineral	Volume fraction	Volume fraction
Calcite	0.00	0.10

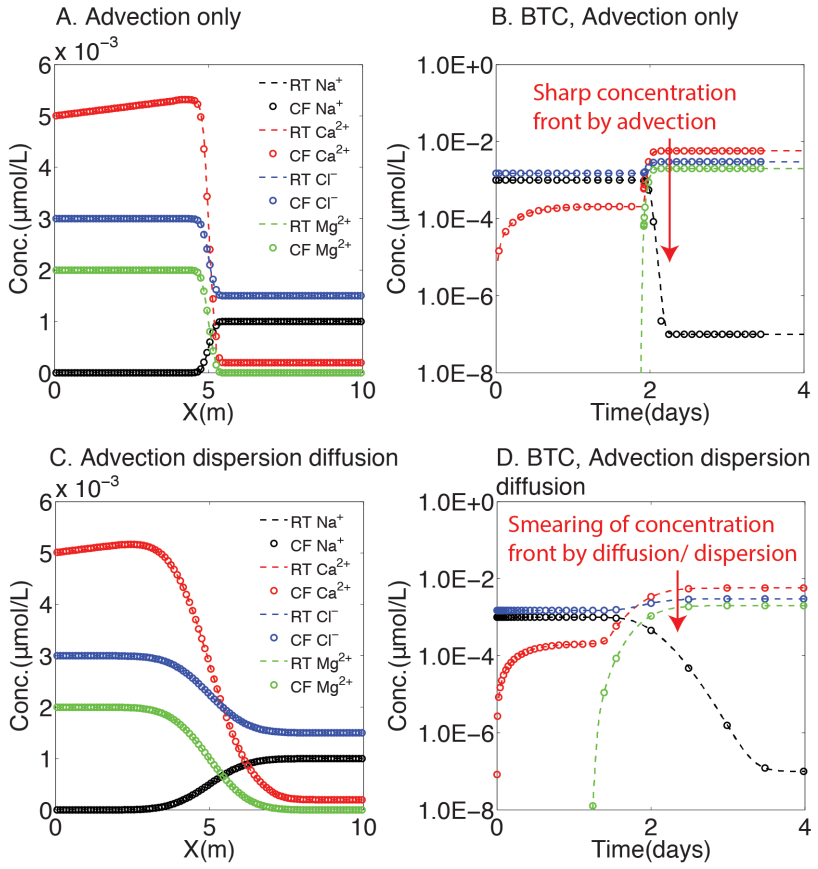

Figure 2-4. Comparison of results from RT and CrunchFlow. A: spatial distribution of solutes on day 2 (half residence time) for advection-only case. B: breakthrough curves (BTC) for advection-only case. RT and CF generated almost identical results except for slight difference at the sharp concentration front. Magnesium originally in the column was all adsorbed onto surface sites so no magnesium broke through at the outlet before 1.9 days. The sharp front suggests good remediation of numerical dispersion. C: spatial distribution of solutes on day 2 in the case with advection, diffusion and dispersion. D: breakthrough curves for the case with advection, diffusion and dispersion. RT and CF generated essentially identical solutions in both cases.

For the advection-only case, both codes successfully capture the sharp concentration fronts produced by advection. Solutions from RT and CrunchFlow have relative differences of less than 10^{-8} in the smooth regions and relative differences in the order of $<10^{-4}$ at the sharp front. For the second case with diffusion and dispersion, solutions from the two codes are almost identical with relative error less than 10^{-8} everywhere. The similar breakthrough curves for

magnesium in RT and CrunchFlow suggests that RT can simulate ion exchange reactions accurately.

4. Model Demonstration

In the section we demonstrate the application of RT-Flux-PIHM in SSHCZO, a V-shaped, first order watershed in central Pennsylvania (Brantley et al., 2006; Duffy et al., 2009; Qu and Duffy, 2007a). We discuss the model set-up first and then the hydrological and geochemical reaction coupling during a large rainfall event. We focus on the dynamics of water content, the non-reactive tracer Cl mostly originated from the rainfall, and a reactive species Mg derived from clay dissolution in the watershed. For reactive transport, we compare two cases here. In one case, Mg dissolves from chlorite however does not participate in ion exchange (w/o CEC). In another case, Mg also participates in ion exchange reactions (w/CEC). The discussion is kept relatively brief to illustrate the salient capabilities. More detailed application and illustration are shown in the companion paper (Bao et al., 2016).

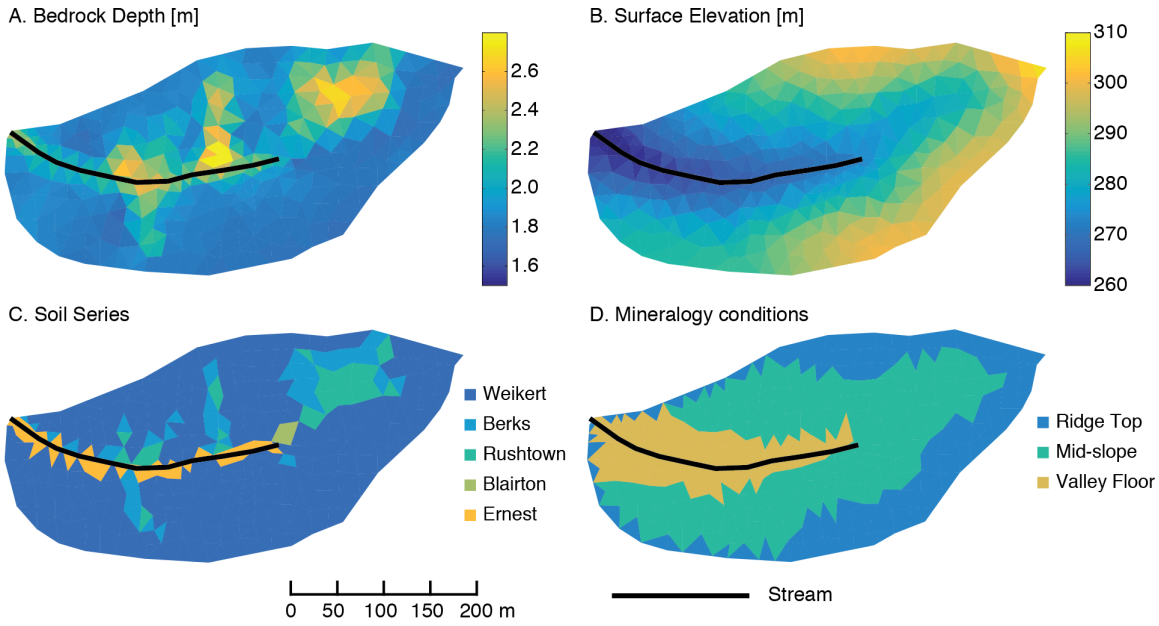

Figure 2-5. Spatial distribution of key topographic and soil properties in SSHCZO based on extensive field surveys and existing modeling work calibrated by using multivariate field measurements. A: depth to bedrock [m]; B. surface elevation [m]; C: identified soil series; D: Zones of different geochemical initial conditions assigned based on field measurements (Jin et al., 2010).

Model setup. RT-Flux-PIHM allows watershed initialization with spatial heterogeneities in both physical and chemical properties. Extensive field surveys have provided spatial distribution of the topographic and hydrological properties (Jin et al., 2010; Lin, 2006; Ma et al., 2010). In this work, we use the spatial distribution of measured soil thickness, soil elevation, soil series and mineralogy from previous work (Jin and Brantley, 2011; Jin et al., 2010; Lin, 2006), as shown in Figure 2-5. Prior to this work, the hydrological parameters for hydrological land surface processes have been carefully calibrated using multiple field measurements (discharge, soil moisture, water table depth, and surface heat fluxes) in 2009 (Shi et al., 2013).

As discussed before, chloride is a non-reactive tracer originated from atmospheric deposition. Chlorite dissolution in the shallow regolith releases magnesium (Jin et al., 2014). Magnesium also participates in cation exchange reaction (Jin et al., 2010). The surface reactions and its thermodynamic and kinetic parameters are shown in Table 2-4. The primary species here is the H^+, HCO_3^-, and cations derived from chlorite dissolution. Aqueous complexation reactions are considered here with the secondary species being OH^-, $CO_2(aq)$, CO_3^{2-}, $MgCO_3(aq)$, $MgCl^+$, and $MgHCO_3^+$.

Table 2-4 Reactions and reaction thermodynamics and kinetics

Chlorite dissolution	$\log_{10}K_{eq}$	$\log_{10}k$ (mol/m^2/s)	Specific surface area (SSA, m^2/g)
$(Fe_{0.24}Mg_{0.38}Al_{0.38})_6(Si_{0.07}Al_{0.93})_4O_{10}(OH)_{8\,(s)}$ *(chlorite)*+ 5.72 $H_4SiO_{4\,(aq)}$ + 4.56 H^+ → 1.44 $FeOOH_{(s)}$ + 2.28 Mg^{2+} + 3$Al_2Si_2O_5(OH)_{4\,(s)}$ + 11 H_2O	38.8	-12.5[a]	0.01 (1.1~7.7)[a]
Cation exchange reaction[f]			
X_2Mg + 2H^+⇔ >2HX + Mg^{2+}	0.50[b]		

[a]: values in brackets for comparison from (Aylmore et al., 1970; Köhler et al., 2005; Köhler et al., 2003) [b]: derived from (Jin et al., 2010) using Vanselow convention (Vanselow, 1932).

Hydrogeochemical dynamics during a large rainfall event. Large rainfall events are expected to significantly influence reactions and transport in the watershed (McGuire and McDonnell, 2010; Torres et al., 2015). Here we simulated the watershed water and geochemical dynamics in SSHCZO during a large rainfall event on Oct. 23rd ~ 24th in 2009. The spatial distributions of water storages (h_u, h_g), solute concentrations and mineral dissolution rates are demonstrated in Figure 2-6. In general, the topography of the watershed has a large control over the spatial distribution of water content and reactions. Higher dissolution rates and more Mg mass on the exchange sites occur in areas with converging flow and higher water content, including swales and valley floor. During the rainfall event, water storage in both unsaturated and saturated zones increased due to the water infiltration and recharge into the unsaturated and saturated zones (Figure 2-6 AB). Interestingly, the unsaturated zone water storage quickly restored to its level before the rainfall, while the saturated zone sees sustained water storage even after four days of the rainfall event, reflecting the slower flow out of the saturated zone.

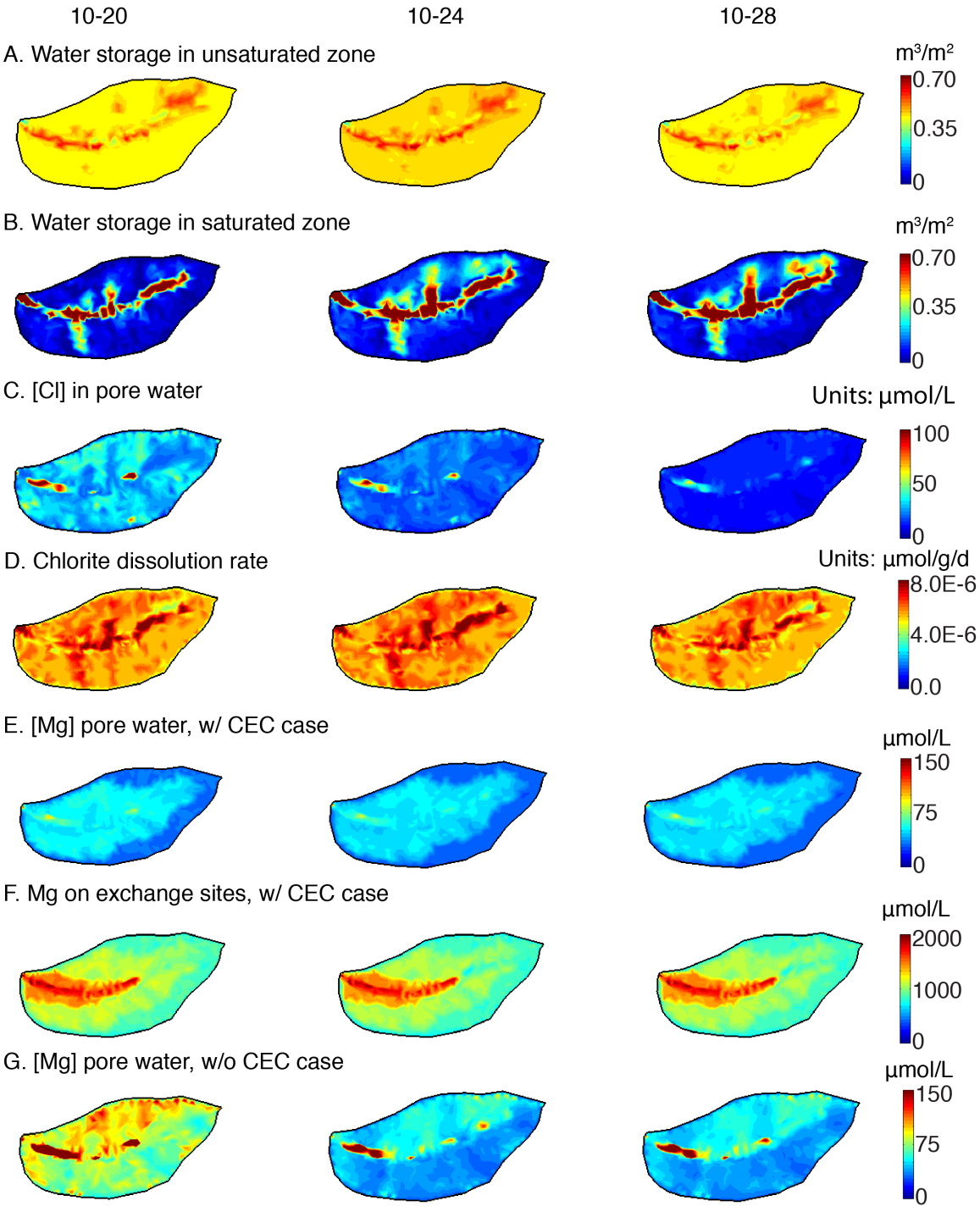

Figure 2-6 At selected time (before, during and after the rainfall event under investigation), . A: water storage h_u in the unsaturated zone [m^3/m^2]; B: water storage h_g in the saturated zone [m^3/m^2]; C: [Cl] [µmol/L-pore water]; D: chlorite dissolution rate [µmol/g-soil/d]; E: [Mg] in pore water for w/ CEC case [µmol/L-pore water]; F: Mg on exchange sites, w/ CEC case [µmol/L-pore water]; G: [Mg] in pore water for w/o CEC case [µmol/L-pore water].

The [Cl] in pore water was relatively high before the rainfall event and dropped quickly due to the flush out during the rainfall event (Figure 2-6C). During the rainfall, chlorite dissolution rates are in general higher due to the higher water content (Figure 2-6D). The spatial distribution of the water content essentially dictates the highs and lows of local dissolution rates. For Mg, pore water concentrations remain relatively constant in the case with cation exchange reaction while Mg on exchange site decreases during the rainfall (Figure 2-6EF). The soil surface has much more Mg than in pore water and serves as a large buffering reservoir. In the case without ion exchange (w/o CEC), the relatively higher Mg pore water concentration before the rainfall dropped quickly and was much more responsive to the rainfall event. The depletion of Mg due to rainfall is much more pronounced without the buffering capacity of ion exchange (Figure 2-6G).

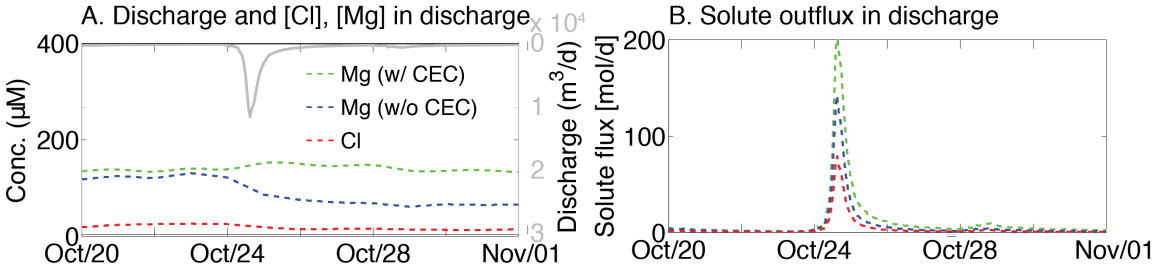

Figure 2-7. Predicted discharge, concentrations, and fluxes as a function of time during a large rainfall event on oct. 24, 2009. A: discharge and [Cl], [Mg] (w/ CEC and w/o CEC) at the stream outlet. B: solute outflux as a function of time.

Although discharge increased by more than two orders of magnitude from 51.44 m^3/d to 1.15×10^4 m^3/d, solute concentrations at the stream outlet are surprisingly stable (Figure 2-7A). Our model shows that with ion exchange, [Mg] at the stream outlet is stable and even increased slightly. This is because the release of Mg from exchange sites compensates for the losses of Mg from elevated discharge. In contrast, without ion exchange, [Mg] at the stream outlet dropped to approximately half of its pre-rainfall concentration, behaving similarly like [Cl]. As a result, Mg

fluxes are highest during the rainfall event with ion exchange, flushing out magnesium that is previously on cation exchange sites.

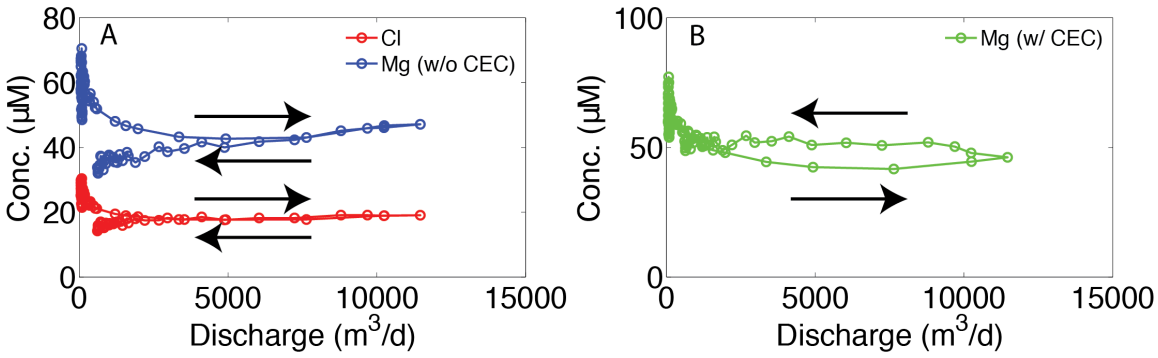

Figure 2-8. CQ hysteresis plots from hourly output of RT-Flux-PIHM simulation from Oct. 22 to 26, 2009, when a large precipitation event occurred on Oct. 24. Black arrows indicate the rising limb (arrow pointing to the right) and recession limb (arrow pointing to the left).

Finer temporal resolution in model outputs would allow us to further investigate the impact of episodic rainfall events in much greater detail. Here we show the predicted hourly output of stream outlet concentration and stream discharge between Oct. 22nd and Oct. 26th (Figure 2-8). It has often been observed that concentrations at certain discharge of the rising limb (early stage of rainfall) differs from those at the same discharge in a recession limb (late stage of rainfall) (Hendrickson and Krieger, 1964; Toler, 1965). This phenomenon, often called hysteresis, has been attributed to different arrival times of solute and discharge (Walling and Foster, 1975), mixing of different components (Hooper et al., 1990), and the combination of the two (Evans and Davies, 1998).

Our simulation results show that [Cl] started high in the early stage of the rainfall due to the accumulation before the rainfall event. The rainfall flushed out Cl and lowered its concentration in the recession limb. The hysteresis at high discharge however is relatively small (Figure 2-8A). Only at low discharge of rising and recession limbs [Cl] are very different. Magnesium behaves very similarly to Cl when cation exchange is absent, except that it generally

has higher concentrations compared to Cl. Neither [Cl] nor [Mg] without ion exchange is restored to the pre-rainfall level so no hysteresis loop is formed.

With cation exchange, Mg exhibited stronger hysteresis loop during the rainfall event. The Mg concentration was constantly lower in the rising limb than that of the recession limb at any given discharge (Figure 2-8B). This is because the fast surface runoff with low [Mg] concentration reached stream quickly and contributed substantially to the stream outlet during the rising limb, such that [Mg] at the outlet is low. During the recession limb, much of the discharge water came from the slower subsurface flow carrying much higher [Mg] released from ion exchange, therefore maintaining relatively higher concentration in the stream. The difference in the [Mg] concentrations in the rising and recession limbs, however, are relatively small compared to the more than two orders of magnitude variation in discharge.

Cation exchange also led to a restoration of [Mg] to before the rainfall event, therefore forming a closed CQ hysteresis loop. This hysteresis loop corresponds to the A3 type defined by Evans and Davies (1998). This is a result of higher solute concentrations in groundwater and soil water than those in surface runoff. Although we only have two components in our system (subsurface water, surface runoff), A3 type hysteresis still occur with cation exchange reaction. The role of ion exchange in determining the characteristics of hysteresis loop has rarely been discussed in previous studies.

5. Conclusion

RT-Flux-PIHM offers a much-needed modeling tool to integrate land-surface interactions, hydrological and geochemical processes at the watershed scale. It provides capabilities of mechanistic understanding on energy, water, and flux coupling at the watershed scale, and identification of key processes and emergence behavior. Here we demonstrate the model capability by investigating the chloride and magnesium dynamics during a single rainfall

event in SSHCZO. The model shows the spatial distributions of soil weathering are controlled by topographic features where flow converges. It also indicates the importance of ion exchange in buffering and keeping relatively constant Mg concentrations. The ion storage capacity of exchange sites leads to hysteresis of Mg concentration-discharge relationship during the large rainfall event. The example shows the potential of using RT-Flux-PIHM as a tool for virtual experiments under a variety of topography, hydrological, and geochemical conditions, enabling the resolution of long-standing puzzles in watershed hydrogeochemistry.

6. Numerical Treatment of RTM

6.1 Mass Action Law

Although the advection diffusion dispersion equation holds true for any individual species that exists in the fluids, the number of total equations to be solved in each control volume could be reduced because of the "mass action law".

For each individual species:

$$\frac{\partial}{\partial t}(\phi V C_i) + \nabla(-\boldsymbol{D}\nabla(C_i\Theta_i) + \boldsymbol{u}C_i\Theta_i) + \left(R_i^{eq} + R_i^{kin}\right) + S_i = 0 \qquad (18)$$

Where $R^{eq}{}_i$ is the rate of reaction in chemical equilibrium and $R^{kin}{}_i$ is the rate of kinetic reaction [mol/s]. In general, if a reaction reaches its equilibrium within a short time, it is classified as equilibrium-controlled reaction. For each of the equilibrium-controlled reactions simulated in the system, concentration of one chemical species in that reaction becomes a function of the concentrations of other species in that reaction and the chemical equilibrium constant. Therefore, because of equilibrium-controlled reactions, usually only a fraction of chemical species are independent variables. The system with N_{tot} chemical species could then be

represented by N_c independent chemical species plus $N_x=N_{tot}$ - N_c chemically dependent species (Kirkner and Reeves, 1988). We would call the N_c independent chemical species as primary species, and other species secondary species. Partitioning between primary species and secondary species are not unique. We can have different set of primary species/ secondary species combination for the same problem.

If a secondary species is generated by equilibrium controlled reactions:

$$A_i \rightleftharpoons \sum_{j=1}^{N_c} v_{ij} A_j \, (i = 1,...N_x) \tag{19}$$

Where A_i and A_j is the chemical formula of the primary and secondary species in the reaction; v_{ij} is the stoichiometry coefficient of the species in this reaction. For each equilibrium-controlled reaction, we can then write the **Mass Action Law** that is

$$X_i = K_i^{-1} \gamma_i^{-1} \prod_{j=1}^{N_c} (\gamma_j C_j)^{v_{ij}} \, (i = 1,..., N_x) \tag{20}$$

Where K_i is the equilibrium constant for the equilibrium controlled reaction, γ_i is the activity coefficient of the species i; X_i is the concentration of secondary species i [mol/m^3].

The production rate of a primary species due to equilibrium-controlled reaction can be written in terms of the sum of production rates of the secondary species due to the same equilibrium-controlled reaction (Kirkner and Reeves, 1988).

$$R_j^{eq} = -\sum_{i=1}^{N_x} v_{ij} R_i^{eq} \tag{21}$$

Where $R^{eq}{}_i$ is the production rate of secondary species i and $R^{eq}{}_j$ is the production rate of primary species j in this equilibrium controlled reaction. This leads to a reduction of total numbers of ADR equations by:

$$\frac{\partial}{\partial t}\left[\phi V(C_j + \sum_{i=1}^{N_x} v_{ij} X_i)\right] + \nabla\left\{-\boldsymbol{D}\nabla\left[(C_j + \sum_{i=1}^{N_x} v_{ij} X_i)\Theta_j\right] + \boldsymbol{u}(C_j + \sum_{i=1}^{N_x} v_{ij} X_i)\Theta_j\right\} + R_j^{kin} + S_{j,tot} = 0 \tag{22}$$

If we further define the **Total Analytic Concentration** for a given primary species as:

$$U_j = C_j + \sum_{i=1}^{N_x} v_{ij} X_i \tag{23}$$

$$\frac{\partial}{\partial t}\left[\phi V U_j\right] + \nabla\left\{-\boldsymbol{D}\nabla\left[U_j\right]\Theta_j + \boldsymbol{u} U_j \Theta_j\right\} + R_j^{kin} + S_{j,tot} = 0 \tag{24}$$

6.2 Debye–Hückel Model For Species Activity

Only a fraction of molecules of a chemical species will participate chemical reaction. The fraction that actively reacts is often referred activity (Pitzer, 1977):

$$a_i = \gamma_i C_i \tag{25}$$

We used an extended Debye–Hückel Equation to compute for the activity coefficient of chemical species:

$$\log \gamma_i = -\frac{A_T Z_i^2 (I)^{1/2}}{1 + B_T \alpha_i (I)^{1/2}} + b_T I \tag{26}$$

where γ_i is the activity coefficient of species i; A_T, B_T and b_T is the temperature dependent Debye–Hückel parameters that can be looked up in the database; Z_i is the charge of species i; I is the ionic strength of the solution:

$$I = \frac{1}{2}\sum_{i}^{N_{tot}} (C_i Z_i^2) \tag{27}$$

6.3 Influences of Temperature on Kinetic Reactions

Since Flux-PIHM also simulates the temperature evolution in the subsurface, the influence of temperature changes on kinetic reactions are also considered in RT-Flux-PIHM model:

$$\ln(\frac{k}{k_{ref}}) = -\frac{E_a}{R}(\frac{1}{T} - \frac{1}{T_{ref}}) \quad (28)$$

where k is the rate constant for kinetic reaction [mol/m^2/s]; k_{ref} is the rate constant in the reference temperature, which is 298.15K in RT-Flux-PIHM; E_a is the activation energy [J/mol]; R is the gas constant [J/mol/K]; T is the soil temperature [K] and T_{ref} is 298.15K. The soil temperature T here is a volumetric weighted average of soil temperatures readings from four soil layers (0~5 cm, 5 ~ 25 cm, 25 ~ 70 cm and 70 ~ 150 cm).

6.4 Finite Volume Based Reactive Transport Model

Solving the set of abovementioned partial differential equations numerically requires spatial discretization of the field. The method and the quality of such spatial discretization are vital to the accurate solution of the system. In addition, physical and chemical parameters of porous media are often distributed heterogeneously in natural systems (Li et al., 2011). Spatial discretization is also expected to account for these heterogeneities. Multiple numerical discretization methods have been proposed. Those methods can be generally categorized into three groups: finite difference methods (FDM), finite volume methods (FVM) and finite element methods (FEM).

Traditionally, finite difference methods are predominantly used in reservoir engineering simulators (Ertekin et al., 2001) as well as hydrological simulators like PARFLOW-Surface-Fow

(Kollet and Maxwell, 2006), MODHMS (Panday and Huyakorn, 2004) for flow field simulation. For mass transfer and reactions, majority of the existing reactive transport algorithms uses finite difference methods as well, including CRUNCHFLOW (Steefel, 2008; Steefel and Lasaga, 1994), FLOTRAN (Holder et al., 2000; Lu and Lichtner, 2005), STOMP (White and McGrail, 2005; White and Oostrom, 2000), MIN3P (Mayer et al., 2002), etc.

In recent years, finite volume method has been widely utilized by both petroleum engineering community (Cao and Aziz, 2002) and hydrology community (Kumar et al., 2009a). Many reactive transport algorithms are adopting FVMs too, including TOUGHREACT (Xu et al., 2008). When applied on a regular structured rectangular grids, the spatial approximation generated by FVMs is equivalent to that generated by FDMs. The benefit of such an transition lies in the fact that FVMs are better at handling the irregularities in boundary conditions and local heterogeneities because of its compatibility with unstructured grids (Kumar et al., 2009a). On the other hand, FDMs are usually more computationally economical because of the ease in determining the derivatives of state variables in rigid, structured grids.

Lastly, finite elements methods (FEM) are widely used in heat transfer, aerospace engineering, mechanical engineering and computation fluid dynamics (CFD) community (Reddy, 1993). However, there are only a few applications of FEM in porous flow simulations or reactive transport simulations, including HYDROGEOCHEM (Yeh et al., 2004), TRANQUI (Xu et al., 1999).

For a coupled system, the selection of the spatial discretization method for reactive transport model also depends on the spatial discretization of the flow field simulation. In order to directly use the flow field information generated by the later model, the spatial discretization method used for the former model should be compatible to the method used in the later model. By compatible, we mean the gridding system used in the later model could be directly used in the former model. Otherwise, interpolation in the flow field is required before running reactive

transport model. The compatibility of the three methods discussed could be summarized in the following table:

Table 2-5 Compatibility of Spatial Discretization Methods In A Coupled System

	Reactive Transport Simulation		
Flow Field Simulation	FDM	FVM	FEM
FDM	Compatible	Compatible	Incompatible
FVM	Incompatible	Compatible	Compatible *
FEM	Incompatible	Compatible	Compatible

* FEM is only compatible to FVMs with triangular or tetrahedral grids.

Among the methods discussed, FVMs appear to be most versatile in accommodating to the existing gridding structure of the flow simulator. A FVM based reactive transport code would be inherently compatible with any types of gridding system that the flow simulation utilizes. This compatibility eliminates the need to translate flow field information from one gridding system to another, therefore saves computational time and retains accuracy. Flux-PIHM also uses finite volume method.

As a result, in this work, we used finite volume method to solve for the advection diffusion reaction equation for reactive transport of multi-species. Finite volume method could be conceptualized as a system where each of the elements is treated as a control volume with discrete volume. Mass is conserved over every of the control volumes by enforcing the net change of mass in this control volume be equal to the input of mass minus the output of mass for each of all chemical species. The control volume could be of any shape but most frequently it is a polyhedron:

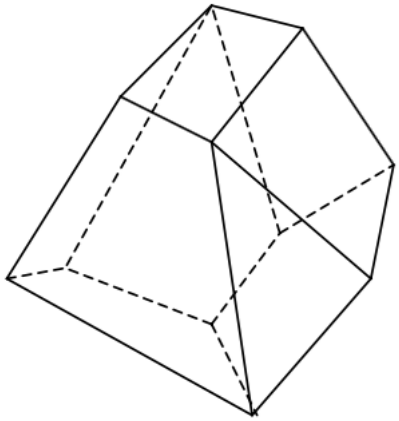

Figure 2-9 A polyhedron

In RT-Flux-PIHM, the finite volumes are triangular prisms. In the subsequent section, we will discuss in detail how reactive transport equations are solves in a finite volume manner in RT model.

6.5 Sequential Non-Iterative Approach (SNIA)

The RT module follows a sequential non-iterative approach (SNIA) that has been widely applied (Walsh et al., 1984; Yeh and Tripathi, 1989). This approach is efficient in integrating subsurface flow simulation with reactive transport algorithms with some limits noted (Jacques et al., 2006). The SNIA is a derivative of the operator-splitting method that decouples ADR equation and solves transport and reaction steps separately (Xu et al., 1999; Zysset et al., 1994). In the RT module, the transport step is solved using the Euler forward method while the reaction step is solved iteratively using the Crank–Nicolson and Newton Raphson method. In the reaction step, the local matrices accounting for the mass balance of all primary species in each finite volume are assembled and solved using a matrix solver in SUNDIALS (Hindmarsh et al., 2005).

The accuracy of the SNIA approach depends on multiple factors including spatial discretization, time stepping, and flow conditions. To minimize numerical errors and improve convergence, we adopted the approach in Jacques et al. (2006). Performance index (PI) and

maximum allowable time step are used to optimize the time stepping. PI is set to be less than 0.05 for every shared surface between elements to minimize the operator splitting error associated with temporal discretization (Jacques et al., 2006; Perrochet and Bérod, 1993):

$$\frac{u_{ij}^2}{D_{ij}}\Delta t < 0.05 \tag{29}$$

where Δt is the time step, u_{ij} and D_{ij} is the velocity and mode of the dispersion tensor from volume i to j, respectively. The allowable maximum time step is set to be 1 minutes (Jacques et al., 2006) by default or could by redefined by user through input file. The final time step in the algorithm will be the minimum of the Δt obtained from equation (31) and the maximum time step. The use of small PI and maximum time step requires a longer computational time; however, this improves the SNIA accuracy.

The numerical procedures carried out in RT between time n and time $n+1$ could be summarized as:

$$\frac{\phi V(S_W^{n+1}U_j^{n+1,pre-reaction,} - S_W^n U_j^n)}{\Delta t} + \nabla\left\{-\boldsymbol{D}\nabla\left[U_j\right] + \boldsymbol{u}U_j\right\} + S_{j,tot} = 0 \tag{30}$$

$$\frac{\phi S_W^{n+1}V(U_j^{n+1,after-reaction,} - U_j^{n+1,pre-reaction})}{\Delta t} - R_j^{kin} = 0 \tag{31}$$

Considering the fact that Flux-PIHM uses area normalized fluxes and water heights as variables, the above equations could be further written into:

$$\frac{\phi(h_{u|g,k}^{n+1}U_j^{n+1,pre-reaction,} - h_{u|g,k}^n U_j^n)}{\Delta t} + \sum_{l=1}^{3}\left\{-D_{lk}\nabla\left[U_j\right] + A_k q_{lk}U_j\right\} + S_{j,tot} = 0 \tag{32}$$

where D_{lk} is the dispersion tensor at the interface of element l and k; A_k is the base area of the prismatic element k; q_{lk} is the area normalized flux from element l to k.

$$\frac{\phi h_{u|g}^{n+1}(U_j^{n+1,after-reaction,} - U_j^{n+1,pre-reaction})}{\Delta t} - R_j^{kin} = 0 \quad (33)$$

We used Crank-Nicolson method to evaluate the exact value of R^{kin}_j right after each iteration:

$$\left(R_j^{kin}\right)^{n,t+\frac{1}{2}} = \frac{1}{2}\left[\left(R_j^{kin}\right)^{n,t} + \left(R_j^{kin}\right)^{n,t+1}\right] \quad (34)$$

where $(R^{kin}_j)^{n,t+1}$ is the rate evaluated based on the concentrations of chemical species at the time *n* and iteration *t+1*.

which leads to

$$\frac{\phi h_{u|g}^{n+1}(U_j^{n+1,after-reaction,} - U_j^{n+1,pre-reaction})}{\Delta t} - \frac{1}{2}\left[\left(R_j^{kin}\right)^{n,t} + \left(R_j^{kin}\right)^{n,t+1}\right] = 0 \quad (35)$$

Equation 34 and 37 are the two equations that are solved in RT component of RT-Flux-PIHM. The first equation is solved using an Euler forward method (os3d.c) and the second equation on chemical reaction is iteratively solved using Crank–Nicolson method and Newton Raphson method for each of the elements in the field (react.c).

6.6 Local Jacobian Matrix for Kinetic Reactions

To solve equation 37, Newton Raphson method is implemented. First, we define the evaluation functions of each of the total analytic concentrations:

$$f_j(U_j) = \frac{\phi h_{u|g}^{n+1}(U_j^{n+1,after-reaction,} - U_j^{n+1,pre-reaction})}{\Delta t} - \frac{1}{2}\left[\left(R_j^{kin}\right)^{n,t} + \left(R_j^{kin}\right)^{n,t+1}\right] \quad (36)$$

For a total of N_x species, we end up with N_x such evaluation functions:

$$f(\mathbf{U}) = f\left(\begin{bmatrix} U_1 \\ U_2 \\ \cdots \\ U_{N_x} \end{bmatrix}\right) = \begin{bmatrix} f_1(U_1) \\ f_2(U_2) \\ \cdots \\ f_{N_x}(U_{N_x}) \end{bmatrix} \tag{37}$$

where **U** is the vector of total analytic concentration from species *1* to species N_c.

The corresponding Jacobian Matric for this evaluation function becomes:

$$\mathbf{J} = \begin{bmatrix} \frac{df_1}{dU_1} & \frac{df_1}{dU_2} & \cdots & \frac{df_1}{dU_{N_c}} \\ \frac{df_2}{dU_1} & \frac{df_2}{dU_2} & \cdots & \frac{df_2}{dU_{N_c}} \\ \cdots & \cdots & \cdots & \cdots \\ \frac{df_{N_c}}{dU_1} & \frac{df_{N_c}}{dU_2} & \cdots & \frac{df_{N_c}}{dU_{N_c}} \end{bmatrix} \tag{38}$$

The exact values of the entries in **J** in each iterative step could be evaluated by using numerical perturbation method:

$$\frac{df_j}{dU_j} = \frac{f_j(U_j + \Delta U) - f_j(U_j)}{\Delta U} \tag{39}$$

In the chemical reaction system, it would be more convenient to mark the entries in the Jacobian matrix that will be always zeros in the initialization stage. Then in each solving process, those entries with a zero mark will not be evaluated to save CPU time:

$$\mathbf{J}^* = \begin{bmatrix} \frac{df_1}{dU_1}\delta_{11} & \frac{df_1}{dU_2}\delta_{12} & \cdots & \frac{df_1}{dU_{N_c}}\delta_{1N_c} \\ \frac{df_2}{dU_1}\delta_{21} & \frac{df_2}{dU_2}\delta_{22} & \cdots & \frac{df_2}{dU_{N_c}}\delta_{2N_c} \\ \cdots & \cdots & \cdots & \cdots \\ \frac{df_{N_c}}{dU_1}\delta_{N_c1} & \frac{df_{N_c}}{dU_2}\delta_{N_c2} & \cdots & \frac{df_{N_c}}{dU_{N_c}}\delta_{N_cN_c} \end{bmatrix} \quad (40)$$

where δ_{ij} is the dependency function of f_i on U_j. If f_i is dependent on U_j, δ_{ij}=1, otherwise δ_{ij} = 0. Entries with δ_{ij} = 0 will not be evaluated in the iterative solver process, thusly saving CPU time.

The iterative solving process then is:

$$\mathbf{U}^{n+1} = \mathbf{U}^n - [\mathbf{J}^*(\mathbf{U}^n)]^{-1} f(\mathbf{U}^n) \quad (41)$$

The iterative process stops if the improvement between steps is smaller than a predefined threshold:

$$\left|\mathbf{U}^{n+1} - \mathbf{U}^n\right| \le \gamma \quad (42)$$

where γ is the threshold of accepting a solution.

6.7 Speciation For Equilibrium Controlled Reactions

In reactive transport model, only the total analytic concentrations of the independent species are solved. After reaching the solution for the total concentrations, additional steps are required to obtain the concentration of all the individual species. This process is often called "Speciation" in RTMs.

In this section, we will discuss the process of using Newton Raphson method to perform the speciation operation. Let us start from Mass Action Law discussed in earlier section. It will be simpler if we first express the concentration of secondary species into a logarithmic form:

$$X_i = K_i^{-1}\gamma_i^{-1}\prod_{j=1}^{N_c}(\gamma_j C_j)^{v_{ij}}, (i = 1,...,N_x) \tag{43}$$

$$\log 10(X_i) = -\log 10(K_i\gamma_i) + \sum_{j=1}^{N_c} v_{ij}\log 10(\gamma_j C_j) \tag{44}$$

This could be also expressed in a matrix vector multiplication operation:

$$\mathbf{X} = \begin{bmatrix} \log 10(X_1) \\ \log 10(X_2) \\ \dots \\ \log 10(X_{N_x}) \end{bmatrix} = -\begin{bmatrix} \log 10(K_1\gamma_1) \\ \log 10(K_2\gamma_2) \\ \dots \\ \log 10(K_{N_x}\gamma_{N_x}) \end{bmatrix} + \begin{bmatrix} v_{1a} & v_{1b} & \dots & v_{1N_c} \\ v_{2a} & v_{2b} & \dots & v_{2N_c} \\ \dots & \dots & \dots & \dots \\ v_{N_x a} & v_{N_x b} & \dots & v_{N_x N_c} \end{bmatrix} \begin{bmatrix} \log 10(\gamma_1 C_a) \\ \log 10(\gamma_1 C_b) \\ \dots \\ \log 10(\gamma_1 C_{N_c}) \end{bmatrix} \tag{45}$$

where **X** is the vector of secondary species concentration. We use [***v***] to represent the matrix with entries v_{ij}. This matrix is also called dependency matrix, because the "dependencies" of secondary species on primary species are stored in this matrix.

If we also express the definition of total concentration:

$$U_j = C_j + \sum_{i=1}^{N_x} v_{ij} X_i$$

in a matrix manner:

$$\mathbf{U} = \mathbf{C} + [v]^T \mathbf{X} \tag{46}$$

or

$$\mathbf{U} = [\mathbf{I} \mid v]^T \begin{bmatrix} \mathbf{C} \\ \mathbf{X} \end{bmatrix} \tag{47}$$

It now becomes easier to see how the Newton Raphson method works for speciation process. Let us define evaluation function:

$$g(\mathbf{C}) = \mathbf{U} - [\mathbf{I} \mid v]^T \begin{bmatrix} \mathbf{C} \\ \mathbf{X} \end{bmatrix} \tag{48}$$

Then the local Jacobian matrix for speciation purpose is:

$$\mathbf{J}_g^* = \begin{bmatrix} \frac{dg_1}{dC_1}\delta_{11,g} & \frac{dg_1}{dC_2}\delta_{12,g} & \cdots & \frac{dg_1}{dC_{N_c}}\delta_{1N_c,g} \\ \frac{dg_2}{dC_1}\delta_{21,g} & \frac{dg_2}{dC_2}\delta_{22,g} & \cdots & \frac{dg_2}{dC_{N_c}}\delta_{2N_c,g} \\ \cdots & \cdots & \cdots & \cdots \\ \frac{dg_{N_c}}{dC_1}\delta_{N_c1,g} & \frac{dg_{N_c}}{dC_2}\delta_{N_c2,g} & \cdots & \frac{dg_{N_c}}{dC_{N_c}}\delta_{N_cN_c,g} \end{bmatrix} \tag{49}$$

where $\delta_{ij,g}$ is the dependency function of g_i on C_j. If g_i is dependent on C_j, $\delta_{ij,g}$ =1, otherwise $\delta_{ij,g}$ = 0. Entries with $\delta_{ij,g}$ = 0 will not be evaluated in the iterative solver process, thusly saving CPU time.

The exact values of the entries in $\mathbf{J}^*_g$ in each iterative step could be evaluated by using numerical perturbation method:

$$\frac{dg_j}{dC_j} = \frac{g_j(C_j + \Delta C) - g_j(C_j)}{\Delta C} \tag{50}$$

Finally, we solve for **C** iteratively:

$$\mathbf{C}^{n+1} = \mathbf{C}^n - [\mathbf{J}_g^*(\mathbf{C}^n)]^{-1} g(\mathbf{C}^n) \tag{51}$$

until the improvement satisfies

$$\left| \mathbf{C}^{n+1} - \mathbf{C}^n \right| < \gamma \tag{52}$$

6.8 Total Variation Diminishing

Numerical dispersion is also a serious concern for large-scale transport simulations with large grid blocks and fast flow dominated by convection (Li and Duffy, 2012). A total variation diminishing technique (TVD), which is third-order accurate in smooth regions, is used to reduce the extent of numerical dispersion (Gupta et al., 1991). This method addresses the numerical dispersion problem by using the concentration at the interface of the element under investigation and the upstream element, instead of the volume averaged concentration of the upstream element:

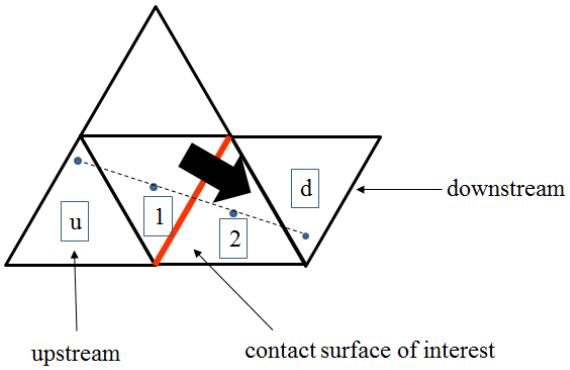

Figure 2-10 Schematic plot of Gupta TVD for unstructured grid

The key to implement this TVD is to estimate the concentration of species at the face between element 1 and element 2. The first step to perform the TVD is to find the (potential) upstream and downstream cell for the pair of element 1 and 2 by using a simple extrapolation of the centroid of element 1 and 2. This search is performed in the initialization stage of the code and is only performed once.

Then the concentration at the interface of element 1 and 2 is calculated as (assuming flow direction is from 1 to 2):

$$C_{12} = C_1 + \beta(r)\left[\frac{C_2 - C_1}{2}\right] \tag{53}$$

Where

$$\beta(r) = \max\left[0, \min\left[2, 2r, \frac{2+r}{3}\right]\right] \tag{54}$$

And r is defined as:

$$r = \left[\frac{C_1 - C_u}{C_2 - C_1}\right] \tag{55}$$

6.9 Adaptive time stepping

In the reaction step, the RT module uses concentrations from the previous time step as the initial guess to iteratively solve for the concentration of the current time step. The spatial heterogeneity in hydrological processes can cause significant non-convergence problems. For example, the flow rates between any two neighboring elements in Shale Hills vary by six orders of magnitude (from 0.01 m^3/d for slowest surface flow to 4000 m^3/d in stream flow during storms). When flow rate anywhere in the simulated domain is fast enough, time steps are reduced to facilitate convergence. Reducing the time steps based on the fastest flow, however, would essentially prevent the model from time marching. Therefore, sub time step interpolation is used in the fast-flow regime to obtain a closer initial guess when non-convergence is encountered.

6.10 Code Structure in RT

In each time step, after Flux-PIHM finishes computation and reached a solution in the water distribution, RT will be called to perform reactive transport simulation based on the flow field information generated in Flux-PIHM. A flow chart of the RT component is provided in the following figure. The source code files responsible for the simulated processes are also indicated in different colors.

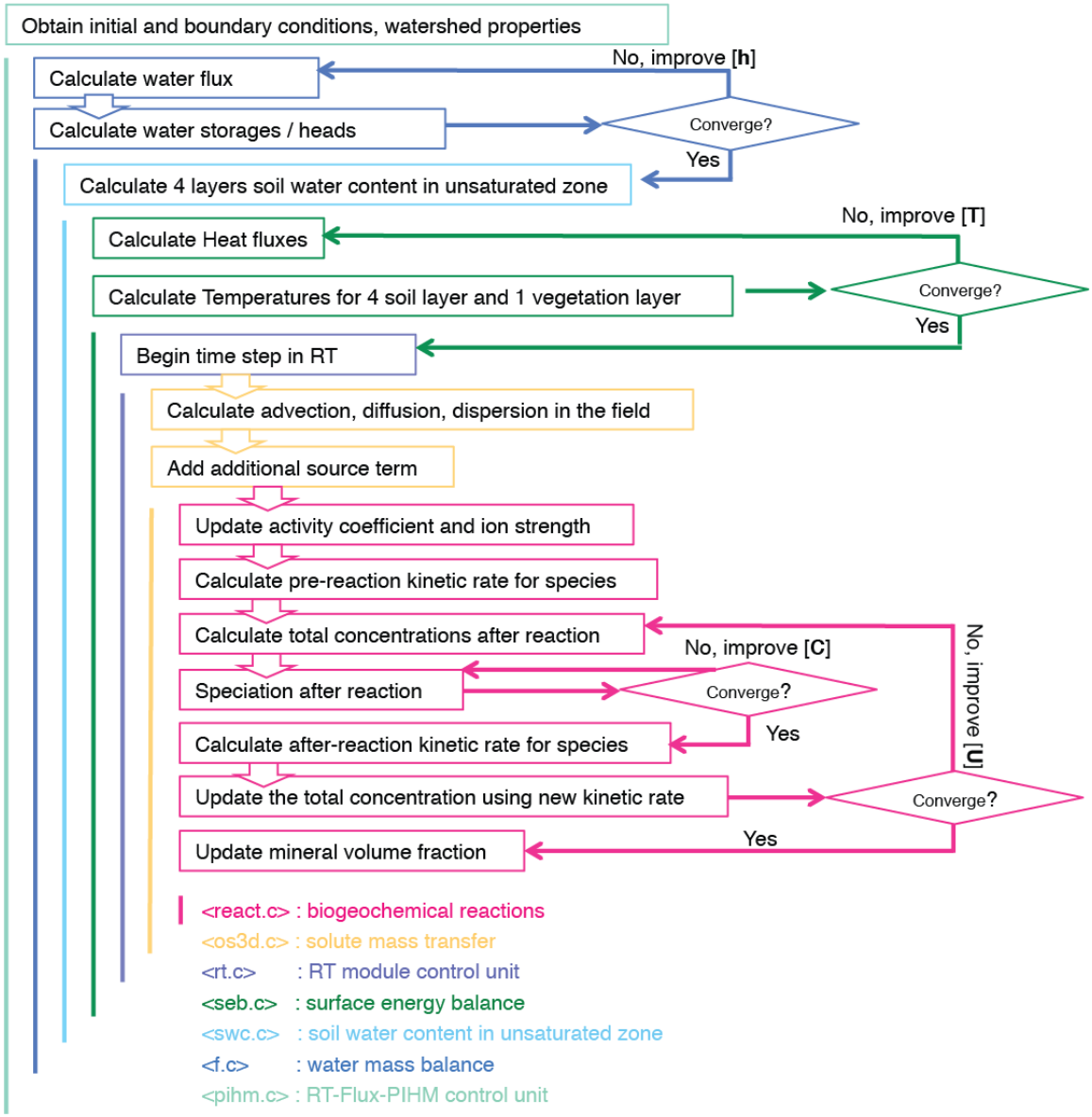

Figure 2-11 Flow chart of RT-Flux-PIHM. [**h**] is the vector of water storages in the field; [**T**] is the vector of temperature in the field. [**C**] is the vector of primary species concentration in the field; [**U**] is the vector of total species concentration in the field. A nested Newton Raphson iteration is performed to solve for concentration evolution resulted from reactions.

Chapter 3

Decoding Concentration-discharge Relationship of Chloride and Magnesium at the Shale Hills Critical Zone Observatory

Abstract

Understanding complex hydrogeochemical processes requires an integrated approach at the watershed scale. Here we used a newly developed hydrological land surface and reactive transport model RT-Flux-PIHM to understand the watershed dynamics of non-reactive tracer Chloride (Cl) and reactive solute Magnesium (Mg) in Susquehanna Shale Hills Critical Zone Observatory (SSHCZO). The model was first calibrated using water chemistry data at the SSHCZO. Overall, the hydrological processes in Shale Hills have a significant influence on the temporal evolution and spatial distribution of chemical species. The watershed is hydrologically more connected (between hillslope and -stream) in the wet spring and winter and flushes out chloride quickly. In the dry summer, however, the watershed is much less connected and Cl is trapped at elevated concentrations along planar hillslopes that do not flush out quickly. Large rainfall events flush out *and* dilute high Cl concentration ([Cl]) pore water that is built up during dry months. This seasonal connectivity regulates [Cl] and leads to relatively constant [Cl] versus discharge (chemostatic). Mg is balanced between its sources (clay dissolution and groundwater influx) and sink (discharge), and is buffered by cation exchange. Cation exchange stores an order-of-magnitude more magnesium than pore water, especially along convergent flowlines (the valley and swales). In contrast to Cl storage that occurs in high concentration pockets along the planar hillslope, cation exchange sites in the valley floor and in swales store most of the Mg mass. In the wet season, faster dissolution is accompanied by higher water volume and discharge The opposite

occurs in the dry summer. The balance of these multiple processes maintains relatively stable [Mg] and [Cl], explaining the chemostatic behavior. The cation exchange reaction helps to homogenize Mg concentration across the watershed however its effects on CQ relationship is secondary. Dilution only occurs when groundwater influx becomes the dominant Mg source. This work demonstrates the potential of RT-Flux-PIHM as an integration tool for resolving long-standing puzzles at the interface of hydrology and geochemistry.

1. Introduction

The spatial distribution of water flow and soil biogeochemical reactions within a watershed is a function of a watershed's architecture, in particular the surface topography and subsurface structure, land-surface interactions that partition energy and ecohydrologic processes that partition water into distinct compartments (atmosphere, trees, soil, groundwater, rivers; (Brooks et al., 2015; Chorover et al., 2011)) (Figure 1). Solute concentrations (C) and discharge (Q) at the river mouth integrate the water and reaction processes at the watershed scale and therefore encode important signatures of hydrology and soil biogeochemical reaction coupling. Concentration-discharge (CQ) relationship has been used to understand the watershed response to hydrological conditions (Anderson et al., 1997; Chanat et al., 2002; Godsey et al., 2009), and estimate loads of nutrients, elements, contaminants and sediments out of watersheds (Campbell and Bauder, 1940; Ferguson, 1986; Stenback et al., 2011). Concentration and discharge data have also been used to understand watershed hydrodynamics and to quantify weathering rates (Gaillardet et al., 1999; Maher and Chamberlain, 2014; Moon et al., 2014; Navarre-Sitchler and Brantley, 2007a; Torres et al., 2015b; White and Blum, 1995).

The CQ relationships for different chemical species are signatures of different processes (Johnson et al., 1969; Kirchner et al., 2000b). The CQ for the non-reactive tracers, for examples,

chloride, encodes the water flow and solute transport processes. Those of geogenic species, including Mg, Na and Si derived from minerals, offer signals of soil weathering. The CQ relationship for bio-relevant species, including dissolved organic carbon (DOC) from soil carbon decomposition, nutrients (N, P), and cations involved in biological processes such as plant uptake and complexation with DOC (e.g., K, Fe, Al), provide insight into the hydrobiogeochemical process coupling (Basu et al., 2010; Grimm et al., 2003; Sebestyen et al., 2008). Chemostatic behavior -- relatively small concentration variation compared to orders of magnitude variations in discharge -- have been observed for a range of geogenic species such as Na, Si, Ca, and Mg for catchments of widely different geochemical and hydrological characteristics (Clow and Mast, 2010; Godsey et al., 2009). In contrast, bio-relevant species often exhibit chemodynamic behavior, where concentrations increase (flushing o/ mobilization) or decrease (dilution) with increasing discharge (Boyer et al., 1997; Herndon et al., 2015b; Musolff et al., 2015; Thompson et al., 2011).

Finding an explanation for the variability of CQ relationships observed for different solutes in different catchments has been a long-standing puzzle in watershed hydrogeochemistry. Efforts to explain this CQ puzzle date back to about half a century ago where Johnson et al. (1969) proposed a mixing model to explain 4 decades of stream Cl data from the Hubbard Brook forest in New Hampshire. More than 3 decades later, Kirchner (2003) still one of the double paradoxes in catchment hydrology and geochemistry being the “rapid mobilization of old water”, the fact that streamflow responds rapidly to the size of the rainfall events while the concentrations of passive tracers (e.g., chloride) and many dissolution-derived cations remain relatively constant (chemostatic behavior). On the other hand, watersheds also release “old” waters of different chemical composition in rainfall events of different size, leading to drastic variations in stream water compositions following rainfall events and different types of non-chemostatic CQ relationships for elements like aluminum and iron (Kirchner, 2003).

The "dampening" of Cl concentration in stream discharge is particularly puzzling because Cl is usually conceived as a non-reactive tracer mainly reflect hydrological process itself (Kirchner et al., 2000a; Peters et al., 1998). Although increasing evidence suggest that Cl is not fully conservative as previous studies assumed (Bastviken et al., 2007; Svensson et al., 2012), the conservativeness of Cl is still a valid approximation because net release/retention has been found to be a only few percent of the total Cl flux for typical watersheds (Svensson et al., 2012; Svensson et al., 2007). Existing studies found that the Cl CQ behaviors in different watersheds range from chemostatic to slightly dilution (Anderson et al., 1997; Johnson et al., 1969; Peters et al., 1998; Stallard and Murphy, 2014). Explanations for Cl chemostatic CQ relationship is largely based on the mixing of different source waters, including old soil water, new rainwater, and groundwater (Chanat et al., 2002; Evans and Davies, 1998; Hooper et al., 1990; Johnson et al., 1969; Stallard and Murphy, 2014). The chemostatic Cl CQ can also be caused by a high ratio of solute residence time in soil to the short hydrological response time using a low dimensional homogeneous bucket model (Duffy and Cusumano, 1998; Gelhar and Wilson, 1974). Catchment-scale dispersion process has also been invoked to explain chemostatic Cl CQ relationship (Kirchner et al., 2000a, 2001). These models consider idealized watersheds with homogeneous physical and chemical conditions without considering the complexity of watershed structure.

The chemostatic CQ relationships of geogenic cations derived from chemical weathering have been attributed to several mechanisms. Godsey et al. (2009) used a permeability-porosity-aperture model to argue that the mineral surface area increases during high discharge, providing more solute due to dissolution to mitigate the dilution effect, leading to a more chemostatic behavior. Maher (2010, 2011) suggested conditions that allow reactions to reach equilibrium. Herndon et al. (2015) attributed the chemostatic behavior to the homogeneous distribution of soil minerals and their quick release from exchange sites during rainfall events. Cation exchange have also been considered as important because it acts as a buffer and sets the lower limit of

concentrations in streams (Clow and Mast, 2010; Jin et al., 2011a). Mountain catchments with steep slope angles have been found to be more "chemostatic" relative to those with shallow slope angles in the foreland floodplain, indicating important links between geomorphic regime and flow characteristics in controlling catchment-scale weathering fluxes (Torres et al., 2015a).

Existing studies provide hypotheses suggesting mechanisms explaining different CQ behaviors under different conditions. In general, a unifying theory that can reconcile different CQ observations and mechanism is still missing. The process-based, systematic-level approach offered by reactive transport models provides the ideal platform to seek such a theory. Here we aim to understand key hydrogeochemical processes using RT-Flux-PIHM, an integrated simulator that enables the coupling of hydrological, land surface and reactive transport processes at the watershed scale (Bao et al., 2016). We apply RT-Flux-PIHM in the Susquehanna Shale Hills watershed (0.08 km^2), a National Science Foundation (NSF) Critical Zone Observatory (SSHCZO) with extensive field measurements and modeling studies (Brantley et al., 2006; Duffy et al., 2009). The capabilities developed through RT-Flux-PIHM provide insights on the spatially-explicit hydrogeochemical dynamics in the watershed. In particular, we focus on hydrogeochemical processes that control Cl and Mg concentrations. Chloride originates from precipitation and is typically considered non-reactive within soils. Its behavior therefore mostly reflects flow and solute transport. In contrast, Mg is mostly derived from clay weathering and participates in ion exchange reactions. We thus study the CQ behavior of both a non-reactive and a reactive tracer.

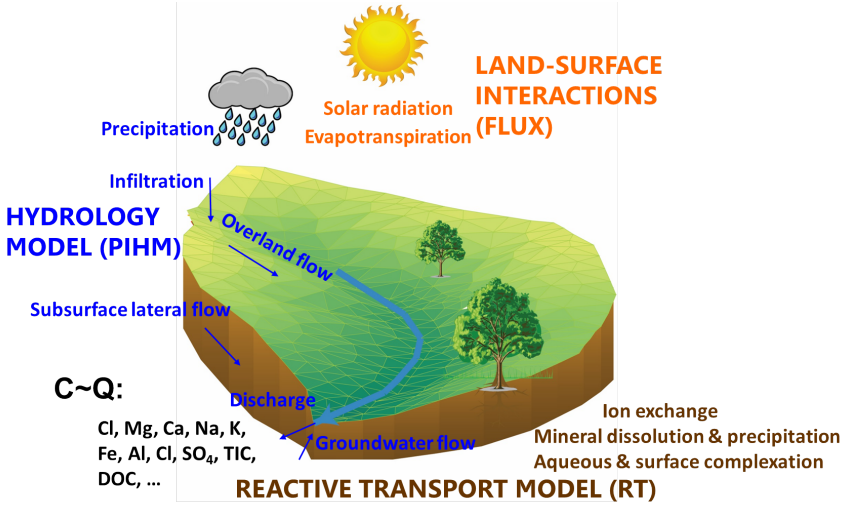

Figure 3-1 A schematic of processes that are incorporated in different modules (shown in different colors) in RT-Flux-PIHM. The model allows systematic understanding of rates and fluxes at the pedon, hillslope, and watershed scales. The watershed, Shale Hills, is located within the Susquehanna Shale Hills Critical Zone Observatory (SSHCZO).

2. The Model, the Site, and Data-Model Integration

RT-Flux-PIHM. As discussed in the companion model development paper (Bao et al., 2016) and shown in Figure 3-1, the PIHM and Flux components solve for the hydrological and land surface processes for water and temperature dynamics within the watershed (Qu and Duffy, 2007b; Shi et al., 2013b). The RT component takes water output from Flux-PIHM, which includes the spatial distribution of water content and flux above the ground surface (runoff), in the unsaturated zone, and the saturated zone below the transient water table in the shallow regolith. The RT component then calculates the spatial and temporal evolution of aqueous and surface concentrations by explicitly including mineral dissolution and precipitation, aqueous complexation, and cation exchange. Mineral dissolution and precipitation are considered as kinetically controlled, while equilibrium-controlled reactions include aqueous complexation and ion exchange. We apply this model to the SSHCZO to elucidate the spatial and geochemical factors controlling CQ behavior.

The Study Site. SSHCZO is a V-shaped, first order watershed in central Pennsylvania (Lin, 2006). The mean annual temperature is 10^{o}C with a mean annual precipitation of 1070 mm (Jin et

al., 2011b). About 50% of the precipitation contributes to evapotranspiration and the other 50% to stream discharge (Jin et al., 2014). Extensive field measurements have been conducted to characterize the topography, hydrological properties and mineral composition in SSHCZO (Brantley et al., 2013a; Hasenmueller et al., 2013; Jin et al., 2014; Jin et al., 2010; Jin et al., 2011c; Lin, 2006; Ma et al., 2010). Measured soil depths from the ground surface vary from less than 0.25 meters at ridge top to 1.87 meters in valley floor (Lin, 2006). At the bottom of this soil, the fractured saprock is permeable and its depth has been quantified at a few boreholes (Brantley et al., 2013a). However, only a small fraction of the incoming water to the catchment infiltrates into the saprock (Sullivan et al., 2016a). In the RT-Flux-PIHM simulation described here, we therefore followed the convention of the previous Flux-PIHM simulations that the depth of this saprock layer is assumed to be 1.5 m and is impermeable beneath that depth across SSHCZO. Therefore the subsurface thickness, the summation of the soil layer and fractured saprock, varies from 1.75 to 3.37 meters across the watershed. The spatial distribution of soil type and soil matrix properties (including porosity and permeability) are from the SSHCZO field survey and have been discussed in previous work (Lin, 2006; Shi et al., 2013b). Measured hydraulic conductivities are used as *a priori* values (Kuntz et al., 2011b) and tuned to reproduce discharge and groundwater level data, as described in Shi et al. (2013). Hydrological and geochemical processes were monitored at high temporal resolution at selected locations, including stream discharge, groundwater table depth, soil moisture, air temperature (Duffy et al., 2010), and chemical composition of streamwater at the watershed outlet and in pore water in 12 lysimeter nests, 6 of which are shown in Figure 3-2.

The interflow from the saturated zone mostly contributes to the stream discharge. These perched zones are connected to the regional groundwater table in the catchment valley. The stream discharge and chemistry at the outlet therefore integrates the water and geochemical dynamics of the whole watershed. RT-Flux-PIHM however does not explicitly model the flow

from deeper groundwater below the fractured saprock. The influx from the deeper groundwater is added into the calculation here to represent the mass influx into the stream, as will be discussed later.

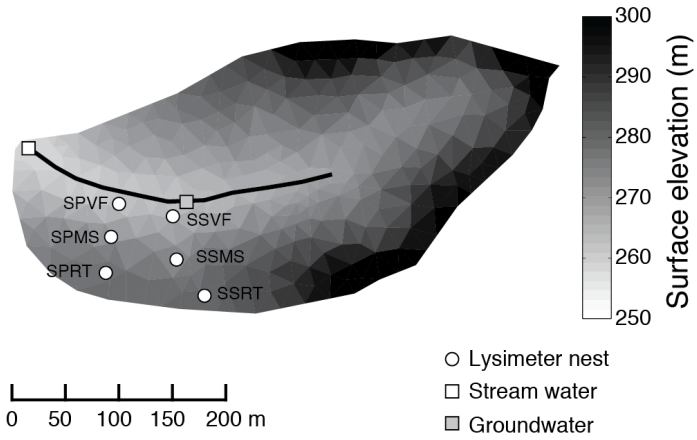

Figure 3-2 Topography of the extensively instrumented SSHCZO. Here we only show the sampling points where key hydrological and geochemical measurements were used in this work. Stream discharge measured at the weir (white square, data available from 2006 to 2012) and the groundwater table depth measured at the groundwater well in the stream riparian zone (grey square, data available from 2007 to 2013) were used to calibrate the land surface hydrological component of the coupled model for 2009 (Duffy, 2013). Water chemistry was measured at 1) lysimeter nests at the south planar sites -- valley floor (SPVF), middle slope (SPMS) and ridge top (SPRT) (data available from Apr. 1st 2008 to Oct. 20th 2011), and at south swale sites -- valley floor (SSVF), middle slope (SSMS) and ridge top (SSRT) (data available from Nov. 9th, 2007 to Oct. 20th, 2011); 2) stream water in the weir at the stream mouth (data available from Oct. 20th, 2006 to Feb. 18th 2011) (Brantley and Sullivan, 2014; Brantley, 2013b, a; Brantley, 2013f, d, e, c; Brantley, 2013g). Measured soil water chemistry was used to calibrate the reactive transport model. The swales are hillslope zones of convergent flow whereas the planar hillslopes are zones of non-convergent flow.

Data-model integration. To simulate the dynamic processes, multiple types of input data are required. The USGS National Elevation Dataset (NED) and the National Land Cover Database (NLCD) provided topography and land cover map with a priori parameters. These data were used initially and were refined later with specific measurements for the watersheds. Watershed characteristics include topography (e.g., soil depth, surface elevation), soil properties (e.g., soil type, soil hydraulic conductivity, porosity, macro pore conductivity, Van Genuchten parameters),

and vegetation properties (e.g., land cover, rooting depth) (Shi et al., 2013c). Watershed initial and boundary conditions include the initial water distribution, water table, snow cover, canopy storage and watershed boundary fluxes. Time series forcing data were either measured at the site or from NLDAS-2 site. These include precipitation, air temperature, wind speed, solar radiation, leaf area index, discharge, and surface heat fluxes that are used to constrain ecohydrological processes. Constraints for geochemical reactions come from measured chemistry of pore water and stream water, as well as soil geochemistry (e.g., mineral composition, surface area, and ion exchange capacity) and soil gases (Hasenmueller et al., 2015; Jin et al., 2014).

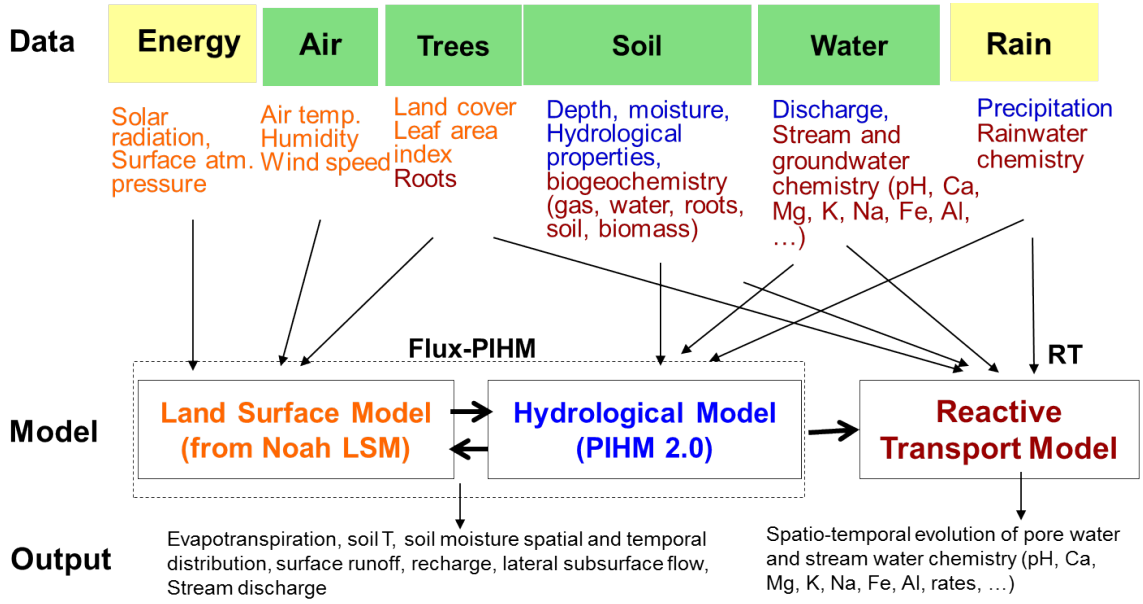

Figure 3-3 Data sources and the structure of data-model integration. The yellow box indicates data from a national database, and the green box indicates data from measurements. Font color indicates connections between data and model. For example, orange colored data provide input or constraints on the orange-colored land surface model. Similarly, the blue colored and brown-colored data are input and/or constraints for the hydrological and reactive transport models with corresponding colors.

Model setup. The code generates unstructured grids based on Delaunay triangulation, considering constraints related to river network, watershed boundary, elevation contours, vegetation, and geology (Qu and Duffy, 2007a). Grids close to rivers and steep areas are typically

small and those in flat, less dynamic areas are large. A total of 535 prismatic elements in the land and 20 stream segments are used in this simulation. The typical mesh size varies from 10 to 100 m. PIHMgis, a tightly-coupled GIS interface to PIHM, was used to setup model domains. The data infrastructure HydroTerre Data System (http://www.hydroterre.psu.edu) harvests, aggregates, and pre-processes essential terrestrial data from federal agencies (e.g., NED and NLCD) (Bhatt et al., 2014). The time step for Flux-PIHM component is set to one minute. The maximum time step for RT component is set to five minutes. In this work, it takes 20~30 hours of CPU time on an Intel ® Xeon ® CPU E5-2670 @ 2.60GHz for 2 years of simulation (2008~2009). The first year (2008) is used as a spin-up, which is run until steady state to avoid unphysical representations of the system. Such unphysical representation can occur if, for example, the initial Mg concentration in the field is too low or too high as compared to what the natural systems can actually maintain. In such cases, the watershed could undergo substantial Mg accumulation or release before reach "steady state", which is unrealistic. The model realizations with different sets of parameters require different spin up time. We manually adjust the spin-up time until the system reaches steady state.

Model evaluation criteria. To evaluate the goodness of simulation results compared to measurements, we used total bias between model output and observations (Moriasi et al., 2007). The total bias (TB) is calculated as follows (Gupta et al., 1999):

$$\text{TB (total bias)} = \frac{\sum_{t=1}^{T}(x_m^t - x_o^t)}{\sum_{t=1}^{T} x_o^t} \times 100\% \tag{56}$$

where x_m^t is the model output at time step t; x_o^t is the corresponding observation at time step t; T is the total length of the simulation time. The Pearson's correlation coefficient is also used to measure the degree of collinearity between simulated and measured data and is calculated as follows:

$$\mathbf{R} = \frac{\sum_{t=1}^{T}(x_m^t - \overline{x_m})(x_o^t - \overline{x_o})}{\sqrt{\sum_{t=1}^{T}(x_m^t - \overline{x_m})^2}\sqrt{\sum_{t=1}^{T}(x_o^t - \overline{x_o})^2}} \quad (57)$$

where $\overline{x_m}$ and $\overline{x_o}$ are the means of model outputs and observations, respectively.

3. Hydrological and Geochemical Processes in SSHCZO

3.1 Hydrological processes in 2009

We focused on elucidating the complex hydrogeochemical interactions in 2009 because the hydrological processes in SSHCZO, including evapotranspiration (ET), infiltration and recharge, subsurface water storage and lateral flow, stream water discharge and overland flow, were already simulated for 2009 using a set of hydrological parameters calibrated to reproduce the hydrological observations (groundwater table depth, stream discharge, soil moisture) (Shi et al., 2014) and high frequency meteorological forcing data and water chemistry observations were available .

Overall, the hydrological processes in SSHCZO have a significant influence on the temporal evolution and spatial distribution of chemical species. For simplification, we calculate the watershed-averaged hydrological fluxes and water storage to demonstrate the hydrological cycle in Shale Hills. Daily precipitation was based on hourly precipitation data (http://criticalzone.org/shale-hills/data/dataset/2556/) (Duffy, 2013). Daily discharge, total ET, water storage in the unsaturated and in the saturated zones were calculated from the daily modeling output and were averaged by the area of each distributed element for the whole watershed to obtain watershed-averaged values.

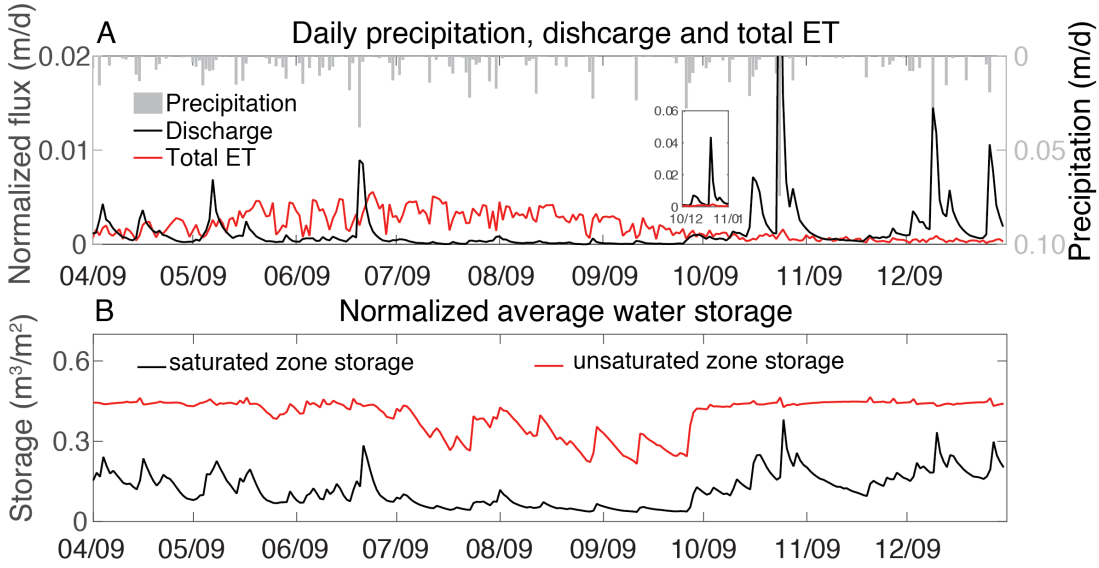

Figure 3-4 A: Temporal evolution of measured daily precipitation [m/d], simulated discharge normalized by watershed area [m/d] and simulated total ET [m/d]. B: Temporal evolution of simulated net watershed water storage in the saturated and unsaturated zones [m^3/m^2](Shi et al., 2013a). Here daily water storages, a measure of water content, indicate similar total precipitation across different seasons however higher ET in the summer, leading to wetter watershed (higher water storage) in spring and winter and dry watershed (lower water storage) in the summer.

From April 1st to Dec. 31st 2009, the total precipitation was 0.9 meter. The model shows that 39.7% of precipitation contributes to stream discharge, 58.8% to total ET and 1.5% remains in the watershed. SSHCZO is a hydrologically responsive watershed with stream discharge closely following intensive precipitation events (Figure 3-4A). In general, large rainfall events lead to more discharge and less ET. Total ET increased from spring to summer and then decreased in winter. Although the precipitation is relatively invariable over the year, water storage decreases due to the higher ET during the summer, which is consistent with the observed water level drop at the monitoring wells (Shi et al., 2013b). Starting from late September, ET decreased, leading to water storage increase. A large rainfall event occurred on Oct. 24th resulting in the highest discharge in 2009. From Apr. 1st to Dec. 31st, 2009, the saturated zone water storage averaged 0.16 m^3/m^2 and unsaturated zone water storage averaged 0.40 m^3/m^2.

The ephemeral stream in SSHCZO demonstrated extremely low discharge between June and September. The groundwater flow from deeper subsurface was not explicitly modelled in Flux-PIHM and was added as an influx source for Cl and Mg. The influx rate was tuned to 1.041E-4 $m^3/m^2/d$ to reproduce concentrations of both Cl and Mg in the stream, as will be discussed later. This is 6.7% of the calculated 0.015 $m^3/m^2/d$ of average stream discharge in 2009 and is consistent with the observation that groundwater influx to the stream is about 5% (Sullivan et al., 2016b).

3.2 Transport of the non-reactive tracer chloride

Chloride is a major anion in rainwater and is largely non-reactive. It is insignificant in concentration in the bedrock and regolith and is therefore controlled by atmospheric or groundwater inputs, watershed hydrodynamics and transport. The average chloride concentration in rainwater in 2009 was 3.05 (±4.20) μmol/L, as measured at Leading Ridge as part of the National Atmospheric Deposition Program about 7.11 miles from SSHCZO (Lamb and Bowersox, 2000). The data from Clean Air Status and Trends Network (CASTNET) (http://epa.gov/castnet/javaweb/index.html) for this region suggests Cl input from dry deposition accounts for less than 3% of total Cl input. However, instead of rainwater concentration, throughfall water concentration is needed to calculate the mass input into soil from atmospheric deposition. During precipitation the tree canopy intercepts a fraction of rainwater, which becomes concentrated as salt residue later during evaporation. The salt residue eventually comes to the ground with litter fall and dissolves into through fall. Therefore the through fall is expected to have a higher Cl concentration compared to the rainwater due to both concentration and inclusion of other sources (Svensson et al., 2012). To calculate an estimated through fall concentration, we multiplied the Cl concentration in rainwater by a tuning multiplier that is maintained constant for all simulations. This multiplier, 1.6, indicates the infiltration water has 0.6 times higher Cl and

Mg concentration than rainwater. This multiplier was used for all solute data originated in precipitation and thus does not affect temporal trends or the spatial distribution. The tuning allows the model to reproduce the Cl concentrations in stream water. Consistent with higher through fall [Cl], the volume of through fall is smaller than incoming rainwater because the vegetation intercepts some water. This through fall volume is calculated in Flux-PIHM. In fact, the multiplier is almost exactly the ratio between the total precipitation / total through fall, indicating Cl mass balance in the watershed.

Cl concentration in rainwater is 3.05 (±4.20) μmol/L on average (Lamb and Bowersox, 2000), leading to a total mass input of 538.5 moles/year in 2009. The Cl deposition from dust is about 5.5 moles/year in 2009 (http://epa.gov/castnet/javaweb/index.html). The overall Cl contribution (544 moles/year) from atmospheric deposition plus the groundwater influx of 280 moles/year approximately equals to the annual Cl outflow of about 846 mol/year for 2007 through 2011 (Brantley, 2013a; Brantley, 2013e, c; Brantley, 2013g) calculated by multiplying discharge with concentration at the stream mouth. The mass influx from deeper groundwater is modeled as the product of the groundwater Cl concentration (63.62±24.82 μmol/L) (Brantley et al., 2013c) and a ground water influx rate into the stream channel elements near the stream mouth. This groundwater influx rate is maintained constant (Sullivan et al., 2016b). The value of the influx rate was tuned to reproduce concentrations of both Cl and Mg in the stream. The throughfall concentration multiplier and the influx of chloride from deeper groundwater into the shallower stream channel are the only tuning parameters used for reproducing the Cl data.

3.3 Reactive Transport of Magnesium

The shallow soil and regolith contains quartz, illite, “chlorite” and kaolinite (Jin et al., 2010; Jin et al., 2011c). We use the term “chlorite” to indicate a mineral showing the same peak as chlorite in X-ray diffraction (XRD); however, it could contain chlorite, vermiculite, hydroxy-interlayered vermiculite (HIV), and/or mixtures of these phases (Jin et al., 2010; Moore and

Reynolds, 1989). Magnesium comes from three sources: clay dissolution (Jin et al., 2010), atmospheric deposition, and groundwater influx (Jin et al., 2014). Chlorite and illite in the shallow regolith dissolve and act as the major source of Mg to water flowing along hillslopes. The clay dissolution rates are calculated based on the Transition State Theory (TST) (Helgeson et al., 1984; Lasaga, 1984):

$$R_k = k_k A_k{}^0 S_w^n (1 - \frac{IAP}{K_{eq}}) \quad (58)$$

Here R_k is the rate of mineral k (mol/(m^3 s)), A_k^0 is the surface area of mineral k per volume of porous media [m^2/m^3] under fully water saturated conditions; S_w is the water saturation; k_k is the intrinsic rate constant [mol /(m^2 s)]; IAP is the ion activity product for the reaction and K_{eq} is the equilibrium constant. The mineral surface area in the unsaturated zone is strongly affected by soil moisture (Clow and Mast, 2010). Under unsaturated conditions, water tends to wet the surface everywhere, but the water films do not flow and the surface area therefore do not experience net reaction. Here we use an n value of 2/3 as the exponent on grain size to indicate the surface area to volume ratio of dissolving mineral grains (Mayer et al., 2002). As such, the dissolution rates not only depend on the intrinsic mineral reactivity (i.e., the rate constant) but also on how much surface area is exposed to water in the zone of phreatic water which is connected to the stream (i.e. flowing water).

Mg concentration in rainwater is 1.40 (±1.17) μmol/L on average (Lamb and Bowersox, 2000), leading to a total mass input of ~120 moles/year in 2009. The Mg deposition from dust is about 5 moles/year in 2009 (http://epa.gov/castnet/javaweb/index.html). The overall Mg contribution (~125 moles/year) from atmospheric deposition is relatively small compared to the annual Mg outflow of about 4700 moles/year (Brantley et al., 2013a)calculated by multiplying

discharge with concentration at the stream mouth. Groundwater influx also contributes Mg to the stream water (Jin et al., 2014). It has been hypothesized that most of the carbonate is depleted in the upper layers of the watershed (Brantley et al., 2013) and that it is the dissolution of magnesium-containing carbonate into the regional groundwater at ~ 22 meters depth under the northern ridge and at 2 meters depth under the stream outlet that produces groundwater that is relatively rich in Mg (238.83 ±109.78) μmol/L (Jin et al., 2011b). Importantly, some of this carbonate appears to be secondary in the valley. Jin et al. (2014) estimated the annual contribution from deep groundwater is in the range of ~1500 mol Mg/year by comparing the Mg concentrations in stream water and soil water. Sullivan et al. (2016) further estimated that about 22% of the Mg is from deep groundwater flow in Shale Hills (Sullivan et al., 2016b). Therefore, although not explicitly modeled in Flux-PIHM, we added Mg groundwater influx as a Mg source to the stream water with constant groundwater influx rate across the year. The constant influx rate is a tuned parameter during our simulation.

Magnesium also adsorbs on mineral surfaces through cation exchange reactions on the soil surface. While magnesium ultimately derives from mineral dissolution, cation exchange is believed to play an important role in buffering its concentration in pore water and stream water (Clow and Mast, 2010; Godsey et al., 2009; Herndon et al., 2015a; Jin et al., 2011b). Magnesium also participates in aqueous complexation and secondary mineral precipitation (Brantley et al., 2013a; Jin et al., 2010). A list of key reactions is in Table 1. Uptake of chemical species into vegetation can play an important role in clay weathering and element cycling. Net Mg uptake by plants as a result of vegetation cycling has been found to vary between -16 and ~ 25 moles/hectare/year in 38 investigated forests in United States, Europe, Japan and USSR (Cole and Rapp, 1981; Johnson et al., 1985). In SSHCZO, net uptake of Mg is about 22 moles/hectare/year (Herndon et al., 2015c). These values are relatively small compared to the annual Mg outflux of about 500 mol/hectare/year from SSHCZO. We therefore assume negligible influence of

vegetation cycling on Mg reactive transport. The Mg concentration in the model therefore reflects the interplay between hydrological processes, solute transport, and geochemical reactions.

Table 3-1 Key reactions in the model and their kinetic and thermodynamics parameters

Clay dissolution relevant to Mg^{2+} (Jin et al., 2010)	$\log_{10}K_{eq}$	$\log_{10}k$ (mol/m^2/s)	Specific surface area (SSA, m^2/g)
$(Fe_{0.24}Mg_{0.38}Al_{0.38})_6(Si_{0.07}Al_{0.93})_4O_{10}(OH)_{8\,(s)}$ *(chlorite)*+ 5.72 $H_4SiO_{4\,(aq)}$ + 4.56 H^+ ↔ 1.44 $FeOOH_{(s)}$ + 2.28 Mg^{2+} + $3Al_2Si_2O_5(OH)_{4\,(s)}$ + 11 H_2O	38.8	-12.5[a]	0.01 (1.1~7.7)[a]
$K_{0.77}(Si_{0.30}Al_{0.70})(Fe_{0.48}Mg_{0.07}Al_{0.45})AlSi_3O_{10}(OH)_{2\,(s)}$ *(illite)*+ 0.91 H^+ + 3.235 H_2O ↔ 0.77 K^+ + 0.48 $FeOOH_{(s)}$ + 0.07 Mg^{2+} + 1.075 $Al_2Si_2O_5(OH)_{4\,(s)}$ + 1.15 $H_4SiO_{4\,(aq)}$	1.45	-14.1[b]	0.86 (40.6~215)[b]
Carbonate dissolution and secondary precipitation			
$CaMg(CO_3)_{2\,(s)}$ *(dolomite)*↔Ca^{2+} + Mg^{2+} + CO_3^{2-}	-17.8[c]	-5.92[d]	
$CaCO_{3\,(s)}$ *(calcite)* ↔Ca^{2+} + CO_3^{2-}	-7.3	-6.65[e]	
$MgCO_{3\,(s)}$ *(magnesite)* ↔Mg^{2+} + CO_3^{2-}	-7.52[e]	-8.22[e]	
Cation exchange reaction[f]			
>XNa + H^+↔ >HX + Na^+	2.40[f]		
$>X_2Ca$ + 2Na^+↔ >2NaX + Ca^{2+}	0.50[f]		
$>X_2Mg$ + 2Na^+↔ >2NaX + Mg^{2+}	0.50[f]		

[a]: (Brandt et al., 2003) [b]: (Aylmore et al., 1970; Köhler et al., 2005; Köhler et al., 2003) [c]: (Sherman and Barak, 2000) [d]: (Gautelier et al., 1999) [e]: (Pokrovsky et al., 2005) [f]: derived from (Jin et al., 2010) using Vanselow convention, all others from (Wolery, 1992)

The non-reactive transport of Cl and reactive transport of Mg in SSHCZO was simulated from Dec. 1st, 2008 to Jan. 1st, 2010. Based on pore water chemistry, mineral composition and cation exchange capacity (CEC) measurements (Brantley et al., 2013c; Jin et al., 2010), different initial chemical conditions were assigned to pore waters in different parts of the watershed based on their locations within the watershed (RT, MS, VF), as shown in Table 2. The concentration of total bicarbonate was calculated based on measured alkalinity ranging from 0.05 to 0.73 meq/L (Brantley et al., 2013b). The hydrological and land surface parameters that reproduced the hydrological data were used to drive Flux-PIHM (Shi et al., 2013b). We used a fixed diffusion coefficient of 1.0×10^{-9} m^2/s and a fixed dispersivity of 0.1 m within the reported range at the relevant spatial scale (Cussler, 2009; Gelhar et al., 1992).

Table 3-2 Initial pore water chemistry and mineral compositions used in simulations

Chemical Species	Ridge Top	Mid-Slope	Valley Floor	Ways Obtained
Aqueous species (mol/L except for pH)[a]				
pH	4.56	4.48	4.70	Measured
Magnesium	2.49×10^{-5}	5.41×10^{-5}	5.61×10^{-5}	Measured
Calcium	5.22×10^{-5}	4.97×10^{-5}	8.49×10^{-5}	Measured
Iron	5.80×10^{-7}	2.76×10^{-7}	4.32×10^{-7}	Measured
Chloride	3.69×10^{-5}	3.12×10^{-5}	3.93×10^{-5}	Measured
Silicon	8.72×10^{-5}	9.97×10^{-5}	1.13×10^{-4}	Measured
Potassium	2.19×10^{-5}	1.52×10^{-5}	2.33×10^{-5}	Measured
Sodium	1.90×10^{-5}	1.85×10^{-5}	2.67×10^{-5}	Measured
HCO_3^-	0.28	0.28	0.28	Calculated from alkalinity[b]
Mineral volume fraction (m^3/m^3)[c]				
Illite	0.2304	0.2179	0.3295	Measured
chlorite	0.0559	0.0542	0.0541	Measured
Kaolinite	0.0215	0.0229	0.0121	Measured
Quartz	0.4973	0.5069	0.3941	Measured
Calcite	0.0049	0.0081	0.0203	Measured
FeOOH	0	0	0	Measured
Cation Exchange Capacity (CEC) [eq/g]	3.9 $(\pm0.5)\times10^{-5}$	4.0 $(\pm0.5)\times10^{-5}$	6.4 $(\pm0.7)\times10^{-5}$	Measured[d]
	5.0×10^{-5}	4.0×10^{-5}	6.0×10^{-5}	Tuned

[a]: pore water chemistry data from (Brantley et al., 2013c) [b]: alkalinity was measured in stream water in SSHCZO. We assumed as an initial guess that the pore water has similar alkalinity as stream water. However, the alkalinity of pore water changes in the simulation as a result of CO_2 dissolution. [c]: mineral composition data from (Jin et al., 2010) [d]: CEC values as measured previously (Jin et al., 2010).

Simulations of Mg reactive transport require parameterization of key chemical reactions based on a geochemical database and *a priori* values reported in the literature. Equilibrium constants for aqueous complexation and mineral reactions were derived from the database EQ3/6 (Wolery, 1992). The kinetic rate constants for mineral dissolution from literature were used (Table 1). The calibration of RT-Flux-PIHM was carried out using a "trial and error" strategy until model output reproduced the observations. Mineral specific surface areas (SSA) were

adjusted starting from measured literature values. For Mg ion exchange, the equilibrium constant of $10^{0.5}$ was derived from measurements for SSHCZO soils assuming the pore water and soil surface are at equilibrium (Jin et al., 2010). Measured cation exchange capacity values (CEC, [eq/g]) (Jin et al., 2010) were used first and then tuned to reproduce Mg pore water concentration data. The soil CEC that reproduced data is $2.5\sim10.0\times10^{-5}$ eq/g (Table 2). This is close to the mole-fraction-wieghted CEC value estimated using mole fractions of chlorite and illite in SSHCZO soils and measured chloride and illite CEC values of $0\sim10\times10^{-5}$ eq/g and $10\sim40\times10^{-5}$ eq/g from literature, respectively (Weaver, 1989).

As described previously, the groundwater influx of Mg was added as an additional mass input near the outlet of the stream. The groundwater influx was assumed constant at a rate of 1.04×10^{-4} m^3/d compared to 0.015 m^3/d of average discharge to reproduce the measured magnesium concentrations in stream water. Constant Mg groundwater influx was estimated to be 1000 moles/year. In summary, we tuned the clay surface area, CEC, and groundwater influx to reproduce the measured stream water and pore water concentrations.

4. Results

4.1 Chloride

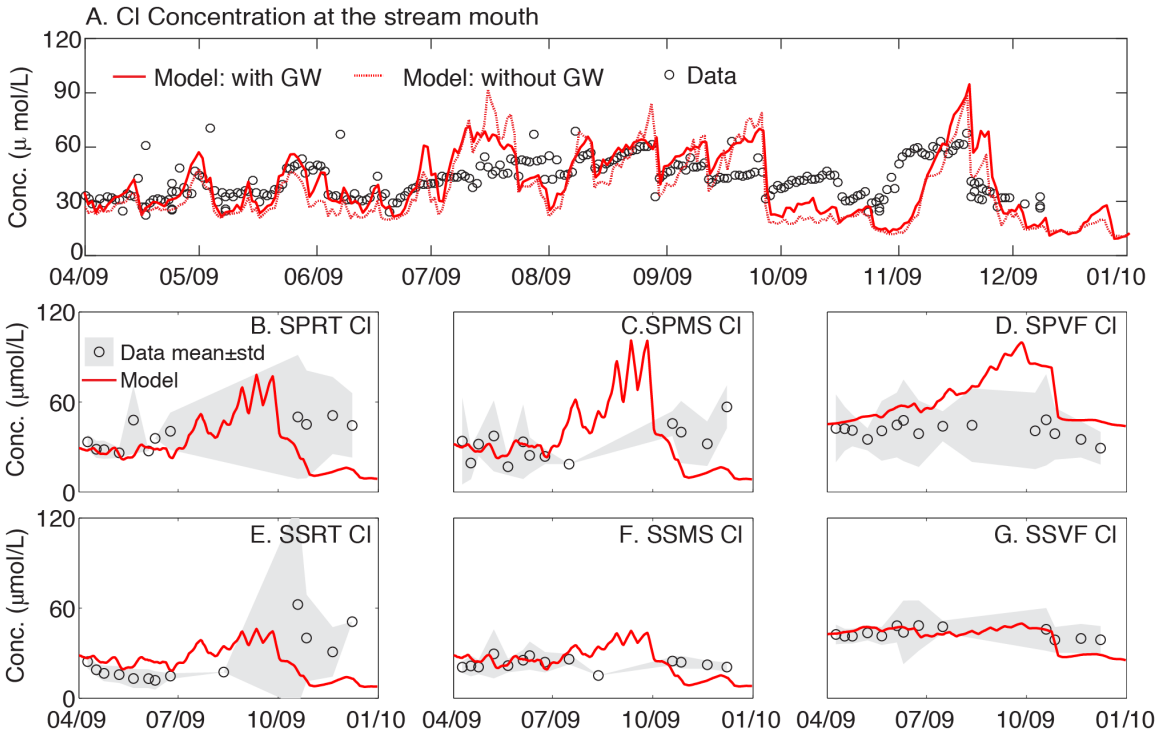

Figure 3-5 Temporal evolution of average chloride data (open circles) and modeling output (red lines) from Apr. 1st to Dec. 31st, 2009. A: concentrations at the stream mouth; B through G: concentrations in 6 lysimeter sites, including the 3 South Planar sites (SPRT, SPMS, SPVF) and 3 South Swale sites (SSRT, SSMS, SSVF) (Figure 3-2). Grey areas indicate ±one standard deviation for the measured pore water chemistry.

RT-Flux-PIHM captured the trend and magnitude of Cl evolution at the stream mouth (Figure 3-5A). The total bias between the data and prediction is -3.40% and the Pearson's correlation coefficient is 0.54, well within ±25.00%, a value considered very good for solute transport models (Moriasi et al., 2007). Chloride concentrations in stream water gradually increased from spring to summer when the watershed became drier, and gradually decreased until

November when the watershed became wetter. A concentration peak occurred in November following a big rainfall event on October 24th, 2009.

Table 3-3. The total bias* (%) between model output and measured concentrations.

Element	Stream	SPRT	SPMS	SPVF	SSRT	SSMS	SSVF
Chloride	-3.40	-41.66	-18.72	40.67	-19.31	-5.07	-5.11
Magnesium	-13.22	13.77	-9.23	8.41	108.13	16.20	-21.40

*A negative value means the model prediction is lower than the data.

The model also reproduces the general trends of chloride concentrations in the pore water (Figure 3-5B~G and Table 3-3). The model prediction is closest to data in the spring. The elevated evaporation in the summer results in less pore water and therefore high chloride concentrations. This is more pronounced in pore waters sampled in lysimeters in the south planar slope than in the south swale slope. This is expected because the swales collect water from convergent flow -- they almost always have more water than planar slopes – and therefore flush Cl into the stream (Qu and Duffy, 2007a). The model predicts a peak in Cl concentration during summer in all locations except SSVF. The model underestimates chloride at all locations between October and December. This is likely due to the fact that Flux-PIHM misidentified the Oct 15th snowstorm as a rainfall event based on the above freezing temperature. In reality, it takes longer for snow to melt and flow into the stream than rainfall (Shi et al., 2013b).

Hydrological Controls on Chloride Transport. To understand hydrological controls on chloride transport, the predicted spatial profiles of water saturation in the unsaturated zone, water storage in saturated zone (h_g), depth from surface to water table and chloride concentration are compared (Figure 3-6). The spatial patterns of soil water storage in different seasons have been validated by field observations (Shi et al., 2015). The water storage is higher in the spring and winter and is lower in the summer. The valley floor and swales are areas of gravity-driven convergent flow (Figure 3-6A, B). The water table (also the divide between the saturated and

unsaturated zone) is shallower along the stream channel and deeper in all other locations (Figure 3-6C). From spring to summer, the depth to water table (DWT) increases as the watershed gradually loses water due to higher ET. In the wet spring and winter, chloride concentration is relatively low in the entire watershed, largely because the wet watershed is more connected to the stream, allowing easy flushing of Cl out of the watershed. In the dry summer, discharge is very low at least partly because only a small proportion of the watershed is connected to the stream (Figure 3-6B). As a result, Cl is trapped in pockets or "immobile porewaters" that are not "connected" to the convergent flow in the valley floor and stream, leading to highly elevated concentrations as ET continues (Figure 3-6D). In effect, connectivity to the stream acts like a valve in the catchment that either retains chloride in porewaters along the planar slopes or flushes the chloride out. This leads to patterns of Cl spatial distributions that are almost opposite to that of water storage in the summer. On October 15th, a snowstorm hit Shale Hills followed by a heavy rain on the 24th. The big precipitation events flushed the trapped chloride out of the watershed, leading to the peak in stream water chloride concentration in November (Figure 3-5A). This peak appears in both measured and simulated data. The time lag between storm and peak in discharge is very short in the simulation compared to the data. This discrepancy is attributed to the nature of the precipitation (snow versus rain) as described above.

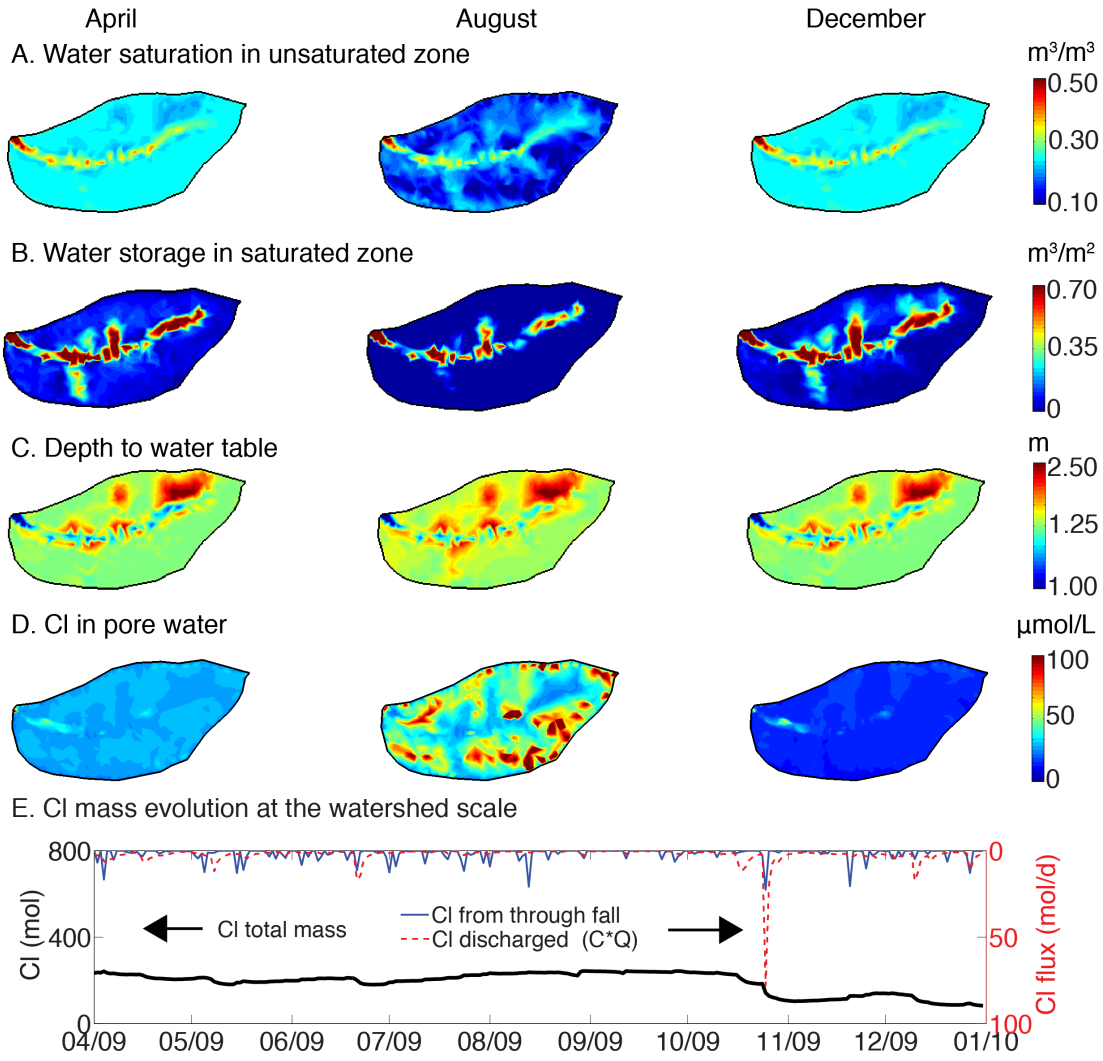

Figure 3-6 Spatial profiles in April, August, and December in 2009. A: water saturation (soil moisture) in the unsaturated zone [m^3/m^3]; B: water storage h_g in the saturated zone [m^3/m^2]; C: depth from ground surface to water table (DWT) [m]; D: local Cl concentration in pore water [µmol/L] (calculated as a volume weighted average over the saturated and unsaturated zones); Chloride concentrations are lower in or near the valley floor and swales where water is more abundant and connected to the stream. E: Chloride total mass (pore water volume × Cl concentration) over the entire watershed, daily chloride influx from the throughfall and outflux (discharged, C×Q) [mol/d].

The dynamics of the total mass of Cl in the watershed is shown in Figure 6E. Total chloride mass in the watershed was calculated by summing up Cl mass (pore volume × concentration) in each prismatic element at the end of each day. Input of Cl is the product of throughfall and throughfall Cl concentration, and the output is the discharged Cl fluxes calculated

from the product of daily average Cl concentration at the stream mouth and the stream discharge (C×Q). It is interesting to note that although Cl concentrations in the stream (Figure 5A) vary only from 25 – 70 μmol/L, the product C×Q (the flux) varies by orders of magnitude due to the orders of magnitude variation in discharge. In the dry summer, the low discharge leads to low connectivity, low flushing of planar hillslopes, and low Cl export out of the watershed, i.e., Cl accumulates in the watershed. The increase or decrease of Cl mass in the watershed is largely determined by the balance (or lags) between the rainfall input and discharge output. In late October, one intense rainfall / snowfall event connected the immobile zones to the stream and flushed the accumulated Cl especially along planar hillslopes, leading to the drop in total catchment Cl mass by approximately 50%.

CQ usually follows power law forms and linear log-log relationships, as shown in Figure 7 for data and model prediction. The model reproduced data well with both data and model exhibiting chemostatic behavior. The model predictions at higher discharges are lower, however, than the measured data, indicating underestimation of chloride concentration between October and December (discussed above). The power law CQ slopes for chloride are -0.0300 (±0.0062) and -0.1011 (±0.0060) for data and model prediction, respectively. This Cl chemostatic behavior is largely dictated by the hydrodynamics of the watershed. In the summer when stream discharge is low and planar slopes are largely unconnected to the stream, most chloride is trapped in "immobile water" in the planar hillslopes. During these dry intervals, the discharged Cl derives mostly from the more stream-connected swales and the valley floor where flow paths converge. In spring and winter when stream discharge is high, large precipitation events and lower ET leads to a wetter watershed that connects not only the swales and valley floor area but also planar hillslopes to the stream, mobilizing trapped Cl during the summer. This mobilization of the trapped Cl however also mitigates the dilution of chloride by more water, leading to relatively

constant at the stream mouth. Stream connectivity acts as a valve on the planar hillslopes such that chloride concentrations remain constant in the stream over time.

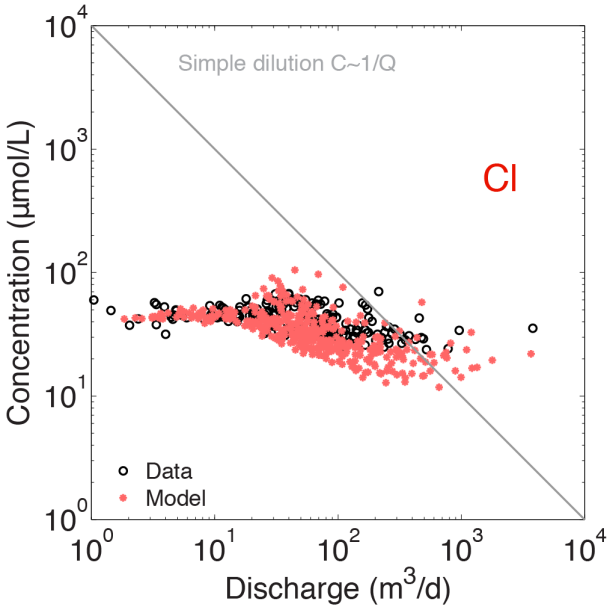

Figure 3-7 CQ relationships for measured and predicted chloride in 2009. The grey diagonal line indicates a CQ relationship if simple dilution dominates the system.

4.2 Magnesium

RT-Flux-PIHM reproduces Mg in the stream water to within 15% when all processes are included (rainwater input + clay dissolution + Mg ion exchange + groundwater influx) (Figure 8A). The simulation results are slightly closer to data than that of Cl with a lower total bias of -13.22% and the Pearson's correlation coefficient of 0.52. Of all parameters, the Mg concentration predicted in the model depends most strongly on the clay surface area. The values of 0.01 m^2/g and 0.86 m^2/g for chlorite and illite used in the model are about two orders of magnitude lower than the laboratory-measured surface areas for chlorite (1.1 to 7.7 m^2/g) (Brandt et al., 2003) and illite (40.6~215 m^2/g) (Aylmore et al., 1970). The product of kinetic rate constant and the specific

surface area for chlorite calculated from this work (6.5×10^{-10} mol/m^3/s) is very close to the estimated value for Shale Hills based on field data (7.6×10^{-10} mol/m^3/s) (Jin et al., 2011b).

The fact that we need to assume a lower specific surface area than measured in the laboratory reflects the long-standing laboratory-field rate discrepancy observed for more than 3 decades (Navarre-Sitchler and Brantley, 2007b). In effect, we are making the reasonable argument that the effective surface area that interacts with water that flushes to the stream in the catchment is lower than the surface area of clay powders measured in the laboratory by the Brunauer–Emmett–Teller (BET) method (Li et al., 2014; Moore et al., 2012; Salehikhoo and Li, 2015). In Shale Hills, water is quickly transmitted in the subsurface when the catchment is wet (December-May) but transmitted much slower in summer when the catchment is dry. Therefore, from a microscopic point of view, much of the pore water directly contacting clay surfaces – especially along planar hillslopes -- might be chemically equilibrated in the thin water film at the clay surface even though the average pore fluid concentration calculated at a larger scale is not equilibrated with regard to minerals. In addition, Fe-OOH or organic matter could be coating the reacting mineral surface as well. In essence, the specific surface area used here reflects the "effective" surface area (Salehikhoo et al., 2013) at the watershed scale, i.e., the surface area that is actually dissolving but may be a result of multiple physical and chemical processes that lower dissolution rates.

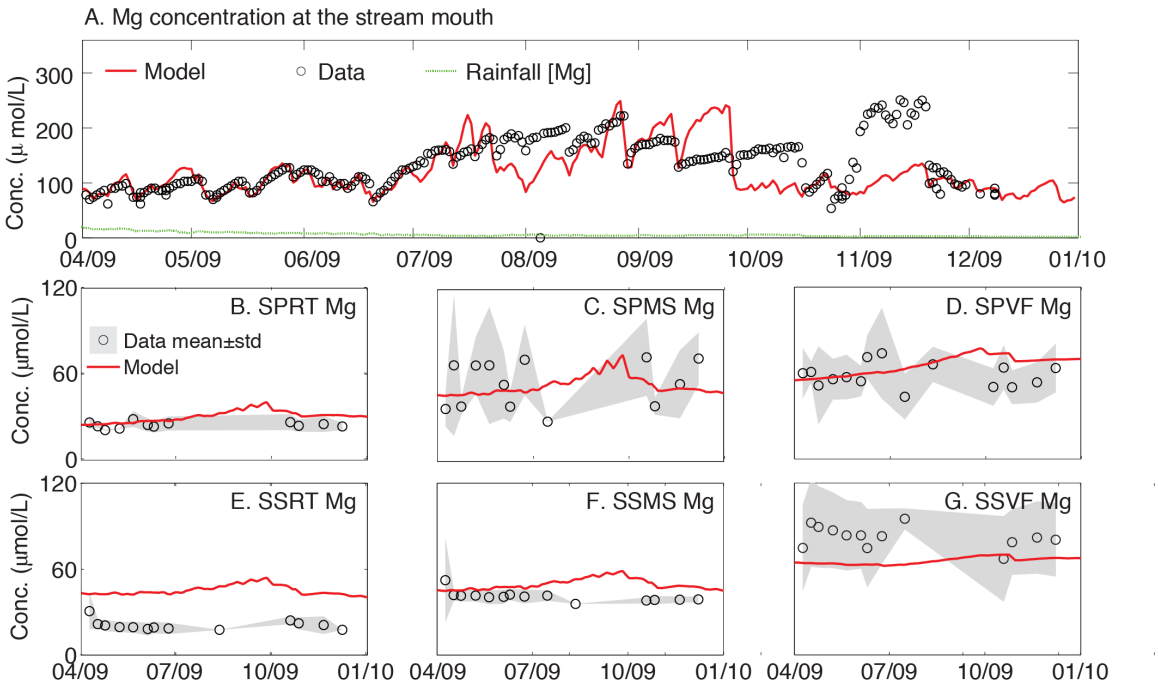

Figure 3-8 A. Temporal evolution of modeled and measured magnesium concentrations in stream water (A). (B-G) Temporal evolution of modeled and measured pore water Mg concentration in different sampling locations, including the 3 South Planar sites (SPRT, SPMS, SPVF) and 3 South Swale sites (SSRT, SSMS, SSVF).

Overall, the annual flux of Mg entering the catchment in rainwater (65.7 moles/year) was a negligible 1.4% of the total outflowing Mg (4694.8 moles/year). Clay dissolution accounted for 77.7% (3647.9 moles/year) of this outflux, while the groundwater influx (1000.0 moles/year) contributed 21.3%. Groundwater influx had a larger impact on the stream water concentration from July to September, consistent with previous observations (Jin et al., 2014; Thomas et al., 2013). No carbonate precipitation was observed in the simulation.

The predicted Mg concentrations in pore water are close to measured mean concentrations with total bias values lower than 25% except in SSRT (Figure 8 and Table 3). At SSRT the model overestimates by 108% for the whole period of simulation. The predicted Mg concentrations increase from Ridge Top (RT) to Mid Slope (MS) and to Valley Floor (VF),

consistent with observations. This increase is attributed to clay dissolution along the flow path from RT to VF (see also Jin et al., 2011).

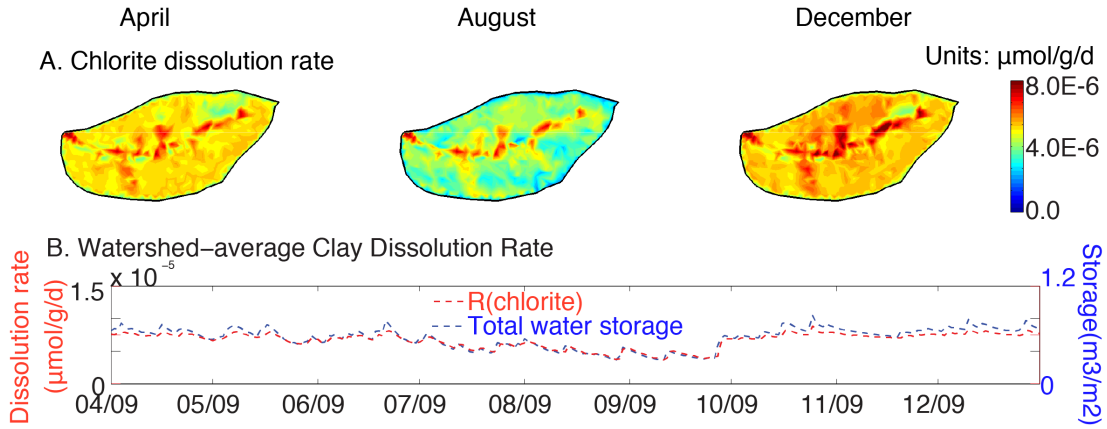

Figure 3-9 A: Predicted spatial distribution of chlorite dissolution rate [µmol/g/d] on Apr. 1st, Aug. 1st and Dec. 1st, 2009; B: Temporal evolution of the watershed-average dissolution rate of and chlorite [μ mol/g/d] and watershed-average total water storage in saturated and unsaturated zones [m^3/m^2]. Watershed-averaged dissolution rates were calculated from the change per day in the mineral mass (µmol) in the entire SSHCZO (normalized by the total mass (g) of each mineral in SSHCZO).

Clay dissolution. The majority of magnesium comes from clay dissolution, especially chlorite dissolution. Water storage influences clay dissolution by controlling the wetted surface area of clays in the shallow saturated zone, as indicated by Equation (3). Chlorite dissolves faster in swales and valley floor where water is generally more abundant and more connected to the stream (Figure 3-9A). Watershed-average dissolution rates decrease by about half in the summer as a result of drier conditions (Figure 3-9B). The chloride dissolution rate is about 1.70×10^{-10} $mol/m^3/s$ on average in 2009, which is very close to the estimated long-term chlorite dissolution rate of 1.90×10^{-10} $mol/m^3/s$ calculated from soil profiles at the ridge top (Jin et al., 2010). Although not shown here, the dissolution rates of illite vary in the same spatial and temporal pattern as that of water storage: high dissolution rate when water storage is high. The coupling of mineral dissolution and water content is demonstrated through Figure 10. Essentially, when the watershed becomes wetter with high discharge and total water storage, the dissolution rates increase because the wetted surface area increases. The increase in wetted surface area and

dissolution is proportional to the water content, therefore mitigating the dilution effect brought by higher water volume in the wetter watershed. This counterbalance introduced by larger dissolution rates maintains a relatively constant Mg concentration across the watershed.

Figure 3-10 also shows a clear division in [Mg] concentration below and above the discharge of about 20 m^3/d, suggesting different controls of Mg concentration under dry and wet conditions. Under the dry condition below this number, average Mg concentration is high. In fact, the [Mg] shows chemostatic behavior. Under the wet condition above this number, [Mg] is chemostatic. This largely due to the fact that under dry conditions, dissolved Mg is trapped in immobilized zones without being able to flush out. This is similar to the Cl dynamics in low discharge conditions.

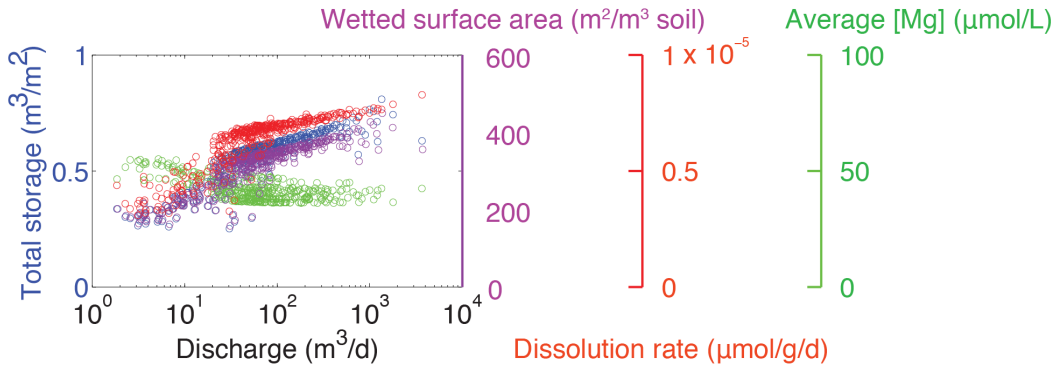

Figure 3-10 Total water storage, wetted surface area, dissolution rates, and average [Mg] at the watershed scale as a function of discharge. The dissolution rates rise proportionally with the discharge, water storage, and wetted surface area, leading to larger dissolved Mg mass. This increase in dissolved Mg flux however is counterbalanced by larger total water storage, leading to relatively constant average [Mg] at the watershed scale.

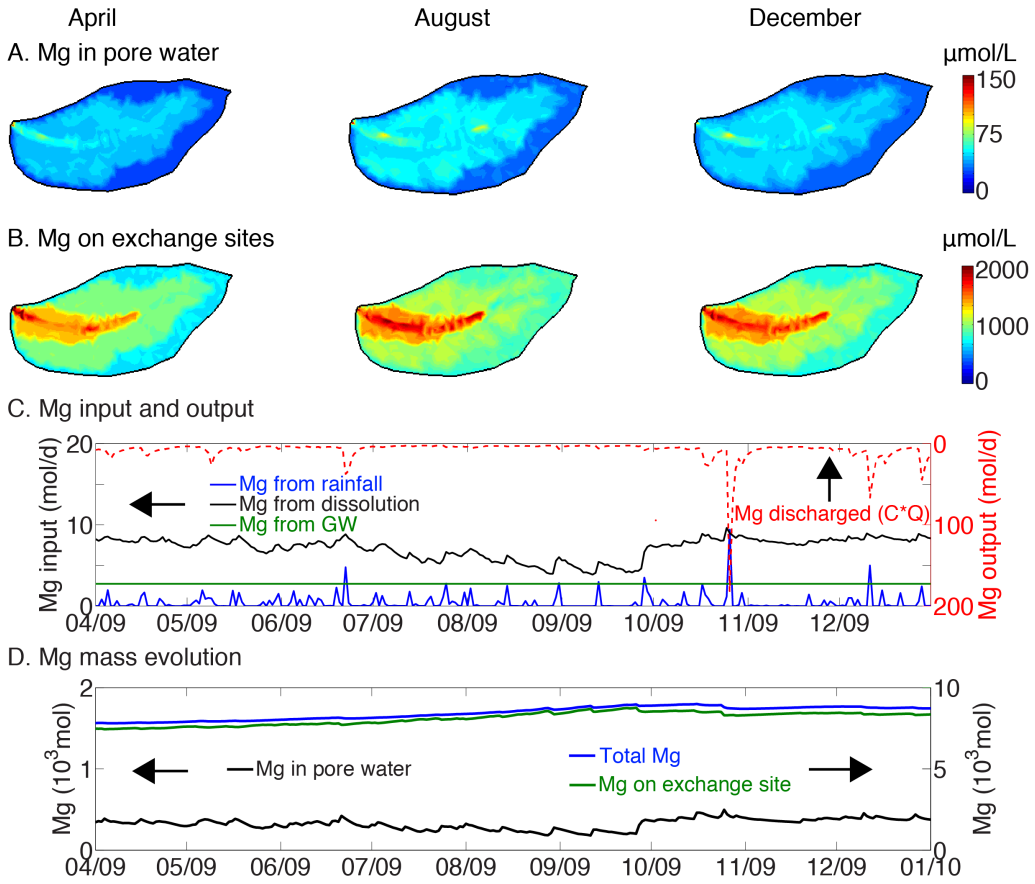

Figure 3-11 A: spatial profiles of [Mg] in pore water [μmol/L]; B: [Mg] on exchange sites μmol/g]; C: Daily input (bottom solid lines) from rain water (blue), clay dissolution (black), groundwater (green), and output fluxes from stream discharge (red, C×Q, mol/d). Mg primarily comes from dissolution and GW influx, while discharge flushes out Mg, especially in big rainfall events. D: Mg mass evolution: Mg mass in pore water (solid black line) and on exchange sites (solid green line) calculated by summing up Mg mass over the entire watershed. Total Mg is the sum of Mg in pore water and on exchange site. The exchange sites store an order of magnitude more Mg mass than pore water.

Role of Mg exchange. It has been speculated that cation exchange on solid surfaces acts as a buffer in SSHCZO and elsewhere to regulate magnesium concentrations in pore water and to set the lower limit of concentrations observed in stream water (Clow and Mast, 2010; Herndon et al., 2015a; Jin et al., 2011b). Figure 11A-B shows the predicted spatial distribution of pore water and exchange site concentrations on Apr. 1st, Aug. 1st and Dec. 1st, 2009. Mg aqueous concentrations are relatively constant over time. In wet spring and winter seasons, Mg concentrations are only slightly lower than those in the dry summer months. The concentration of Mg on exchange sites

(Mg per unit volume of regolith on exchange sites) is calculated to be highest in the valley floor (Figure 10B). This is attributed to the fact that convergent flow of water consistently brings Mg mass fluxes from upslope. This is consistent with the observations that Mg concentrations on exchange sites in south planar valley floor (SPVF) are higher than in south planar ridge top (SPRT) and south planar middle slope (SPMS) (Jin et al., 2010). Predicted [Mg] on exchange sites agree relatively well with the measured data – although the model underestimated Mg concentration on exchange sites in the valley floor.

Concentrations of Mg in porewaters do not increase as much as Cl during the summer, primarily because cation exchange reactions buffer Mg concentration in water. In other words, as Mg concentrations increase during the summer, they charge up the exchange sites especially in the valley floor, buffering the increase in aqueous concentration. Figure 11C and D shows the Mg mass balance at the watershed scale. In the summer, clay dissolution is slower due to lower water content, lower wetted surface area, and even lower Mg discharge out of the watershed. As a result, the total Mg cation mass (in the form of free cation in pore water or those associated with CEC) over the entire watershed actually increases. This is similar to Cl. However, for Mg, exchange sites store more than an order of magnitude higher magnesium mass than pore water (when considered over the entire catchment) and therefore act as a significant storage buffer that reduces the spatial and temporal evolution of Mg concentration. In late October, the large rainfall and snowfall events flush out 2.1% of the total Mg of the whole watershed. In contrast to Cl, the Mg mass remains mostly on the exchange sites even after the large precipitation events.

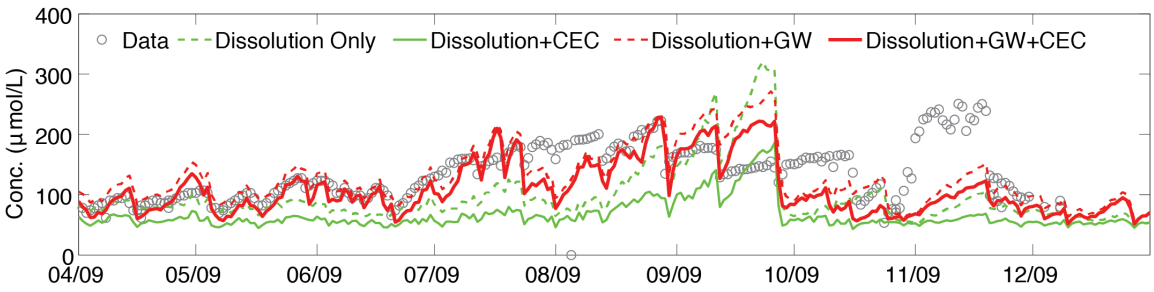

Figure 3-12 Comparison of data (circles) and model prediction of stream outlet Mg concentration in 4 scenarios: dissolution only (dashed green), dissolution with cation exchange (solid green), dissolution with groundwater influx (dashed red), dissolution with both GW and CEC (solid red, best fit case shown in figure 8).

To demonstrate the effects of different processes on the stream Mg concentration, Figure 3-12 compared simulation outputs for four scenarios, each with proper spin-up and initialization. In addition to the best fit case with all relevant dissolution, cation exchange, and groundwater influx, three additional scenarios considered here are a dissolution only case (dissolution-Only), a case with dissolution and cation exchange reactions without groundwater influx (dissolution+CEC), a case with dissolution and groundwater influx without cation exchange (dissolution+GW). Comparison between the dissolution-Only and dissolution+CEC demonstrates the buffering effects of the ion exchange. The dissolution-Only case demonstrates much more variations in Mg concentration. When the watershed is dry in mid-September, for example, the [Mg] at the stream outlet can reach twice the value observed in the model with cation exchange. The Mg groundwater influx introduces additional Mg mass in the stream, as shown in the dissolution+GW and dissolution+CEC+GW compared to their corresponding counterparts without groundwater influx. The cation exchange still acts as a buffer to bring down Mg concentrations, especially when there are large changes in the system. The effect of CEC is smaller however smaller with the presence of GW influx.

Concentration-discharge relationships. In Shale Hills, where stream discharge (Q) varies over almost 6 orders of magnitude, the stream [Mg] varies by a maximum of a factor of four. The power law slopes are -0.0564 (±0.0051) and -0.0458 (±0.0042) for the data and for the best fit model (represented as the 1X case with GW in Figure 13C), respectively. The Mg behavior is thus chemostatic because of the balance between the interactions among clay dissolution and groundwater influx as sources, discharge as the outflux, and ion exchange as the temporary storage. In spring and winter, abundant water leads to more mineral surfaces bathed in

flowing water and higher dissolution rates throughout the catchment, adding more Mg mass into water. The increased Mg mass however are also diluted by larger water volume and high ~~water volume~~ flushing rates out of the watershed, as shown in Figure 3-9. In the drier summer, although the evaporation is increasing the Mg concentration, [Mg] is maintained near-constant by cation exchange reactions.

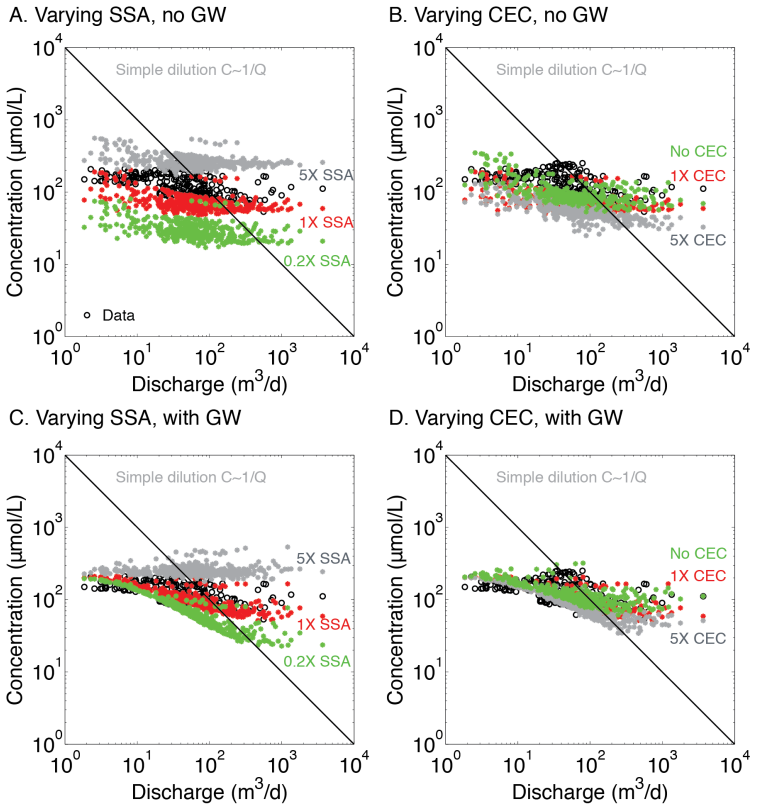

Figure 3-13 Effects of three important parameters in determining the CQ relationship for Mg. A: The effect of varying specific surface area (SSA) without including the groundwater (GW) influx. B: Effect of varying cation exchange capacity (CEC) without including GW influx. C: Same as A except including a GW influx. The red dots are output from the best fit model with GW and with SSA and CEC in the base case (1X SSA and 1X CEC). D: Same as B except including the GW influx.

To explore the role of different processes, Figure 3-13 compares cases with different processes by varying SSA for clay minerals and CEC under conditions with and without including groundwater influx. In each case, only one parameter is changed while all other parameters are kept the same as the best fit model in the base case (1X SSA and 1X CEC). Table

4 documents the average stream [Mg] and the CQ slope b. As shown in Figure 3-13A for cases without groundwater, although higher Mg release rates result from higher surface area and lead to proportionally higher [Mg] in discharge, changing SSA by 25 times does not affect the CQ slope much. Varying CEC also results in negligible impact on the CQ slope (Figure 3-13B). This suggests that although cation exchange stores large Mg mass on soil surfaces, it has relatively minor impact on the CQ behavior when clay dissolution provides the primary Mg source.

The groundwater influx affects the CQ behaviors by introducing an additional Mg source. Under low discharge conditions, the groundwater concentration dominates the stream concentration, leading to very similar concentrations under all parameter conditions (Figure 3-13 CD). For the low SSA case (Figure 3-13C), the Mg dissolution rate is low and the primary Mg source is the constant groundwater that does not increase when discharge increases. This leads to a CQ relationship which shows more of a dilution trend with decreasing concentration as discharge increases. The CQ slope in fact progressively becomes steeper (more of a dilution trend) as the SSA values decrease from 5X to 0.2X with groundwater influx becoming the increasingly dominant Mg source. In contrast, with fixed SSA and groundwater influx (Figure 13D), varying CEC does not significantly change the CQ slope. The 5X CEC case exhibits some dilution behavior with a slope of -0.25. This is largely because it the Mg concentrations in the stream in the 5X CEC case is lower so that the constant GW influx is more dominant compared with other cases with less CEC, leading to a system that is more responsive to the dilution effect brought by high discharge.

Table 3-4 Average Mg concentrations and slope of CQ curve

			Average Mg (μ M)	**b**
No GW influx	Varying SSA	0.2 X	38.23	-0.08
		1.0 X	79.22	-0.02
		5.0 X	273.89	-0.03

	Varying CEC	0.0	82.06	-0.12
		1.0 X	79.23	-0.02
		5.0 X	64.14	-0.09
With GW influx	Varying SSA	0.2 X	72.49	-0.34
		1.0 X	104.36	-0.05
		5.0 X	252.58	0.01
	Varying CEC	0.0	121.09	-0.13
		1.0 X	104.36	-0.05
		5.0 X	89.93	-0.25

5. Discussion

This work emphasizes the importance of different Mg sources in determining the CQ relationship, as shown in Figure 14. Here we partition the Mg mass flux coming from clay dissolution ($Flux_D$) and mineral dissolution into regional groundwater ($Flux_G$). Importantly, both of these fluxes derive from mineral dissolution but the first occurs largely along hillslopes (clay dissolution) in the shallow regolith while the second largely at depths of the regional groundwater table under the valley floor (carbonate dissolution). When the ratio $Flux_D$ / $Flux_G$ is high, meaning that clay dissolution in shallow regolith provides the major Mg source, the watershed maintains a self-balance between hydrological and geochemical processes because the clay dissolution in shallow regolith and discharge respond similarly to surface hydrological dynamics dictated by precipitation and evapotranspiration. In other words, with high water content and high discharge, dissolution rates increase proportionally because the surface area of reacting minerals in contact with flushing water increases. The increase in dissolved mass is therefore diluted by a proportionally larger water volume during periods of high connectivity, maintaining relatively constant concentrations under different flow regimes. The model emphasizes that the dominant control on the chemostasis of Mg is the relatively constant ratio of mineral surface area (A) and porewater volume (V) that are connected to the stream in the shallow regolith. Both A and V

increase equivalently as connectivity changes in the watershed. This actually occurs also for Cl chemostatic behavior, although no dissolution is involved. Namely, the mobilization of the "trapped" Cl mass grows proportionally to the connected watershed pore water volume and the discharge, therefore maintaining a relatively constant concentration in the stream.

In contrast, when the $Flux_D$ / $Flux_G$ ratio is low, meaning $Flux_G$ then provides a relatively dominant and constant Mg source that is not as responsive to surface hydrological processes, dilution (decreasing concentration with increasing discharge) occurs. GW influx, however, if becomes the dominant mass influx in the stream, leads to more dilution behavior, the opposite of chemostasis. This is largely due to the fact that groundwater is already fully saturated and groundwater flow tends to be slow, leading to unresponsive or slower responsive nature of the chemical weathering in groundwater and relatively constant flux into the stream.

Ion exchange plays secondary role in the chemostasis of Mg. Ion exchange buffers the system and controls the stream [Mg] at times of extreme hydrological conditions such as intense rainfall and very low discharge conditions, but its effect on the CQ relationship is limited compared to the effects of mineral dissolution and GW influx.

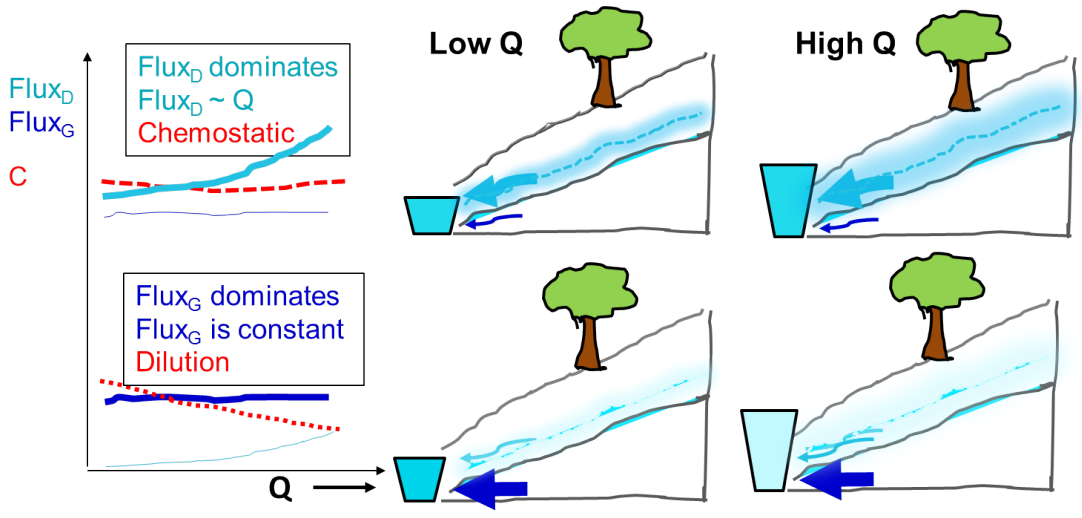

Figure 3-14 Schematics of different controls on determining the chemostasis of CQ in stream water. When the dissolution flux ($Flux_D$, light and aqua blue) is much larger than

the Mg flux from the ground water ($Flux_G$, dark blue color), chemostasis is more likely to occur because mass flux from clay dissolution increase proportionally to water volume and Q . When $Flux_D << Flux_G$, dilution is more likely to occur because of the constant, unresponsive groundwater influx to hydrological events.

The importance of the relative dominance of the different Mg sources echoes the ideas underlying the end-member mixing models proposed to explain concentration-discharge relationships (Johnson et al., 1969), as well as the better performance of the porosity-permeability-aperture model in explaining the widely observed chemostatic behavior in Godsey et al. (2009). A key feature of the porosity-permeability-aperture model is the increasing surface area (and catchment-scale dissolution rates) with higher discharge, similar to what is shown in Figure 13B. Herndon et al. (2015) argued that chemostatic behavior of geogenic species, the species that are derived from minerals, is due to the homogeneous source across the watershed but the chemodynamic behavior of bioactive solutes is caused by the heterogeneous distribution of organic matter and the associated presence of different water pools of different composition which contribute to stream chemistry under different flow regimes (Herndon et al., 2015a).

The importance of the groundwater influx as a Mg source is also highlighted here. Importantly, the source of this Mg is still dissolution but it is dictated by mineral layers in the subsurface of the valley floor. There is strong field evidence that such deep groundwater may come into direct contact with the stream through fractures in shaly watersheds like SSHCZO or in Plynlimon, Wales (Neal et al., 1997a; Neal et al., 1997b). It is estimated that in Plynlimon, groundwater influx contributes as much as 25% of stream flow (Neal et al., 1997b). Whether such groundwater influx becomes the dominant source of cations in the stream not only depends on groundwater flow rate but also on the concentrations of the cations derived from deep dissolution reactions relative to the concentrations in soil water derived from shallow dissolution reactions. In the cases simulated here, a tendency toward dilution behavior occurred only in models for dry periods when groundwater provided the primary Mg source (Figure 9) and under

conditions where Mg flux coming from clay dissolution is low with low specific surface area that groundwater influx becomes the dominant Mg source (Figure 13C, case 0.2XSSA).

If the inferences from our model for Shale Hills are extrapolated to explain the chemostatic behavior of geogenic elements (Na, Si, Ca, Mg) that was reported in 59 watersheds on different lithologies in different climatic and hydrological conditions (Godsey et al., 2009), one might conclude that groundwater influx is a relatively minor influence on chemostasis for geogenic cations in those streams. In other words, the prevalence of chemostasis is due to the relatively constant *A/V* ratio rather than the importance of GW influx.

However, it is also possible that most watersheds also host deep mineral dissolution reactions that always provide a source of geogenic elements in groundwater that recharges into the mouth of the stream, contributing to chemostasis under low-flow conditions. For example, Ca and Mg may commonly be enriched in groundwater under valleys where carbonates may be both dissolving and precipitating depending upon local groundwater levels (Brantley et al., 2013). Key to this idea is the observation that valleys tend to be zones of upwelling where CO_2 degassing may precipitate carbonates during some periods of time and where dissolution of these carbonates may occur at other times. Characterization and quantification of groundwater influxes, however, often represents a major challenge (Kuntz et al., 2011a) (Neal et al., 1990a; Neal et al., 1990b; Robson, 1993).

6. Conclusions

In this work we use RT-Flux-PIHM to explore the dynamics of Cl and Mg in SSHCZO. For Cl, the less connected watershed in the summer allows only low flow from a relatively small connected area to the stream, leading to trapped Cl in unconnected planar slope., Large rainfall events and wetter conditions connect a larger portion of the watershed to the stream and wash out these “old water” pockets of high Cl concentrations. This increase in mobilized Cl mitigates the

dilution effects brought by the proportionally higher water volume in the watershed, leading to relatively constant Cl concentration in stream and chemostatic behavior.

Mg is a geogenic species whose source is mostly dissolution of chlorite and illite clay (along the hillslopes) in the shallow regolith and /or those from groundwater influx. Chemostasis of Mg is maintained by mass flux dissolved out of clay along the hillslope that is responding to the water content and therefore discharge in the watershed. The surface area of mineral grains wetted by water connected to the stream (A) increases equivalently to the volume of porewater connected to the stream (V). Chemostasis is largely dictated by roughly constant A/V ratios yearlong in the catchment. In the dry summer, the low A and consequent slower clay dissolution is compensated by Mg-rich groundwater influxes at the stream mouth and lower V (i.e. low discharge). Large rainfall events flush out stored Mg on the exchange sites while also diluting the waters, leading to similar Mg concentrations in the stream waters in large and small rainfall events. The interplay between these processes evens out seasonal differences and results in chemostatic behavior of magnesium. In general, the relative constancy of A/V maintains chemostasis for Mg but the Mg-rich groundwater influx and the Mg-rich cation exchange capacity both contribute.

In contrast, when groundwater influx becomes the dominant source in the stream, dilution occurs largely due to the relatively constant and unresponsive nature of groundwater mass flux.

Released Mg^{2+} exchanges with H^{+} on cation exchange sites, especially in parts of the watershed (valley floor, swales) that are connected to the stream for much of the year. Likewise, especially during wet periods, the cation exchange capacity buffers the magnesium concentration by storing an order-of-magnitude higher magnesium on exchange sites than in pore water. Cation exchange as a storage buffer however have a secondary effect on chemostatic behavior compared to clay dissolution and groundwater influx.

Although the importance of these different processes, including chemical weathering along hillslopes and at depth and cation exchange in regulating stream chemistry has been discussed in the literature (Clow and Mast, 2010; Godsey et al., 2009; Herndon et al., 2015a), only with process-based modelling such as provided by RT-Flux-PIHM can the importance of each mechanism be interrogated. As such, the model provides the potential to resolve long-standing puzzles challenging researchers studying watershed processes. The model integrates complex hydrogeochemical processes to identify key controls under a variety of topological, hydrological, and geochemical conditions. Only with such numerical models will we ever be able to understand the intricacies of watershed scale geochemical cycling.

Chapter 4

Hydrological Controls on the Chloride Concentration Discharge Relationship

1. Introduction

Concentration-discharge (CQ) relationship is a convenient and powerful tool to analyze the hydrogeochemical response of watersheds to hydrological processes (Anderson et al., 1997; Chanat et al., 2002; Godsey et al., 2009). It can be used in watershed management simulations to estimate loads of nutrients, elements, contaminants and sediments from closely monitored discharge data (Campbell and Bauder, 1940; Ferguson, 1986; Stenback et al., 2011). In particular, concentration discharge relationship of chloride have been thoroughly studied due to its importance in understanding the transport of conservative species (Hedin et al., 1995; Kirchner et al., 2000). Chloride has generally been conceived as a tracer controlled primarily by the input from rainwater (Eriksson, 1955; Kirchner et al., 2000) and transported conservatively (Peters et al., 1998) under typical watershed conditions. As such, it is often used as a key indicator of water residence time in the field (Kirchner, 2003; Kirchner et al., 2000, 2001). It could also be used to elucidate and even quantify other processes when compared to the spatiotemporal variations of other species (Lockwood et al., 1995; Peters et al., 1998).

However, chloride concentrations in stream water are found to be quite unresponsive to variations in precipitation or discharge even though precipitation is its primary control (Kirchner, 2003). In some watersheds, chloride concentration is almost constant despite great variations in precipitation and discharge (Johnson et al., 1969; Kirchner et al., 2000). In other watersheds, chloride concentration in stream decreases as discharge increase (Anderson et al., 1997; Peters et al., 1998). Godsey et al., (2009) uses the slope of the log-log concentration discharge plot to

quantify the chemostasis of solute concentration in stream water, that is, “the system keeps concentrations constant as discharge varies”. Existing studies found such slopes for chloride concentration discharge relationship generally falls between 0 and -0.25 (Anderson et al., 1997; Johnson et al., 1969; Peters et al., 1998; Stallard and Murphy, 2014). This suggests chloride is either chemostatic or slightly diluted as discharge increase.

Many studies attempted to investigate the controls on the variations in chloride CQ relationship based on the mixing of different source waters, e.g. old soil water and new rainwater; groundwater, soil water and rainwater (Chanat et al., 2002; Evans and Davies, 1998; Hooper et al., 1990; Johnson et al., 1969). Stallard and Murphy explained the slightly dilution behavior of chloride concentration discharge relationship (Stallard and Murphy, 2014) based on End-Member mixing analysis (EMMA) (Hooper et al., 1990) and concluded that the CQ of chloride reflected the “repeated mixing of storm water with a soil–water Cl^- reservoir”. Kirchner found that the chemostatic CQ relationship could arise from a gamma water residence time distribution that is corresponding to the catchment scale advection dispersion process if the dispersivity is at the scale of the hillslope length (Kirchner et al., 2000, 2001). Duffy and Cusumano demonstrated that concentration discharge relationship for conservative tracer could be predicted from a low-dimensional model. The model indicates the shape of CQ plot is controlled by the ratio of solute residence time and hydrological response time (Duffy and Cusumano, 1998; Gelhar and Wilson, 1974). Other models are also proposed for the chemostatic behavior of reactive species (Godsey et al., 2009; Herndon et al., 2015; Maher and Chamberlain, 2014) however they are not applicable to the nonreactive chloride. However, it is still not fully clear how watershed characteristics including topography, hydrological parameters and soil properties contribute to the variations in chloride concentration discharge relationships at the watershed scale.

In recent years, there has been an ongoing discussion on how watershed connectivity impacts the generation of runoff and controls the solute transport as the small watershed responds

to rainfall and snowmelt events (Jencso et al., 2009; McGuire and McDonnell, 2010; Western et al., 2004). Such connectivity could be evaluated by the correlations between groundwater levels at different locations, e.g. hillslope, riparian and stream etc. (Jencso et al., 2009; Tockner et al., 1999). Alternatively, spatial connectivity function defined basing on thresholding certain observable variables, e.g. shallow soil moisture (top 20~30 cm soil), provides more quantitative insights into this discussion (James and Roulet, 2007; Michaelides and Chappell, 2009; Western et al., 2001). Mcguire and McDonnell argued that hillslope runoff could substantially contribute to the stream water and transport solutes when saturated zone expands to more upslope area and induce transient lateral subsurface flow (McDonnell et al., 2007; McGuire and McDonnell, 2010). However, it is still under debate whether we can use shallow soil moisture patterns as indicators of subsurface lateral flow that will mobilize solutes and older waters more upslope (van Meerveld and McDonnell, 2005; Western et al., 2004). Nonetheless, these ongoing discussions brought to our attention the importance of the intermittent, non-linear upslope lateral subsurface flow that would invalidate the basic assumption in a traditional end-member mixing analysis as the latter often requires soil water or groundwater as homogeneous storages.

In this work, we aim to understand the underlying mechanism that controls the chloride concentration discharge relationship through studying a distributed hydrological land surface and mass transport model RT-Flux-PIHM. Such a distributed model can take advantage of numerical spatial discretization to study the effects of physical heterogeneity on mass transfer, which cannot be analyzed in a conventional EMMA. The model has been carefully calibrated at Shale Hills Critical Zone Observatory and is shown to be able to reproduce key hydrological observations in the field (Qu and Duffy, 2007; Shi et al., 2013b). Based on the base case simulation, numerical experiments could be conducted to elucidate the hydrological controls on the chloride concentration discharge relationship.

2. Method

2.1 Shale Hills Critical Zone Observatory (SSHCZO)

This work studies the hydrological controls of chloride CQ relationship at Shale Hills Critical Zone Observatory (SSHCZO). The SSHCZO is a V-shaped, first order watershed (0.08 km^2) in central Pennsylvania (Qu and Duffy, 2007). The Rose Hill shale underlining the SSHCZO is a fossiliferous shale with well-developed fracture cleavage (Flueckinger, 1969). The mean annual temperature is 10^{o}C with a mean annual precipitation of 1070 mm (Jin et al., 2011a). About 50% of the precipitation contributes to evapotranspiration and the other 50% to stream discharge (Jin et al., 2014).

Extensive field surveys have provided us the topographic and hydrological properties in SSHCZO (Jin et al., 2010; Lin, 2006; Ma et al., 2010). Five types of soil have been identified in the shallow subsurface within the watershed: Berks, Weikert, Rushtown, Blairtown, and Ernest (Lin, 2006). In this work, we continue to use a spatial distribution of subsurface thickness, soil elevation, soil series and soil matrix properties discussed in previous work (Bao et al., 2015; Lin, 2006; Shi et al., 2013b). A summary of these properties is provided in Figure 4-1. Prior to this work, the hydrological parameters for hydrological land surface model Flux-PIHM have been carefully calibrated using multivariate field measurements (discharge, soil moisture, water table depth, and surface heat fluxes) in SSHCZO (Shi et al., 2014). In particular, we focus on the year 2009 to understand the hydrological controls of chloride CQ in this work due to the availability of data and calibrated model in this year (Bao et al., 2015).

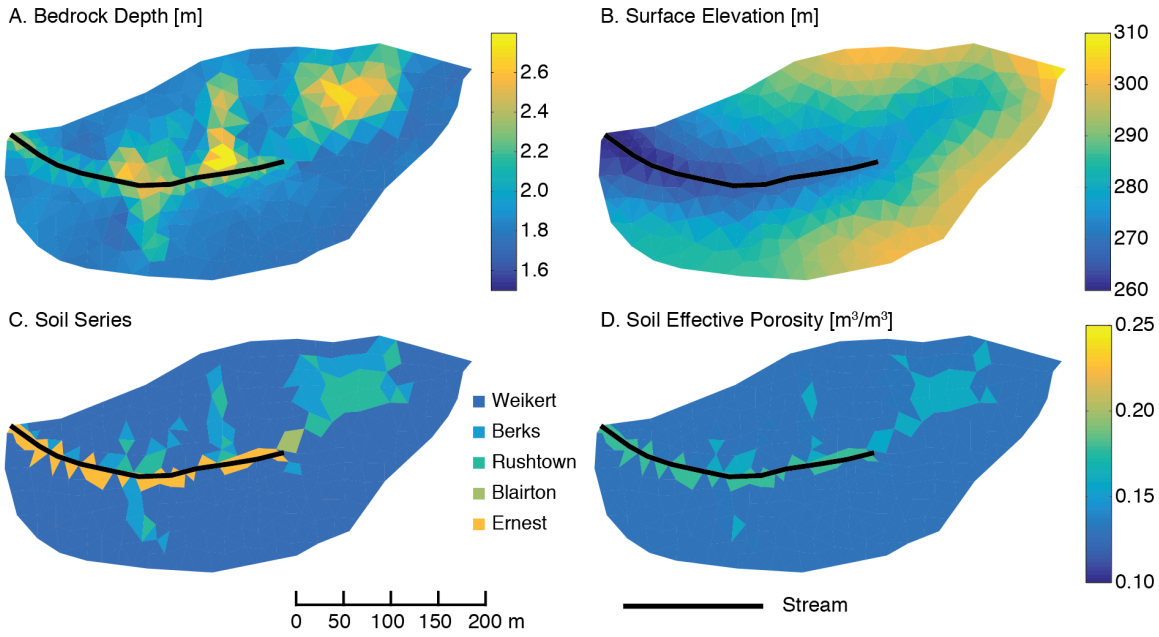

Figure 4-1. Spatial distribution of key topographic and soil properties in SSHCZO based on extensive field surveys and existing modeling work calibrated by using multivariate field measurements (Jin et al., 2010; Lin, 2006; Shi et al., 2013b): A, depth to bedrock [m]; B, surface elevation [m]; C, identified soil series; D, soil average effective porosity in each element [m^3/m^3].

For the non-reactive transport of chloride, it is believed majority of the chloride entering SSHCZO comes from precipitation events. The average chloride concentration in rainwater in 2009 was 3.05 (±4.20) μmol/L, as measured at Leading Ridge as part of the National Atmospheric Deposition Program, i.e., 7.11 miles from SSHCZO (Lamb and Bowersox, 2000). Solute concentration in throughfall water is reported to be 1.07~4.70 times higher than rainwater concentration (Polkowska et al., 2005) due to the contributions from dry deposition, cloud-water deposition and canopy wash-off (Svensson et al., 2012). Therefore, we use a concentration multiplier to consider this effect, which is 1.8 in this work to match the observed chloride concentration in the field. The Shale Hills watershed is underlain by deeply fractured shale. As such, much deeper groundwater might contribute to the stream through fracture flow, as indicated in (Neal et al., 1997). A chloride influx of 250 mol/year from deeper groundwater is also added to the system to account for the difference between the total loss of chloride from discharge (940

mol in 2009) and total input of chloride from precipitation (690 mol in 2009, considering the throughfall chloride concentration multiplier). The average concentration of groundwater chloride in groundwater wells in SSHCZO from 2006 to 2010 is 62.31 μmol/L with a standard deviation of 25.41 μmol/L.

In this work, we will use three methods with decreasing complexity to demonstrate the effect of different level of watershed details on the evolution of stream water chloride. The first method is a RT-Flux-PIHM simulation on the non-reactive transport of chloride (Bao et al., 2015). This model is a watershed scale distributed model integrates hydrological, land surface and mass transfer processes, calibrated by hydrological and geochemistry measurements made in SSHCZO. In the second method, we consider the dynamic end-member mixing (dEMMA) in the stream outlet, in which stream water chloride concentration is calculated as the flow rate weighted average of different end-members (Stallard and Murphy, 2014). The third method is to model the continuous source water mixing within a well mixed reservoir (Gelhar and Wilson, 1974). In this model, the entire watershed is assumed to be a homogeneous, constantly well-mixed "box" of water that receives from rainwater and deeper groundwater influx. This "box" of water is also subject to evapotranspiration and discharge that removes water and solutes. Building on those understandings, we will test the sensitivity of chloride concentration discharge relationship to key watershed characteristics using RT-Flux-PIHM, which is the most comprehensive.

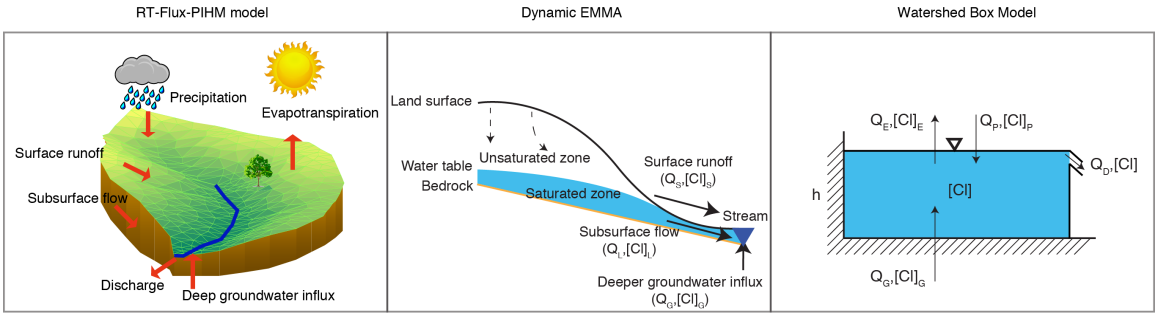

Figure 4-2 Schematic plot of the three methods used in this work. Left: Finite volume based distributed RT-Flux-PIHM model that simulates the coupled hydrological land surface process and the non-reactive transport of chloride. Middle: Dynamic end-member mixing analysis (dEMMA) where end-members are mixed at the stream outlet. (Q_S, $[Cl]_S$) are the flow rate [$m^3/(m^2d)$] and concentration [mol/m^3] of surface runoff; (Q_L, $[Cl]_L$) are the flow rate [$m^3/(m^2d)$] and concentration [mol/m^3] of subsurface flow; (Q_G,$[Cl]_G$) are the flow rate [$m^3/(m^2d)$] and concentration [mol/m^3] of deeper groundwater influx. Right: Watershed scale "box" model where end-members are mixed in a simplified linear reservoir. (Q_E, $[Cl]_E$) are the rate [$m^3/(m^2d)$] and concentration [mol/m^3] of evapotranspiration; (Q_P, $[Cl]_P$) are the flow rate [$m^3/(m^2d)$] of precipitation and throughfall concentration [mol/m^3]; (Q_G,$[Cl]_G$) are the flow rate [$m^3/(m^2d)$] and concentration [mol/m^3] of deeper groundwater influx. Q_D [$m^3/(m^2d)$] is the discharge and [Cl] [mol/m^3] is the chloride concentration in discharge and in the linear reservoir.

2.2 RT-Flux-PIHM model

In this work, we use an integrated simulator RT-Flux-PIHM to explicitly models hydrological, land surface and reactive transport processes in in Shale Hills Critical Zone Observatory (Bao et al., 2015). For non-reactive species chloride, only advection diffusion/dispersion equation is solved in RT-Flux-PIHM using finite volume method:

$$\frac{\partial}{\partial t}(V\phi[\mathrm{Cl}]) + \nabla(-\boldsymbol{D}\nabla[\mathrm{Cl}] + \boldsymbol{u}[\mathrm{Cl}]) = 0 \quad (1)$$

where ϕ is the porosity in the control volume [m^3/m^3]; [Cl] is chloride concentration; V is the volume of the control volume [m^3]; $\boldsymbol{D}$ is the combined dispersion/diffusion flux tensor [m^4/s] and $\boldsymbol{u}$ is the Darcian flux vector [m^3/s].

During each rainfall, the canopy layer will intercept a fraction of rainwater and the rest of rainwater penetrate the canopy layer and becomes throughfall. The throughfall water will either infiltrate into soil or be directed to flow as surface runoff, depending on the infiltration rate. The infiltration throughfall water will be mixed with the soil water in place at each element. Then they will either recharge into the local groundwater or become evaporated. The local groundwater will be able to move laterally until they merge to the stream. In RT-Flux-PIHM, lateral subsurface

flow is assumed to only emerge in saturated zone, or the "perched groundwater". When the "perched groundwater" table is higher than certain threshold, macro pore lateral flow is then considered. When the "perched groundwater" table is lower than that threshold, only saturated zone lateral flow is considered based on Darcy's law. Therefore, the subsurface lateral flow here is a sum of the occasional macro flow that sweeps the unsaturated zone and the saturated zone flow that flows beneath the perched groundwater table. Both belong to the shallow, above bedrock reservoir as conceptualized by (McDonnell et al., 2007; McGuire and McDonnell, 2010). In RT-Flux-PIHM simulation, the chloride concentration of deeper groundwater is set to be 55 μmol/L to best fit the measured stream chloride concentration, which is within the range of the measured chloride concentration in groundwater wells. The influx of deeper groundwater is assumed to be penetrating near the outlet of the stream in RT-Flux-PIHM simulation.

2.3 Dynamic End-Member Mixing Analysis (dEMMA)

As proposed by many existing works (Evans and Davies, 1998; Stallard and Murphy, 2014), the concentration of stream water at the outlet could be modeled as the flow rate weighted average of concentrations of the different mixing end members. In later discussions, we will refer this method as dynamic End-Member mixing analysis (dEMMA). Based on the conceptual model proposed by (McGuire and McDonnell, 2010), the discharge at the outlet of the stream is:

$$Q_D(t) = Q_S(t) + Q_L(t) + Q_G \quad (2)$$

where $Q_D(t)$ is the discharge at outlet [$m^3/(m^2d)$]; $Q_S(t)$ is surface runoff [$m^3/(m^2d)$]; $Q_L(t)$ is the subsurface lateral flow that contributes to stream [$m^3/(m^2d)$]; Q_G [$m^3/(m^2d)$] is the influx of groundwater from a much older and deeper reservoir; all normalized by area of the watershed.

Then the chloride concentration at the stream outlet could then be expressed as:

$$[\mathbf{Cl}]_D = \frac{Q_S(t)[\mathbf{Cl}]_S + Q_L(t)[\mathbf{Cl}]_L + Q_G[\mathbf{Cl}]_G}{Q_D(t)} \quad (3)$$

To calculate $[\mathbf{Cl}]_D$, the flow rate and the concentration for each type of flow are needed. The surface runoff $Q_S(t)$ contributing to the stream could be obtained from RT-Flux-PIHM by:

$$Q_S(t) = \frac{\sum_{i=1}^{N_{riv}} (q_{Si,left}(t) + q_{Si,right}(t))}{A_{watershed}} \quad (4)$$

where $q_{Si,left}(t)$ and $q_{Si,right}(t)$ are the surface runoff flowing into stream element i from the left and right bank at time t [m^3/d], respectively; $A_{watershed}$ is the total area of the watershed [m^2]; N_{riv} is the number of stream segments. Surface runoff concentration $[Cl]_S$ is assumed to be the throughfall water concentration, which was calculated as the product of the concentration multiplier (1.8) and the rainwater concentration from the time series of measured rainwater concentration.

Similarly, the subsurface flow rate $Q_L(t)$ could be calculated based on the water inputs from subsurface to the stream along the riverbank:

$$Q_L(t) = \frac{\sum_{i=1}^{N_{riv}} \left[q_{i,left}(t) + q_{i,right}(t) \right]}{A_{watershed}} \quad (5)$$

where $q_{i,left}(t)$ and $q_{i,right}(t)$ are the subsurface flow flowing into stream element i from the left and right bank [m^3/d], respectively. Chloride concentration of the subsurface water could be estimated by the annual average of measured soil water chloride concentration, which is 29.88 μmol/L in SSHCZO.

The influx of deeper groundwater could be estimated from the total influx of chloride due to deeper groundwater and the groundwater chloride concentration. For simplicity, we assumed a constant deeper groundwater influx rate:

$$Q_G = \frac{F_G}{[\mathbf{Cl}]_G A} \tag{6}$$

where F_G is the total mass influx of chloride from deeper groundwater [mol/d]; A is the total area of the watershed [m^2]. From RT-Flux-PIHM, we obtained the F_G=0.68 mol/d and A = 8.417×10^4 m^2. Therefore, $Q_G = 1.48\times10^{-4}$ $m^3/(m^2d)$.

2.4 Watershed Box Model

In the third method, we assume the watershed could be represented by a well-mixed reservoir that receives from rainwater and deeper groundwater influx. The mixing of different source waters happens in this well mixed reservoir and the chloride concentration will change accordingly. This "box" of water is also subject to evapotranspiration and discharge that removes water and solutes. The water balance of this reservoir could be stated as (Gelhar and Wilson, 1974):

$$\frac{dV(t)}{dt} = Q_P(t) + Q_G - Q_E(t) - Q_D(t) \tag{7}$$

where V is the water storage in watershed [m^3/m^2], normalized by watershed area; $Q_P(t)$ is precipitation [$m^3/(m^2d)$]; Q_G is the influx of deeper groundwater [$m^3/(m^2d)$]; $Q_D(t)$ is the discharge at outlet [$m^3/(m^2d)$]; $Q_E(t)$ is the evapotranspiration [$m^3/(m^2d)$], all normalized by watershed area. The $Q_D(t)$ and $Q_P(t)$ are usually available in watersheds as time series data. The influx of deeper groundwater, Q_G could be estimated from the total influx of chloride due to deeper groundwater and the groundwater chloride concentration. The groundwater influx rate and the concentration is set to be the same as in the previous method.

The $Q_E(t)$ could be estimated based on field measurement in surface temperature, wind speed, radiation, humidity, etc. (Hargreaves and Samani, 1982; Penman, 1948; Priestley and

Taylor, 1972). In this study, we uses the $Q_E(t)$ estimated by Flux-PIHM (Shi et al., 2013b). In Flux-PIHM, evapotranspiration is calculated at each element based on Pennman-Monteith's method. The $Q_E(t)$ for the entire watershed is then calculated by the element area weighted average of evapotranspiration in each element.

The mass of chloride in this watershed could be written as, assuming outflowing discharge with the same chloride concentration as the reservoir:

$$\frac{d\{V(t)[\mathbf{Cl}]\}}{dt} = Q_P(t)[\mathbf{Cl}]_P + Q_G - Q_E(t)[\mathbf{Cl}]_E - Q_D(t)[\mathbf{Cl}] \quad (8)$$

where $[\mathbf{Cl}]$, $[\mathbf{Cl}]_P$, $[\mathbf{Cl}]_G$ and $[\mathbf{Cl}]_E$ is chloride concentration in reservoir, throughfall, deeper groundwater and evapotranspiration, respectively [mol/m^3]. For simplicity, $[\mathbf{Cl}]_E$ is assumed to be zero in this work. Throughfall concentration $[\mathbf{Cl}]_P$ is calculated as the product of the concentration multiplier (1.8) and the rainwater concentration from the time series of measured rainwater concentration. Therefore, by solving for the water storage and chloride concentration in reservoir together using method detailed in (Gelhar and Wilson, 1974) with hourly time step, we will be able to track the chloride concentration evolution in stream water numerically. The initial condition [$V(t0)$, $[\mathbf{Cl}]_{t0}$] need be fitted for this model. An initial concentration of 29.88 μmol/L chloride is assumed based on field measurements. An initial storage $V(t0)$ of 0.05 m^3/m^2 is used to best fit the concentration data in discharge. A numerical algorithm has been written to model the stream water chloride concentration in MATLAB (MATLAB and Statistics Toolbox Release 2014a, The MathWorks, Inc., Natick, Massachusetts, United States).

2.5 Hydrological Connectivity

As revealed by many researchers, watersheds are dynamically connected throughout the year (James and Roulet, 2007; Jencso et al., 2009; McGuire and McDonnell, 2010; Western et al., 2001). Spatial connectivity function has been proposed as a rigid quantification of the hydrological connectivity (Allard, 1993; Michaelides and Chappell, 2009; Western et al., 2001). In this work, the spatial connectivity is assessed following the approaches detailed in (Western et al., 2001). Although many studies used shallow soil moisture to interpret the hydrological connectivity at watershed scale, it is still unclear to us whether a moisture based method would be able to represent the transient subsurface flow that mobilize old water and solutes (van Meerveld and McDonnell, 2005). As we are able to directly extract lateral subsurface flow velocity from RT-Flux-PIHM simulation, we could assess the connectivity function directly based on lateral flow velocity in this work. The connectivity function in Western's method describes the probability of two pixels being connected through a spatially continuous connection with higher than threshold value (e.g. 75th percentile) in indicator variables such as shallow soil moisture. In this work, we use the subsurface lateral flow velocity as the indicator variable:

$$\tau(h) = P(x \leftrightarrow x+h \mid x \in A, x+h \in G) \quad (9)$$

where $\tau(h)$ is the probability of two pixels being physically connected with a separation of h; h is the spatial separation of the two pixels [m]; x and $x+h$ represent the two pixels; G is the set of pixels in simulation domain and A is the subset of G that has higher than threshold indicator value. Two pixels are connected only if there is a continuous path of pixels with indicator value larger than threshold. Following the algorithm in (Western et al., 2001), a code was written in MATLAB (MATLAB and Statistics Toolbox Release 2014a, The MathWorks, Inc., Natick, Massachusetts, United States) to 1) identify zones with higher than indicator value; 2) label connected zones; 3) Loop through all pixels (and its peers) to calculate the connectivity function.

Only omnidirectional connectivity is evaluated in this work. , Integral connectivity scale was calculated based on the integral of connectivity function over separation to quantify the hydrological connectivity at the watershed scale (Western et al., 2001):

$$I_{CS} = \int_0^\infty \tau(h)\, dh \tag{10}$$

2.6 Sensitivity Analysis

We also investigated how are $[Cl]_D$ and $[Cl]_D$-Q_D relationship affected by a suite of soil properties and rainfall conditions (precipitation amount). Among these, we found that Cl concentration and C-Q relationship are most sensitive to soil effective porosity Θ_e [m^3/m^3], Van Genuchten parameter β [-], macro pore conductivity K_{mac} [m/d] and precipitation. The sensitivity analysis performed here used a global calibration coefficient (GCC) approach detailed in (Pokhrel and Gupta, 2010; Shi et al., 2014), that is, the corresponding parameter value in each grid block are multiplied by a GCC. As such, spatial heterogeneity in the corresponding model parameter is kept to the same extent. The a priori soil parameter values and the plausible ranges of GCCs are listed in table 4-1.

Table 4-1 RT-Flux-PIHM model parameters for the SA, their a priori values and ranges of plausible GCCs. The references are 1) (Beven and Binley, 1992) 2) (Gupta et al., 1999) 3) (Anderton et al., 2002) 4) (Tang et al., 2006) 5) (Shi et al., 2013c)

Parameter	A priori value					Plausible range of GCCs	References
	Soil type						
	Weikert	Berks	Rushtown	Blairton	Ernest		
Θ_e [m^3/m^3]	0.48	0.32	0.33	0.29	0.34	0.3~1.2	1,2
β [-]	1.20	1.21	1.33	1.33	1.32	0.95~1.6	3,4
K_{mac} [m/d]	1811.00	909.00	520.00	87.00	393.00	0.01~100	5

Based on data from the Pennsylvania State Climatologist website (http://climate.psu.edu/data/ida/index.php?t=3&x=shef&id=STCP1), the annual precipitation in SSHCZO ranges from 720 mm to 1500 mm in the past 30 years. This corresponds to a GCC of precipitation range of 0.67~1.4. In varying the precipitation, only the magnitudes of every precipitation events are altered. The temporal patterns of the precipitation events in SSHCZO are not changed.

Single-parameter tests, or one-at-a-time (OAT) sampling is performed in this SA, in which only one parameter value is perturbed while the values of all other parameters kept to the base case values from the calibrated model parameters in Flux-PIHM that reproduced multivariable observations (Shi et al., 2013b). Parameter values are sampled linearly in the plausible GCC space. For parameter that has a wide range of GCC (K_{mac}), we sampled parameter values linearly in the logarithmic plausible GCC space. A list of GCCs used in this SA for each parameter could be found in table 2.

Table 4-2 List of GCC values in single parameter SA test

	Global Calibration Coefficients				
	A	B	C	D	E
Θ_e	0.3000	0.5250	0.7500	0.9750	1.2000
β	1.0000	1.1500	1.3000	1.4500	1.6000
K_{mac}	0.0100	0.1000	1.0000	10.000	100.00
Q_P	0.6700	0.8525	1.0350	1.2175	1.4000

To evaluate the $[Cl]_D$-Q_D relationships under different conditions, linear regression is used:

$$\log([\mathbf{Cl}]_D) = a\log(Q_D) + b \tag{11}$$

For each case, the slope *a* of linear regression and the coefficient of determination (R^2) are reported.

3. Results and Discussions

3.1 Watershed Connectivity and the Role of Big Precipitation Events

Hydrological connectivity. As revealed by many researchers, watersheds are dynamically connected throughout the year (James and Roulet, 2007; Jencso et al., 2009; McGuire and McDonnell, 2010; Western et al., 2001). In SSHCZO, watershed hydrological connectivity is affected by seasonality and precipitation events.

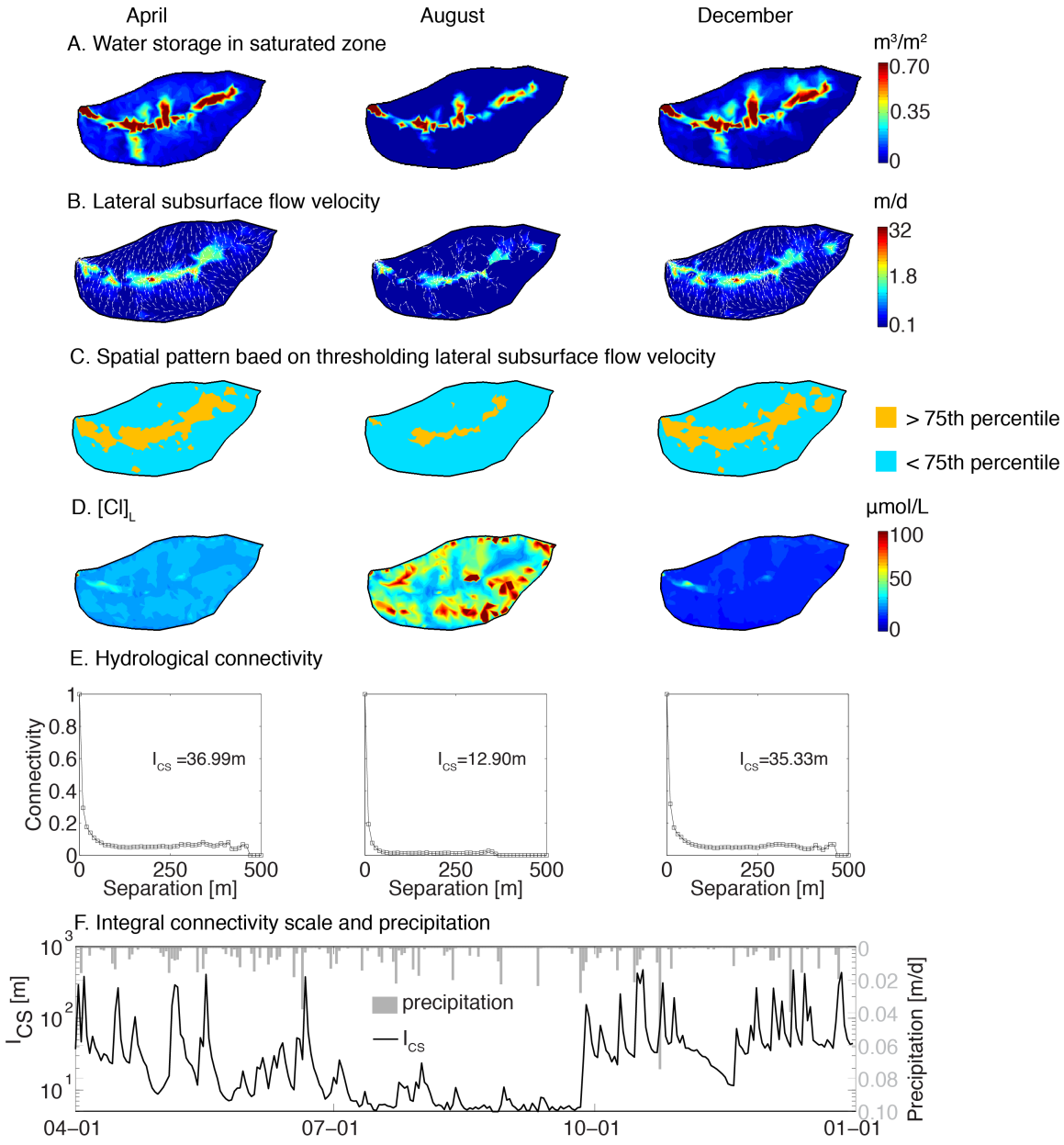

Figure 4-3 A: water storage in the saturated zone (m^3/m^2); the saturated zone in subsurface drives lateral flow velocity based on Darcy's law; B: velocity of lateral saturated zone flow from RT-Flux-PIHM in logarithm color scale. White arrows indicate the directions of the lateral flows. Most saturated zone flows are directed towards the nearest stream or swales. Lateral flows on ridges are often directly flowing along the ridge towards the outlet of the stream; C: spatial pattern of flow velocities when 75^{th} percentile velocity was used as a threshold; D: [Cl] concentration in the subsurface; E: omnidirectional connectivity as a function of separation (distance between grid blocks) at different times and the corresponding integral connectivity scale (I_{CS}) [m]; F: I_{CS} and precipitation as a function of time. The I_{CS} here is in logarithmic scale. The three dates selected here has no significant preceding rainfall events to exclude the impact of

preceding rainfalls. Sudden increase in hydrological connectivity correlates to big rainfall events.

Hydrological connectivity varies significantly in the SSHCZO in different season. In spring and winter (the first and third columns), SSHCZO is mildly connected, as saturated zones in riparian and swales drives subsurface water flows to the stream. As evapotranspiration becomes higher in summer, the saturated zone drastically shrank and led to a great decrease in the subsurface flow as well as hydrological connectivity (Figure 4-3A~C).

Such changes in hydrological connectivity have significantly influenced the chloride transport in SSHCZO. As saturated zone retreated from the upslope region from spring to the summer, chloride in the upslope planar region became isolated. Its concentration is further amplified as evapotranspiration proceeded, as shown in figure 4-3D. Over time, the watershed is partitioned into mobile subsurface water characterized by lower chloride concentration and an relatively immobile water pool that trapped chloride with much higher concentration. Although all the connected zones have low $[Cl]_L$, not all low $[Cl]_L$ zones corresponds to higher lateral flow velocity or connected zones. This is because snapshots of lateral flow velocities are transient, while $[Cl]_L$ also depends on the preceding flow activities. Between different snapshots, precipitation events would advect chloride, leading to low $[Cl]_L$ channels along swales that may not necessarily shown as connected in the three selected snapshots. In December, these previously trapped chlorides in the upslope is released and [Cl] returned to a more homogeneous distribution.

Consistent with the spatial patterns, hydrological connectivity function shows much lower connectivity in the dry summer and higher values in the wetter spring and winter. The integral connectivity scale decreased from 36.99 in Apr. 1st to 12.90 in Aug. 1st (Figure 4-3E). Spikes of I_{CS} follows closely the precipitation events except in the summer with prolonged dry period due to high evapotranspiration (Figure 4-3F). In general, low I_{CS} indicates a very narrow

drainage line while higher I_{CS} indicates a wider drainage area sometimes including the entire watershed (Western et al., 2001). Each spike in I_{CS} indicates a sudden increase in watershed hydrological connectivity induced by rainfall (Figure 4-3F).

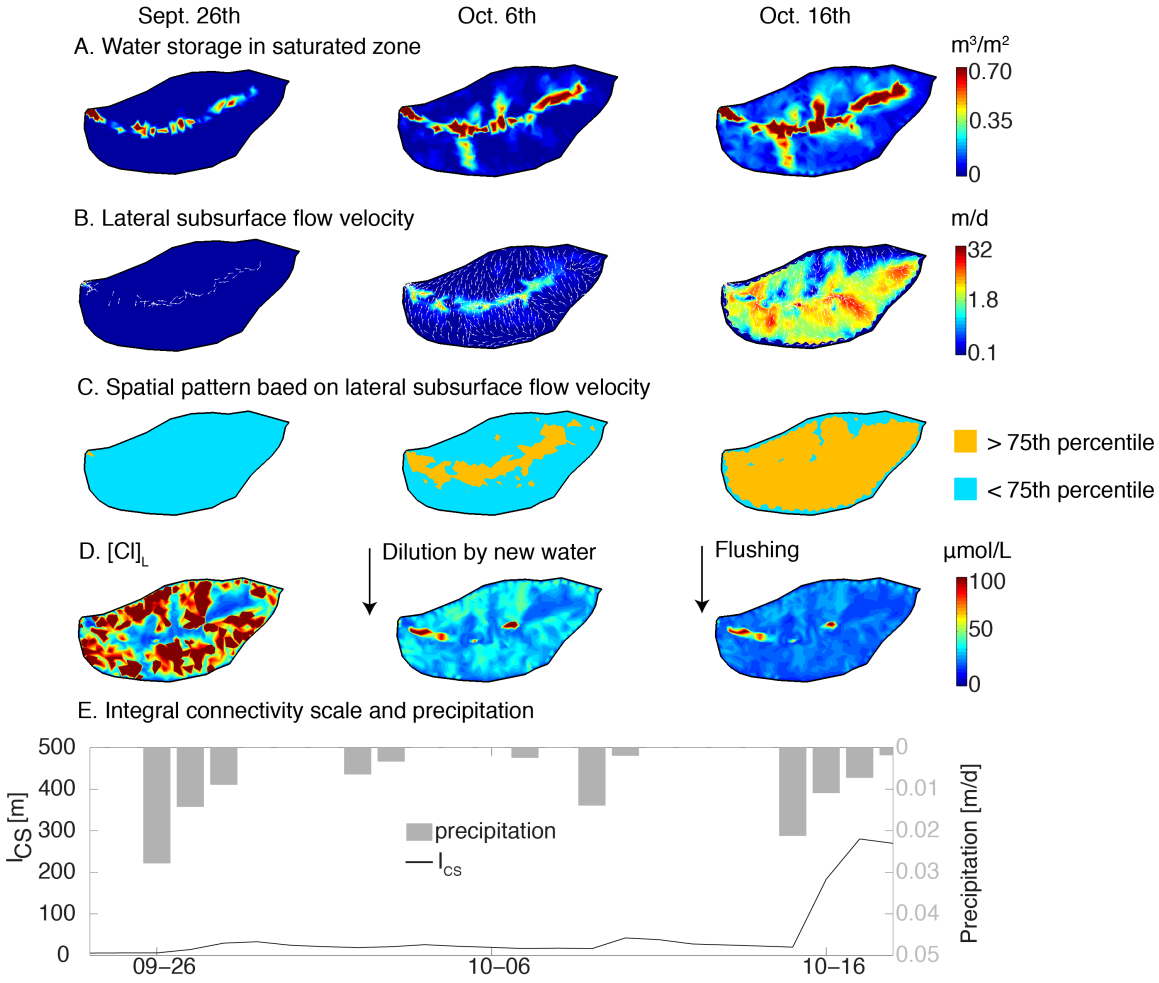

Figure 4-4 A: water storage in the saturated zone [m^3/m^2], which drives lateral flow velocity based on Darcy's law in RT-Flux-PIHM; B: velocity of lateral saturated zone flow in logarithm color scale; The white arrows indicate the directions of the lateral flows. C: spatial pattern of flow velocity when 75th percentile velocity was used as a threshold; D: [Cl] concentration in the subsurface; F: I_{CS} [m] and precipitation as functions of time.

Big rainfall events. Sudden improvements in watershed hydrologic connectivity will mobilize the previously immobile subsurface water pool. As an example, a series of rainfall in between September and October flushed the high $[Cl]_L$ soil water in the summer. In late

September, SSHCZO was still very dry and there were essentially no saturated zone or subsurface flow. Due to the lack of subsurface flow and ongoing evapotranspiration, $[Cl]_L$ reached its maximum level of the year with a volume-weighted average concentration of 67 μmol/L (Figure 4-4 A~C, left figures). A series of rainfall wetted the watershed in late September and early October, leading to a gradual expansion of the saturated zone and an increase in subsurface flow (Fig 4-4 A~C, mid figures). The incoming rainwater also diluted subsurface wa4ter and reduced $[Cl]_L$. On October 15th, a large storm event hit SSHCZO and suddenly led to a rapid expansion of saturated zone, much elevated subsurface flow and extremely high watershed hydrological connectivity (Fig. 4-4A~C, right figure). The sudden development of subsurface flow flushed a substantial amount of chloride into the stream, dropping the volume-weighted average $[Cl]_L$ to 23 μmol/L. Figure 4-4D shows that I_{CS} gradually increased as saturation expanded from Sept. 26th to Oct. 15th and then suddenly spiked up to 280.21.

3.2 Stream Chloride Concentration

Dynamic EMMA and RT-Flux-PIHM results

Based on the end-member mixing model, $[Cl]_D$ is determined by the contributions from surface runoff, subsurface flow and deeper groundwater influx. As a result, $[Cl]_D$ fluctuates as the contributions from different source waters vary. Here we examine how Q_D, Q_S, Q_L and Q_G at and their concentrations vary at different times, and how $[Cl]_D$ vary with different water dynamics.

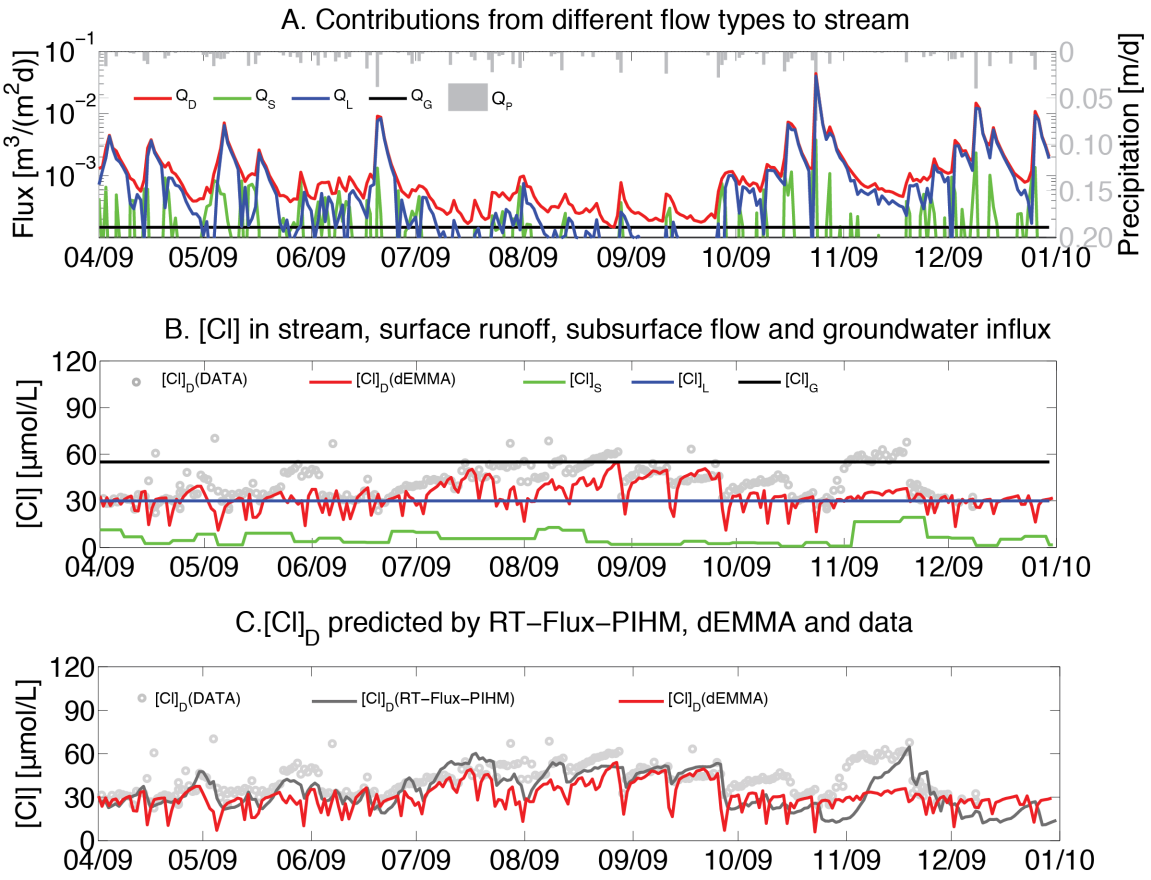

Figure 4-5 A: contributions of different flow types to the stream as functions of time for dynamic EMMA method, flow rates are from RT-Flux-PIHM simulation. B: stream chloride concentration in data and calculated based on the dynamic EMMA method, together with chloride concentrations in different flows. C: stream chloride concentration predicted by RT-Flux-PIHM and by dEMMA with actual data.

In figure 4-5A, flow rates of different flow types fluctuate constantly throughout our analysis. A typical progression of dominance in stream water during each precipitation event is found to be: 1) surface runoff; 2) subsurface flow. Such sequences have been repeatedly observed in watersheds of Pennsylvania (DeWalle and Pionke, 1994; Pionke et al., 1988). Surface runoff tends to be short pulses, while subsurface flow comes in slightly later with longer time duration after each precipitation event. In summer, when rainfall events are absent, the stream is dominated by deeper groundwater influx. In sum, from Apr. 1st to Dec. 31st 2009, 57.45% of total

days the stream water is dominated by subsurface flow, followed by 28.73% of time by deeper groundwater influx and 13.82% of time by surface runoff.

Different source waters have very different chloride concentrations, as shown in figure 4-5B. In general, $[Cl]_S$ is always the lowest among the three end-members . The $[Cl]_G$ is assumed to be constant over time. The $[Cl]_L$ is calculated based on RT-Flux-PIHM simulation, which takes into account the impact of hydrological land surface processes (precipitation, evapotranspiration, lateral flow to stream, etc.). Therefore, $[Cl]_L$ evolves in time as the subsurface water is dynamically mixed. The $[Cl]_L$ decreases when throughfall water with a lower chloride concentration enters subsurface. In summer, $[Cl]_L$ gradually increases due to higher evapotranspiration and surpassed $[Cl]_G$.

The resulting $[Cl]_D$ modeled by dynamic EMMA method reflects changes both in flow rates and source water concentrations. When stream water is dominated by subsurface flow, $[Cl]_D$ is also closely tracking $[Cl]_L$ except for summer. In summer, stream is more dominated by deeper groundwater influx, so $[Cl]_D$ was approaching the level of $[Cl]_G$. Occasionally, $[Cl]_D$ moves lower when surface runoff with a lower $[Cl]_S$ dominates at initial stages of precipitation events.

The $[Cl]_D$ generated by dynamic EMMA methods and RT-Flux-PIHM model converge to each other (figure 4-5C). Comparing the $[Cl]_D$ from dEMMA, RT-Flux-PIHM model and data we found two interesting facts. First, dEMMA predicted more sudden dips in $[Cl]_D$ than RT-Flux-PIHM did when surface runoff dominates. Because $[Cl]_D$ changes instantly in dEMMA when contributions of different source waters are varied. In reality, transition of source water in the stream takes time and happens in different segments of the stream at different time. The final effect of such transition at the stream outlet is often smoothened. A brief dominance of surface runoff will not necessarily lead to a strong $[Cl]_D$ dip as indicated by EMMA method.

Secondly dEMMA completely missed the concentration spike in data in November. The $[Cl]_D$ in dEMMA was close to $[Cl]_L$ at that time as the stream was dominated by the subsurface

flow. The data also shows that the $[Cl]_D$ at this time is higher than that of any end-member, indicating dEMMA is not able to resolve $[Cl]_D$ spike no matter which end-member dominates. However, RT-Flux-PIHM model captured this spike albeit with a delay compared to data. The November "flushing spike" is in fact the result of the release of the trapped chloride by sudden improvement of hydrological connectivity. Upslope soil water will contribute to stream substantially when hydrological connectivity suddenly improves. If $[Cl]_L$ in upslope subsurface water is very different to the $[Cl]_L$ in the well connected riparian, and swale subsurface water, such a contribution will change $[Cl]_D$ significantly. In this work, upslope soil [Cl] has increased significantly during the summer. Therefore, when watershed hydrological connectivity increased and upslope area becomes more saturated, the higher concentration upslope subsurface water will be flushed into the stream to form a "flushing spike". Such a transition of stream source water has also been discussed elsewhere (McGuire and McDonnell, 2010).

Since the dynamic EMMA method used here does not include such a source water transition, the "flushing spike" is not modeled. Additional end-member, such as an upslope soil water end-member could be included in EMMA method. However, the contribution and composition of this end-member remain highly uncertain to quantify.

Watershed Box Model

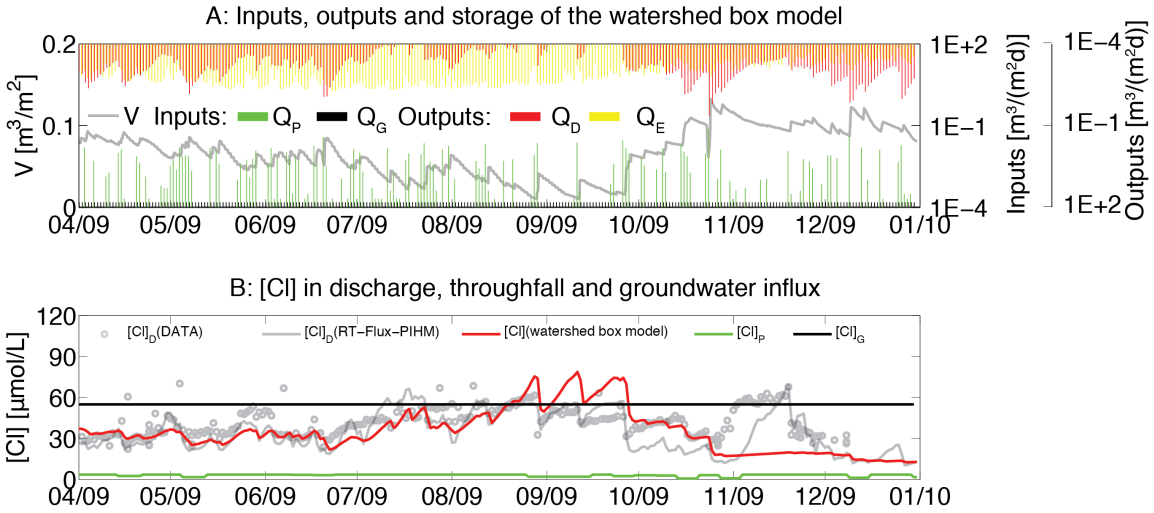

Figure 4-6 A: Inputs, outputs and storage of watershed in the watershed box model. The inputs include precipitation Q_P [$m^3/(m^2d)$] and deeper groundwater influx Q_G [$m^3/(m^2d)$]. The outputs include stream discharge Q_D [$m^3/(m^2d)$] and evapotranspiration Q_E [$m^3/(m^2d)$]. The input and output fluxes are in logarithmic scale. The storage of linear reservoir h [m^3/m^2] (grey curve) drops in summer due to elevated evapotranspiration. B: The stream discharge $[Cl]_D$ in data and calculated based on RT-Flux-PIHM, and based on watershed box model, together with chloride concentrations in different flows.

In the watershed box model, both the storage of water and the chloride concentration are solved numerically. Figure 4-6A shows that the storage of water decreased from April to late September, mainly due to an increase in evapotranspiration. High discharge always follows precipitation event, however, stream discharges tend to last longer. Evapotranspiration is at its highest in the summer months. The deeper groundwater influx is assumed to be always constant.

The [Cl] varies as a result of these input and output flows and evolution of the water storage. Compared to data and the $[Cl]_D$ modeled by RT-Flux-PIHM, the watershed box model overestimated stream [Cl] in the summer and underestimated [Cl] during the "flushing spike". The RT-Flux-PIHM showed lower $[Cl]_D$ in summer because the stream in summer is only draining soil water from valley floors and swales, which have a lower soil chloride concentration (Figure 4-3D). In this watershed box model, however, the stream is draining water from the

simple linear reservoir that have a uniformly elevated chloride concentration. For the same reason, the watershed box model is not able to reproduce the flushing spike that is originated from the sudden increase in upslope soil subsurface flow which brings higher chloride concentration soil water to the stream.

3.3 Hydrological Connectivity and $[Cl]_D$-Q_D relationship

It has been demonstrated that the stream in SSHCZO is draining from different drainage areas at different seasons or during different stages of a particular rainfall events. In this section, we will discuss the $[Cl]_D$-Q_D relationship trends under high (I_{CS}>10m) and low (I_{CS}≤10m) watershed hydrological connectivity phases.

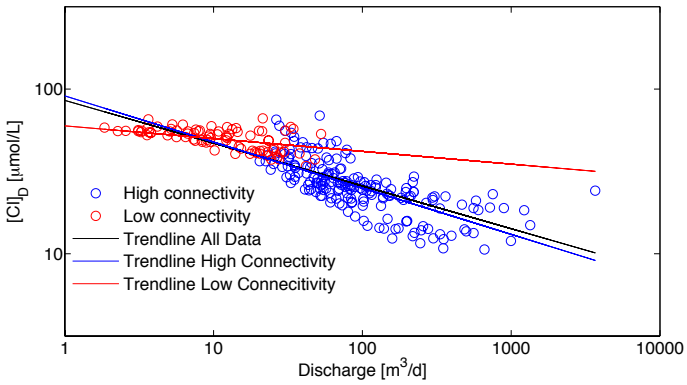

Figure 4-7 $[Cl]_D$-Q_D relationship under high (I_{CS}>10m, blue circles) and low (I_{CS}≤10m, red circles) watershed hydrological connectivity. Simple linear regression statistics are performed for all data points, the high connectivity periods and low connectivity periods.

We found that the $[Cl]_D$-Q_D slope a is -0.26 for all data, -0.28 for high connectivity periods and -0.07 for low connectivity phases. The $[Cl]_D$-Q_D slope for low connectivity periods is flatter because deeper groundwater influx dominates stream flow in those phases, which has a constant concentration. During high connectivity phases, higher precipitation leads to expansion of the saturation zones, induces higher level of transient subsurface flow, which effectively

enhance the mixing of soil water in the entire watershed. Precipitation also introduces low concentration end-members into the stream water mixture. Therefore, concentration is lowered at high discharge and thus the $[Cl]_D$-Q_D is showing a near-dilution behavior.

4. Sensitivity Analysis

4.1 Soil Porosity

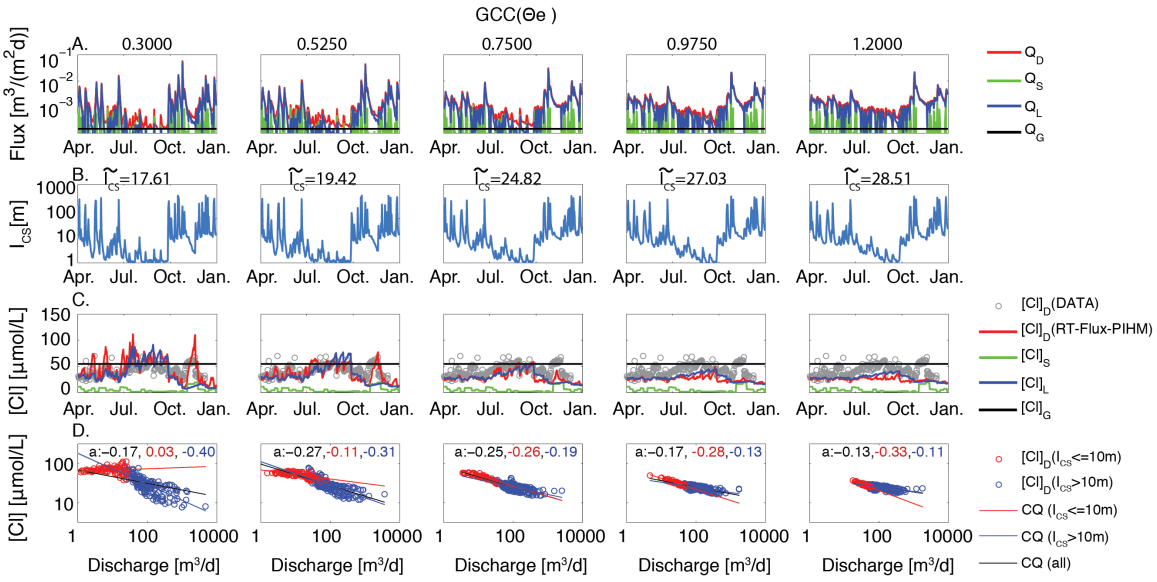

Figure 4-8 Under five different effective porosity conditions, the actual porosity in the field is equal to the GCC multiplies the base case soil porosity distribution, A: contributions of different flows to the stream; B: temporal evolution of l_{CS} [m] in logarithmic scale, evaluated based on hydrological connectivity function using the base case 75 percentile lateral subsurface flow as thresholds (0.18 m/d), the median of l_{CS} is also reported on plot; C: temporal evolution of $[Cl]_D$ (data and RT-Flux-PIHM simulation), $[Cl]_S$, $[Cl]_L$ and $[Cl]_G$; D: log-log plot of $[Cl]_D$-Q_D relationships, slopes *a* for simple linear regressions of each trendline (black for all data, red for low connectivity phase and blue for high connectivity phase) are also reported on plots.

As we increase the effective porosity in SSHCZO, surface runoff increased slightly while subsurface flow increased substantially, especially in the summer (figure 4-8A). The groundwater influx rate is the same as the base case (GCC=0.5, Figure 4-3). Less fluctuation in Q_L is also

observed. This is because during rainfall events, the water head in saturated zone will increase more in a low porosity soil for the same amount of precipitation, which will drives larger lateral subsurface flow. The mean I_{CS} in the summer also improves from 15.51 m (Jun.1st to Sept. 30th) in the low porosity case to 21.70 m in the high porosity case (figure 4-8B). This means the watershed is better at retaining water during summer in high porosity conditions. .

The variations in the $[Cl]_D$ could be interpreted in an EMMA framework (figure 4-8C). For the source waters, the $[Cl]_S$ and $[Cl]_G$ (green and black curves) for all cases are the same as the base case (figure 4-3). In the subsurface, however, chloride concentration in the summer is controlled by the porosity. The $[Cl]_L$ in summer (blue curve) is higher for low porosity case than in the high porosity cases. This is because lower porosity leads to less water storage. In summer, concentration will increase more due to evapotranspiration when water storage is less.

As a mixture of the source waters, the $[Cl]_D$ generally follows the concentration of the dominant source water. For lower porosity cases [GCC(Θ_e)<=0.7500, corresponding to a field mean effective porosity of 0.30 m^3/m^3], stream water is mostly dominated by deeper groundwater influx in the summer and by subsurface flow for the rest of times. Therefore $[Cl]_D$ is close to $[Cl]_G$ in summer and close to $[Cl]_L$ in the rest of times (except for GCC(Θ_e)=0.3000 case). Occasionally, stream water is receiving a large contribution from surface runoff, which leads to sudden drops in $[Cl]_D$. For higher porosity cases, subsurface flow is almost prevalent in the entire year. Therefore, the $[Cl]_D$ closely track $[Cl]_L$.

We also observed that occasionally $[Cl]_D$ will exceed the concentration of all three end-members (figure 4-8C), resulted from "flushing events". We see the more flushing spikes in lower porosity cases. In higher porosity cases, such spikes disappear. For flushing spike to form, it requires 1) the existence of upslope subsurface water with much higher $[Cl]_L$, which is the result of low hydrological connectivity in the watershed; and 2) sudden improvement in hydrological connectivity. Lower porosity cases are prone to have sudden improvement in

hydrological connectivity (figure 4-8B). For the lowest porosity case, post-summer hydrological connectivity improved as early as late September while the highest porosity case did not see a significantly improvement until mid-October. This is because saturation can expands to much larger area for the same amount of precipitation if we have lower porosity. For higher porosity cases, the expansion in saturated zone, and the improvement in hydrological conductivity, is much more gradual. In sum, higher porosity also leads to a reduction in flushing spike events.

For the $[Cl]_D$-Q_D relationships, we separate data points into two phases as in the previous discussion: a high connectivity phase (I_{CS} > 10m) where subsurface flow is dominant and a low connectivity phase (I_{CS} <= 10m) where deeper groundwater influx is dominant. Linear regressions for all data and the two regimes are also plotted in figure 4-8D. As we move to the higher porosity cases, the slope for the high connectivity phase becomes flatter, as higher porosity mitigates the concentration variations caused by either evapotranspiration or sudden upslope subsurface runoff. The slope for the low connectivity phase decreases with increasing porosity, suggesting stronger dilution in high porosity cases. Furthermore, we found that the slope of the high connectivity phase is a linear function of the median I_{CS}, with a coefficient of determination of 0.98. Larger hydrological connectivity in highly porous watershed contributes to the chemostatic behavior of chloride in stream water.

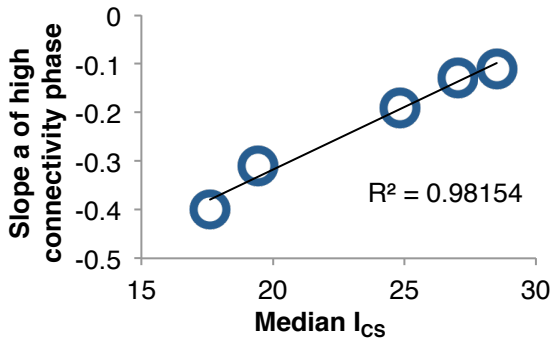

Figure 4-9 Slopes a for high connectivity phases in different porosity conditions are linearly correlated to the median I_{CS}.

In this SA, we found that a distribution of soil porosity ranging from 0.29~0.60 in SSHCZO is able to produce a near chemostatic $[Cl]_D$-Q_D relationship (a=-0.17~-0.13). Such a porosity range falls in the higher ends of typical soil porosity distributions in catchments. E.g., Reported soil porosity in several catchments ranges from 0.15~0.66 (the Institute of Hydrology Gwy Experimental Catchment, Plynlimon, mid-Wales: 0.15~0.60, Tuscon: 0.33~0.66, Hafren catchment, Wales: 0.35~0.55) (Beven and Binley, 1992; Chen et al., 2002; Gupta et al., 1999). No extra large hydrological water storage is required to produce such a near-chemostatic behavior in chloride. However, more chemostatic $[Cl]_D$-Q_D relationship (a>-0.13) could not be obtained unless extra large porosity is assumed, or other non-conservative processes are considered, as noted by (Chen et al., 2002). Lower soil porosity will lead to steeper $[Cl]_D$-Q_D relationship.

4.2 Soil Van Genuchten Parameter β

The Van Genuchten equation, implemented in RT-Flux-PIHM for recharge calculations, describes the ability of soil to retain water in the unsaturated zone (Van Genuchten, 1980):

$$\Theta = \Theta_r + \frac{(\Theta_e - \Theta_r)}{[1+(\alpha h)^{\beta}]^{(1-1/\beta)}} \quad (12$$

where Θ is the soil water content in unsaturated zone [m^3/m^3]; Θ_r and Θ_e is the residual soil water content and saturated water content, or effective porosity [m^3/m^3]; h is the pressure head [m]; both α [m^{-1}] and β [-] are fitting parameters. Both α and β are larger for coarser materials like silt, sand and smaller for clayish materials. Smaller α and β means the soil is more able to retain water and leads to smaller relative hydraulic conductivity in unsaturated zone. Therefore recharge from the unsaturated zone to the saturated zone will be slow. Larger α and β means the soil will not retain water as effectively and also permits a higher hydraulic conductivity

in the unsaturated zone (Van Genuchten, 1980). Therefore recharge from the unsaturated zone to the saturated zone will be quick. Although we tested the sensitivity of $[Cl]_D$-Q_D on both soil Van Genuchten parameter α and β, we found effects of varying α on $[Cl]_D$-Q_D is much smaller than that of varying β. In this section, we will focus on the effects of varying β.

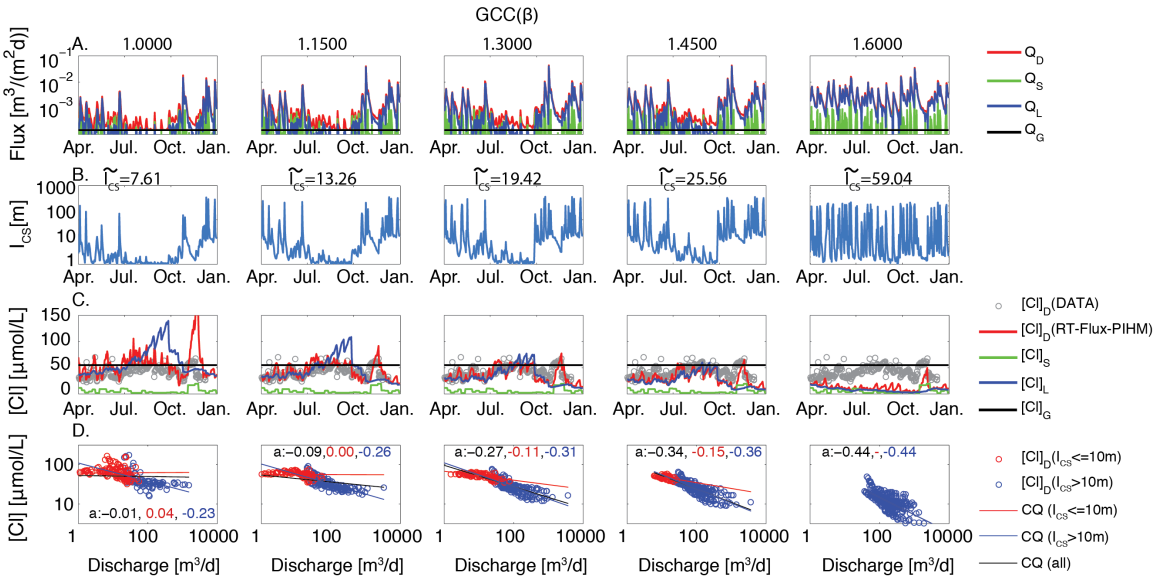

Figure 4-10 Same as figure 4-8, but under different soil Van Genuchten β conditions manipulated by varying GCC for β.

In figure 4-10A, as we increase β, surface runoff increased slightly but subsurface flow increased substantially. This is because as β increases, water retained in the unsaturated zone will become less, and more water will enter the saturated zone, which drives lateral subsurface flow. Also, lower β creates a higher pressure head difference between surface water and subsurface unsaturated zone, therefore directing more surface water into infiltration, reducing surface runoff.

For lower β cases, as more soil water are tightly bounded to the unsaturated zone, lateral subsurface flow that emerges from saturated zone will be limited. Therefore we observe a very limited hydrological connectivity in watershed (figure 4-10B). As we increase β, subsurface flow becomes more prevalent and the hydrological connectivity is also improved. In the highest β case,

water flows quickly downward into saturated zone before they evaporate. Therefore I_{CS} is large even in summer months.

In figure 4-10C, the $[Cl]_L$ in summer (blue curve) is higher for low β case than in the high β cases. This is the result from a longer residence time of subsurface water and more evapotranspiration in the unsaturated zone. The $[Cl]_D$ generally follows the concentration of the dominant source water. However, we also observe many flushing spikes where $[Cl]_D$ exceeds concentrations of all three end-member, especially for lower β cases. For the highest β case, rainfall quickly infiltrates and recharges to saturated zone, therefore, the $[Cl]_L$, $[Cl]_D$ are all close to $[Cl]_S$.

The $[Cl]_D$-Q_D of low β cases indicates a strong divide between low and high hydrological connectivity controlled phases (figure 4-10D). As we increase β, slopes for $[Cl]_D$-Q_D trend lines of the two phases are closer and the low connectivity phase eventually disappeared in highest β case. However, the slope for high connectivity phase is negatively correlated to the median I_{CS}. suggesting that higher β will promote a dilution behavior in $[Cl]_D$-Q_D.

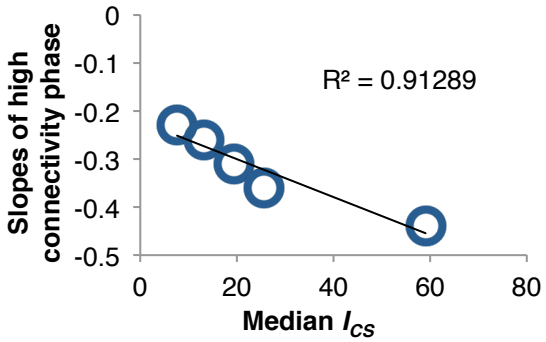

Figure 4-11 Slopes a for high connectivity phases in different β conditions are linearly correlated to the median I_{CS}.

4.3 Macropore Conductivity K_{mac}

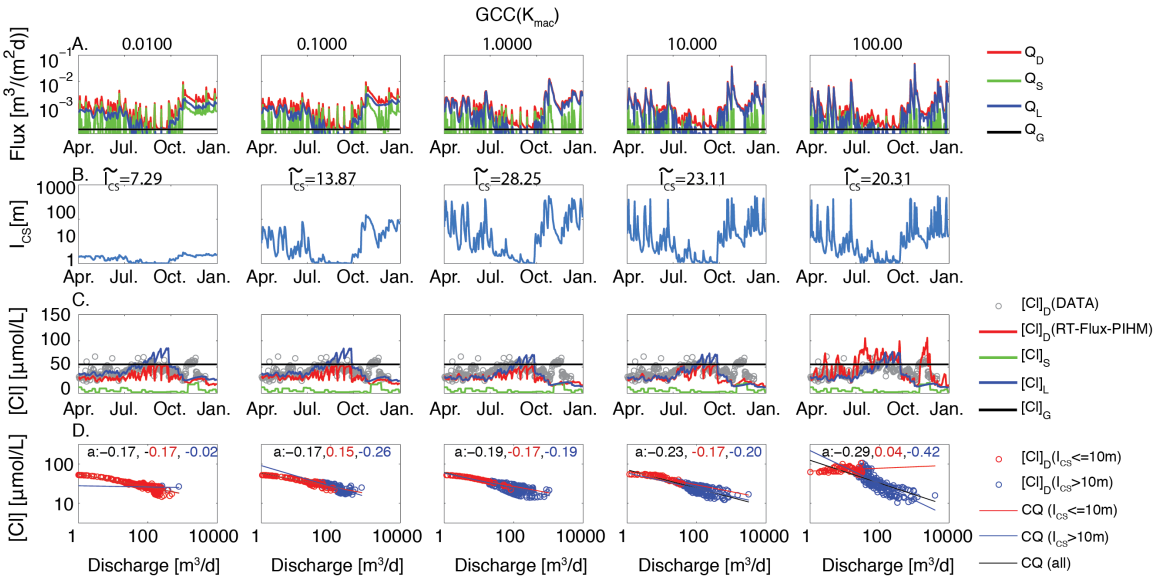

Figure 4-12 Same as figure 4-8, but under different soil K_{mac} conditions.

Macropore conductivity controls how quickly the watershed discharges the incoming rainwater from high precipitation events in the subsurface. Under low K_{mac} conditions, the subsurface flow is smaller but last longer, which also affect surface runoff. Since discharging of subsurface water after rainfalls is slow, precipitation afterwards will be directly to surface runoff. Under high K_{mac} conditions, both surface runoff and subsurface flow becomes quick pulses (figure 4-12A).

In the lowest K_{mac} case, the subsurface flow is slower than 0.18 m/d that in the entire simulation in the watershed, which is the threshold of hydrological connectivity (based on the 75 percentile of lateral subsurface flow of base case). Therefore, the I_{CS} is always very low (figure 4-12B). As we increase K_{mac}, I_{CS} also increases. However, further increase of K_{mac} leads to more transient changes in I_{CS} and actually lowers the median I_{CS}.

Although the hydrological dynamics are sensitive to changes in K_{mac}, it appears that varying K_{mac} by five orders of magnitude changed little in the $[Cl]_L$ and $[Cl]_D$ (figure 4-10C). The

$[Cl]_L$ is slightly higher in summer in lowest K_{mac} case, due to longer traveling time of water. "Flushing spikes" are only observed when larger K_{mac} is used. The slope of $[Cl]_D$-Q_D becomes steeper as K_{mac} increases.

4.4 Precipitation

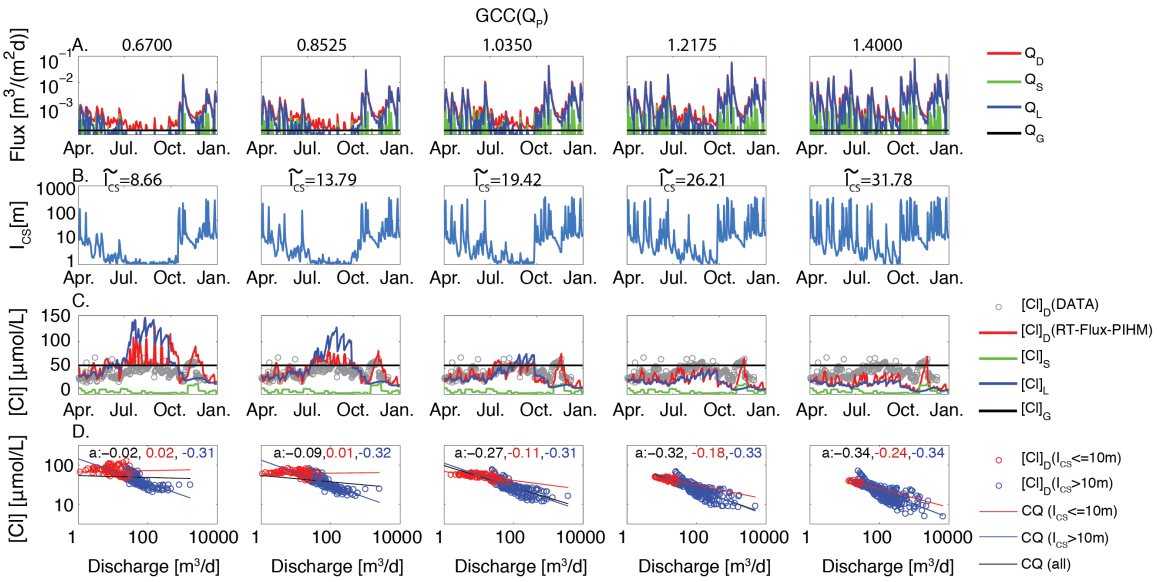

Figure 4-13 Same as figure 4-8, but under different precipitation conditions

In figure 4-13A, both surface runoff and subsurface increased substantially as precipitation increased. Therefore, discharge also increased. Figure 4-13B shows that the I_{CS} improves with higher precipitation, suggesting a better connected watershed with shorter low connectivity phase. For the lowest Q_P case, the watershed started to enter low hydrological connectivity phase as early as April.

The $[Cl]_L$ in summer (blue curve) is higher for low Q_P case than in the high Q_P cases. This is because of less precipitation to replace old water. This also leads to a much higher $[Cl]_D$ in summer when subsurface flow contributes to the stream. Both $[Cl]_L$ and $[Cl]_D$ decreases for larger precipitation cases as subsurface flow becomes the dominant source water.

The two regimes of $[Cl]_D$-Q_D discussed in the low porosity cases also appear in the low Q_P case, suggesting $[Cl]_D$-Q_D of the system is behaving very differently as different level of hydrological connectivity controls the field. As we increase precipitation, $[Cl]_D$-Q_D trend lines of the two phases also merge into one trend. However, the slope for $[Cl]_D$-Q_D is steeper in high Q_P condition, as more surface runoff and subsurface flow with lower [Cl] contributes to the stream, leading to a dilution behavior.

5. Conclusion

In the discussions above, we found that $[Cl]_D$ variations could be attributed to transitions between source waters. Such transitions could be event-based, seasonal or dependent on hydrological connectivity. During each precipitation events, $[Cl]_D$ is first lowered to $[Cl]_S$ level and then gradually increases back to the level of $[Cl]_L$ or $[Cl]_G$, which reflects a transition in source water as different flow types dominates stream flow progressively. In summer months, the subsurface $[Cl]_L$ increases as evapotranspiration elevates, which will be reflected in the stream water when surface flow contributes to stream. Hydrological connectivity may increase as the watershed responds to big precipitations, which leads to "flushing spikes" where outsized upslope subsurface flow contributing to stream that alters $[Cl]_D$.

The $[Cl]_D$ is generally close to subsurface $[Cl]_L$ if the watershed is well connected in the subsurface (e.g. during spring and winter). However, two major forces that can significantly drive up $[Cl]_D$. Summer evapotranspiration will elevate subsurface $[Cl]_L$, which will be reflected in stream water. The second is "flushing spikes" which requires 1) the existence of upslope subsurface water with much higher $[Cl]_L$ and 2) sudden improvement in hydrological connectivity. In addition, excessive surface runoff will lead to a dilutive stream water $[Cl]_D$-Q_D.

Therefore, the chemostasis of $[Cl]_D$-Q_D requires the watershed characteristics that is able to mitigate those driving forces. In our analysis, larger water storage (in this work, by increase porosity) is capable of mitigating such driving forces and will lead to more chemostatic $[Cl]_D$-Q_D. However, higher soil Van Genuchten parameter β (more sandy, silty soil, well-drained soil), larger macro pore conductivity or larger precipitation level will lead to more active surface/ subsurface flow and stronger dilution behavior in $[Cl]_D$-Q_D. In additional, if the hydrological connectivity is limited in the watershed, $[Cl]_D$-Q_D may be governed by two phases: a low connectivity phase where $[Cl]_D$ is mainly dictated by deeper groundwater influx and a high connectivity phase where $[Cl]_D$ reflects more mixing of subsurface and surface water end-member. In sum, although chloride is often suggested as a chemostatic tracer in watersheds, we found such chemostasis is not guaranteed. Nonetheless, the behaviors of chloride $[Cl]_D$-Q_D are strong indicators of the local watersheds characteristic.

We also found that EMMA framework could explain some of the variance we observed in stream water chloride concentration evolution, if accurate end member contribution at each moment could be obtained (e.g. in this work from detailed simulation with RT-Flux-PIHM). Therefore, EMMA method could be used as a convenient proxy model to understand the complex coupled hydrological mass transfer problem at watershed scale. However, the EMMA method does not explain flushing spikes unless additional upslope end-member is introduced.

Chapter 5

Summary

In this dissertation, the governing equations, numerical methods and algorithms for a system that couples flow dynamic, mass transfer and geochemical reaction is discussed. The development of RT-Flux-PIHM presents an integrated approach to study this complex system, e.g. to understand and quantify the hydrologic controls on water chemistry and geochemical reactions, and to explain the spatiotemporal variation in watershed water chemistry. RT-Flux-PIHM further extends the capability of hydrological and land surface model Flux-PIHM by adding a reactive transport module that enables explicit modeling of mass transfer and geochemical reactions, including mineral dissolution, precipitation, and ion exchange. RT-Flux-PIHM is the first model that provides such process integrations at watershed scale.

The model is evaluated at SSHCZO, based on field surveys and previous modeling efforts. The non-reactive transport of chloride is first analyzed using this model. For the chloride, its stream water concentration is controlled by inputs from rain and the hydrological connectivity of watershed. The well-connected watershed in the wet season allows fast flushing and less chloride storage in the watershed. In contrast, the less connected watershed in the summer allows more Cl storage; however, in the dry times, the catchment also allows only low flow from a relatively small connected area. Large rainfall events connect the whole watershed and wash out these “old water” pockets of high Cl concentrations – however, by the time the water emits at the stream mouth it is dilutes significantly. This seasonal change in hydrological connectivity at the watershed scale essentially regulates the chloride concentration and maintains its chemostatic behavior.

The reactive transport of magnesium is also studied in this dissertation. The data for the reactive species Mg were reproduced by tuning specific surface area of clay minerals, cation

exchange capacity, and groundwater influx rate. Magnesium concentrations are regulated by the interplay between clay dissolution and groundwater influx as sources and discharge as sink while ion exchange acts as the storage buffer. Faster clay dissolution in the wet season with more abundant water is accompanied by more diluted groundwater influxes to the stream at the mouth by more discharge. In the dry summer, the slower clay dissolution is accompanied by less diluted groundwater influxes at the stream mouth and lower discharge. Cation exchange buffers the magnesium concentration by storing an order-of-magnitude higher magnesium on exchange sites than in pore water and therefore serving as a large Mg pool. Large rainfall events flush out significant amount of stored Mg on the exchange sites while also diluting the waters, leading to similar Mg concentrations in the stream waters in large and small rainfall events. The interplay between these processes evens out seasonal differences and results in the chemostatic behavior of magnesium. In general, the multiple processes work together to generate the relatively chemostatic behavior for both solutes.

We found that chloride concentration in stream outlet ($[Cl]_D$) variations are attributed to transitions between source waters. Such transitions are event-based, seasonal or dependent on hydrological connectivity. Using dEMMA method, we found that during each precipitation events, $[Cl]_D$ is first lowered to $[Cl]_S$ level and then gradually increases back to the level of [Cl] or $[Cl]_G$, which reflects a transition in source water as different flow types dominates stream flow progressively (Evans and Davies, 1998). In summer months, the subsurface [Cl] increases as evapotranspiration elevates, which is then reflected in the stream water when surface flow contributes to stream. More comprehensive RT-Flux-PIHM model shows that hydrological connectivity increases as the watershed responds to big precipitations, which leads to “flushing spikes” where outsized upslope subsurface flow contributing to stream that alters $[Cl]_D$.

Numerical sensitivity tests on RT-Flux-PIHM model of SSHCZO show that certain watershed characteristics is capable of mitigating those transitions, including larger porosity, smaller precipitation level and soil Van Genuchten parameter β, which lead to more chemostatic $[Cl]_D$-Q_D. Larger watershed porosity will increase the water storage in place and improve hydrological connectivity even during the dry seasons, therefore reduces the variations in $[Cl]_D$. Larger precipitation level and higher soil Van Genuchten parameter β (more sandy, silty soil, e.g.) will lead to more active surface/ subsurface flow and stronger dilution behavior in $[Cl]_D$-Q_D. In sum, although chloride is often suggested as a chemostatic tracer in watersheds, we found such chemostasis is not guaranteed and dependent on watershed characteristics.

We also found that EMMA framework could explain most of the variance we observed in stream water chloride concentration evolution, if accurate end member contribution at each moment could be obtained. Therefore, EMMA method could be used as a convenient proxy model to understand the complex coupled hydrological mass transfer problem at watershed scale. However, the EMMA method does not explain flushing spikes unless additional upslope end-member is introduced, which leads to an underestimation of chloride concentration in such events compared to data and RT-Flux-PIHM simulation.

In conclusion, although the importance of individual processes has been discussed in the literature (Clow and Mast, 2010; Godsey et al., 2009; Herndon et al., 2015; Jencso et al., 2009; Jin et al., 2011a; Maher and Chamberlain, 2014; McGuire and McDonnell, 2010), the lack of process integration prevented a unified understanding on the controls of stream water solute concentrations and evaluation of the relative strength of these different controls. RT-Flux-PIHM offers process-based modeling that integrates different processes while at the same time can separate and interrogate the importance of each mechanism. In addition, the ability in RT-Flux-PIHM to resolve the spatial distributions of solute concentrations allow researchers to investigate the effects of topographic, hydrological and geochemical heterogeneities on solute reactive

transport, as demonstrated in this work. As such, it holds the potential of resolving long-standing puzzles in understanding watershed processes by integrating complex hydrogeochemical processes and identifying key controls under a variety of topological, hydrological, and geochemical conditions.

Chapter 6
Future Research

In the last few years, the interactions between hydrological and geochemical processes at watershed scale, and the impact of this interaction on mass transfer, mineral weathering and concentration discharge relationship (CQ) have received much attention. Based on our work, I suggest four interesting directions for future works.

First, hydrological connectivity strongly limit and regulates the mass transfer within watershed. It is collectively controlled by soil properties, magnitude of precipitation and watershed topography. We studied the chloride concentration discharge relationship in a small, first order, V-shaped watershed SSHCZO. An important task is to study how other watershed topography and characteristics affect the mass transfer and resulted concentration discharge relationships. E.g. is hydrological connectivity still relevant in controlling solute CQ for a much larger watershed?

Second, within SSHCZO, minerals are less depleted in regolith on the north side compared to the south side, while more soil organic carbon (SOC) is accumulated in the north side than the south side. It has been hypothesized that water subsurface flow is the strongest control on element depletion. And we did see more frequent subsurface flow in the south side compared to the north side in 2009. However, as only short term (1~2 year) simulations are conducted for SSHCZO, we failed to identify significant difference in mass accumulation or depletion between the two slopes in our simulation results. It is likely the differences in depletion or SOC accumulation occurred during a much longer time scale. To investigate this hypothesis, further optimization and acceleration is needed for RT-Flux-PIHM to conduct simulations on the 10^2~10^3 year time scales.

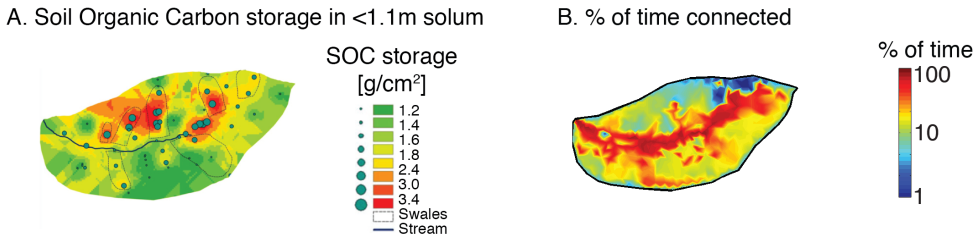

Figure 5-1 Spatial patterns of soil organic carbon storage (A) and the frequency of being hydrological connected (B). A is adapted from (Andrews et al., 2011)

Third, groundwater influx is found to be very important source water to stream in this work. However, it is simplified as a source both constant in flux and in solute concentrations in our discussions. Groundwater can penetrate into shallow water systems through fractures. Accurate quantification of deeper groundwater contribution in the field and the capability for numerical hydrological simulators to model this fractured groundwater flow are highly desirable.

Fourth, the effective surface areas for mineral kinetic reactions in the unsaturated zone in this work are assumed to depend on saturation. However, both experimental work and smaller scale (pore scale, column scale) simulations are required to further investigate the controlling mechanisms of mineral dissolution in unsaturated flowing aqueous phase/ multiphase flow. It is still unclear how localized heterogeneities in physical and chemical properties will affect this process, as well as how to upscale smaller scale understandings to larger scale applications.

Appendix A

User Manual of RT-Flux-PIHM

1. Introduction to the input files of RT-Flux-PIHM

RT-Flux-PIHM relies on a text file based user interface. Multiple input files are required by RT-Flux-PIHM to set up the heterogeneous distribution of physical and chemical properties in the simulation domain. An overview of the input files can be found in the following figure:

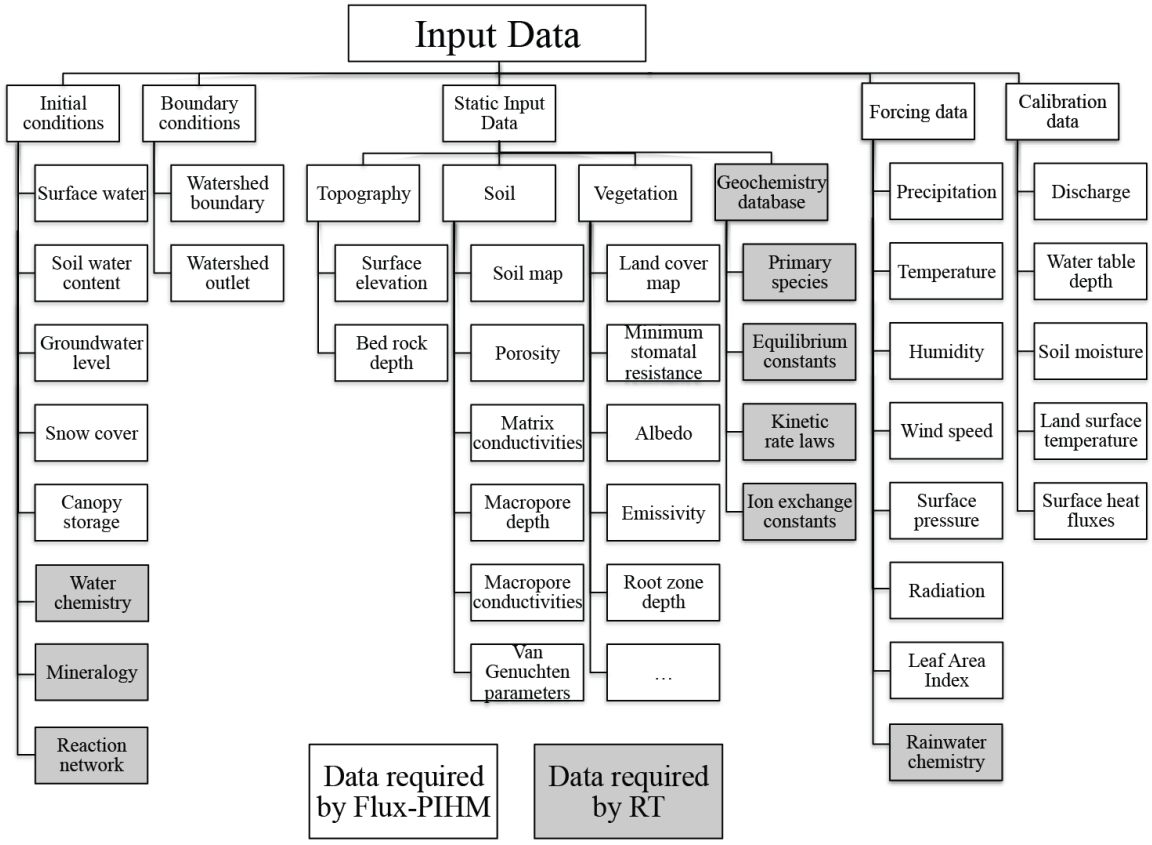

Figure A-1 Input files required by the Flux-PIHM component and the RT component, respectively.

2. Input File Format

Table A-1 Input files for RT component

projectName.txt	Specifying the project name
*.chem	Specifying the initial chemical condition and solving techniques
*.cdbs	The geochemical database
*.cini	Specifying the distribution of the initial geochemical condition in the field
*.prep	The time series of the rainwater solute concentration

2.1 projectName.txt

This file is used to indicate the name of the project. All the input files for this project should have the same filename but with different suffix. For input files for Flux-PIHM, please refer to the Flux-PIHM input file format document.

2.2 *.chem

The asteroid here is the project name specified in projectName.txt. The structure of the chemical condition file "*.chem" is very similar to the input file of the reactive transport code Crunchflow. Within the file, both "#" and "!" could be used to comment. It is recommended to use "#" to supply general comments on this text file interface and use "!" to comment out unwanted specifications. This file is divided into several blocks. Within each block, keywords are used to specify simulation options. Reserved block names are:

TITLE
RUNTIME
GLOBAL
INITIAL_CONDITIONS
OUTPUT
PUMP
Condition
PRECIPITATION
SECONDARY_SPECIES
MINERALS

TITLE

Title or general comments of the project, it will not be read by the RT simulator.

RUNTIME

A full list of RT runtime variables is listed in the following table:

Table A-2 Runtime variables in RT

Variables	Value Type	Value range	Remarks
tvd	Bool	True/false	Please refer to TVD section in code function part. Increase accuracy if enabled at the price of reducing speed.
output	Integer	>0	Frequency of chemical output, in hours
activity	Integer	0/1	If enabled (1), use activity model
act_coe_delay	Integer	0/1	If enabled (1), activity coefficient is not updated in every solving iteration
thermo	Integer	0/1	If enabled (1), RT simulator will use temperature data to compute chemical equilibrium and kinetics
relmin	Integer	0/1	If enabled (1), mineral volume fraction will be relative (to total mineral volume fraction)
effads	Integer	0/1	If enabled (1), RT simulator will use effective adsorption mode (MIM)
transport_only	Integer	0/1	If enabled (1), RT simulator will enter transport only mode. Reaction will be skipped.
precipitation	Integer	0/1/2	0: no precipitation concentration will be specified (0 solute concentration in precipitation assumed) 1: precipitation concentration will be specified in this file follow PRECIPITATION keyword 2: precipitation concentration will be specified in *.prep file as a time series
RT_delay	Integer	>0	Run RT simulator after certain days from the start of Flux-PIHM simulation.
Condensation	Double	>1	The concentration ratio between throughfall and rainwater, generally 1.0~5.0
AvgScl	Integer	>0	Average scaling factor, in minutes.

			Generally 0~30. If runtime error is encountered, reduce this number until no error is reported.

GLOBAL

A full list of global variables used in RT simulator is listed in the following table:

Table A-3 Global variables in RT

Variables	Value Type	Value range	Remarks
t_species	Integer	>0	Number of total primary species including minerals. An easy way to get this number to from the number of lines in each chemical condition block.
s_species	Integer	>0	Number of secondary species
minerals	Integer	>0	Number of minerals
adsorption	Integer	>0	Number of primary adsorption species
cation_exchange	Integer	>0	Number of primary cation exchange species
mineral_kinetic	Integer	>0	Number of kinetic mineral reactions
aqueous_kinetic	Integer	>0	Number of kinetic aqueous reactions
diffusion	Double	>0.0	Fixed diffusion coefficient, in cm^2/s
dispersion	Double	>0.0	Fixed dispersivity, in m.
cementation	Double	>0	Cementation factor
temperature	Double	>0	Field temperature in ^oC, voided if thermo option is enabled.

INITIAL_CONDITIONS

Chemical properties of soil and water are highly likely to be very heterogeneous. To account for this heterogeneity, we provide two ways to specify the spatial distribution of chemical conditions. The first method is to directly specify the chemical conditions for groups of finite elements in the field in this keyword block. The second method is to use *.cini file to specify chemical condition for every finite elements one by one. To use the first option, the users can use syntax like:

CONDITION_NAME 1-1070

This specification gives the chemical condition “CONDITION_NAME” to elements 1 to 1070.

CONDITION_NAME 1,2,3,4,5

This specification gives the chemical condition “CONDITION_NAME” to elements 1, 2, 3, 4 and 5.

Multiple conditions could be specified at once:

```
CONDITION_NAME1   1-1070
CONDITION_NAME2   500-600
CONDITION_NAME3   550-602
CONDITION_NAME4   703,704
```

This specification assign “CONDITION_NAME1” to elements 1 to 1070, and then assign “CONDITION_NAME2” to elements 500 to 600. Later assignments will overwrite previous assignments in this case. Each of the CONDITION_NAME appeared here should be defined in later sections of this input file using “Condition” keyword as a prefix.

To use the second option, the users should attach FILE keyword right after INITIAL_CONDITIONS keyword in this block and then specify the filename of the initial condition distribution. E.g:

```
INITIAL_CONDITIONS  FILE shp.cini
END
```

FILE keyword has a higher priority than direct specifications. If FILE keyword appears after INITIAL_CONDITIONS, the code will skip specification made in the first method. E.g.:

```
INITIAL_CONDITIONS  FILE shp.cini
CONDITION_NAME1   1-1070
CONDITION_NAME2   500-600
CONDITION_NAME3   550-602
CONDITION_NAME4   703,704
END
```

The code will read shp.cini regardless the specifications made within this block. Also note that the number of elements is doubled in RT compared to Flux-PIHM. Each Flux-PIHM element is further divided into the unsaturated zone element and the saturated zone element. Suppose there is Num_Ele elements in Flux-PIHM, there will be 2* Num_Ele elements in RT. The first Num_Ele elements are saturated zone elements and the Num_Ele+1 to 2* Num_Ele elements are unsaturated zone elements.

OUTPUT

This keyword is used to output chemical concentration time series in certain elements, followed by the total number of elements that the user wishes to see the concentration evolution. E.g.:

```
OUTPUT 3
1100
500
100
END
```

This specification will instruct the code to output chemical concentration time series for elements 1100, 500 and 100. The output file generated in this manner will be named *1100.btcv, *500.btcv, *100.btcv, respectively. The asteroid here is the project name.

PUMP

This keyword is used to specify the location and the injection rate of injecting wells/ groundwater influxes, followed by the total number of injection/ influx elements. For example:

```
PUMP  1
1109     Mg++      1000
END
```

Specifies a groundwater influx at element 1109 that will induce an inflow of Mg++ of 1000 mol/year. Note that substantially large injection rate relative to the soil water concentration will lead to non-convergence of code due to sudden jumps in the total concentration induced by injection.

Condition

This keyword is used to specify the details of the chemical conditions specified in INITIAL_CONDITIONS. Multiple total concentrations of primary species could be specified in a way that is very similar to CRUNCHFLOW. E.g.:

```
Condition MS
pH              4.48
```

```
HCO3-       8.0E-4
Mg++        7.05E-5
Cl-         3.12E-5
Na+         18.5E-6
H4SiO4      1.00E-8
K+          1.53E-5
shillite    0.2690   -ssa   0.08
shchlorite  0.0669   -ssa   0.01
Kaolinite   0.0283   -ssa   70.0
Quartz      0.6358   -ssa   70.0
FeOOH       1.00E-5  -ssa   70.0
>SOH        1.00E-5
END
```

For method to specify chemical concentration, please refer to CRUNCHFLOW's user manual.

SECONDARY_SPECIES

This block is used to specify the secondary species that the users would like to track. A complete list of the available secondary species resulted from the specified primary species could be generated via running a CRUNCHFLOW instance with the same primary species set using the database_sweep option.

MINERALS

The kinetic mineral reactions are specified here. This block follows a similar format as the corresponding block in CRUNCHFLOW input file.

PRECIPITATION

This block is used to specify a static rainwater composition.

2.3 *.cdbs

The chemical database file *.cdbs has the exactly same format as CRUNCHFLOW's database files. In fact, the users can use RT's database file and CRUNCHFLOW's database file interchangeably. For a complete description on the CRUNCHFLOW's database file, please refer to CRUNCHFLOW user's manual.

2.4 *.cini

The initial chemical condition file *.cini is used to specify the spatial distribution of chemical conditions in the field. This file is simply a full list of elements and the chemical condition they belong to.

File Structure:

Index	Condition index
Repeating *NumEle* times	

Description:

Variables	Value Type	Value range	Remarks
Index	Integer	>0	Index of element
Condition index	Integer	>0	Index of chemical conditions in *.chem
NumEle	Integer	>0	Number of elements in simulation

2.5 *.prep

RT simulator can utilize time series date in rainwater solute concentration. Users could use the syntax "precipitation 2" to enable this option.

File Structure:

Pconc	Num_Pconc	Num_Precipitation
Species_index	*Repeat Num_Pconc times*	
Time	Value	

Repeat *Num_Precipitation times*

Description:

Variables	Value Type	Value range	Remarks
Pconc	Keyword		Keyword indicate beginning of the file
Num_Pconc	Integer	>0	Number of species in rainwater
Num_Precipitation	Integer	>0	Number of rainwater concentration measurements
Time	Time string	time	
Value	Double	>0.0	Rainwater concentration of solutes, in M

3. Output File Format

Table A-4 Output files generated by RT

*.conc	Chemical concentration evolution in the field
*.btcv	Chemical concentration evolution in the outlet of stream
*index.btcv	Chemical concentration evolution in selected elements
*.vol	Later saturated zone flow velocity

3.1 *.conc

This file is the main output of RT simulator. It contains the concentration of all species in each element at specified output frequency (e.g. hourly, daily, etc.).

File Structure:

Time		
Cell	Species_Name	… *Num_Species*
Index	Concentration	… *Num_species*
Repeat 2**Num_Ele times*		

Time		
Cell	Species_Name	… *Num_Species*
Index	Concentration	… *Num_species*
Repeat 2**Num_Ele times*		

… Repeat Num_output times

Description:

Variables	Value Type	Value range	Remarks
Time	Time string	time	
Species_Name	String		Name of all the chemical species
Index	Integer	>0	Index of elements
Concentration	Double		Logarithm of concentration in M
Num_species	Integer	>0	Number of total species simulated
Num_Ele	Integer	>0	Number of Flux-PIHM elements
Num_output	Integer	>0	Total number of output data points

3.2 *.btcv and *index.btcv files

The breakthrough curve files are auxiliary output files that provide the concentration evolution at selected elements.

File Structure:

	Species_Name	… *Num_Species*
Time	Concentration	… *Num_species*
Repeat *Num_output times*		

Description:

Variables	Value Type	Value range	Remarks
Time	Time string	time	
Species_Name	String		Name of all the chemical species
Concentration	Double		Logarithm of concentration in M
Num_species	Integer	>0	Number of total species simulated
Num_output	Integer	>0	Total number of output data points

3.3 *.vol

This file contains the information on the velocity field in the watershed. Both the x component and the y component of the velocity vectors in each of the saturated zone elements are reported. In unsaturated zone, there is no lateral flow.

File Structure:

Time		
Velocity_x	… *Num_Ele*	
Velocity_y	… *Num_Ele*	
Repeat *Num_output times*		

Description:

Variables	Value Type	Value range	Remarks
Time	Time string	time	
Velocity_x	Double		X component of the velocity vector
Velocity_y	Double		Y component of the velocity vector
Num_Ele	Integer	>0	Number of Flux-PIHM elements

Appendix B

RT source code details

RT source codes includes four files:

Table B-1 RT component source code files

rt.h	Data structure and library for RT
rt.c	RT main code
os3d.c	Transport functions
react.c	Reaction functions

The functions of each file will be discussed in the following sections.

1. Data Structure and Library <rt.h>

This is the header file for the RT simulator. It contains the definition of the data structures used in other codes. We will introduce the data structures from a top-down perspective:

At the highest level, all the data are stored in a grand data structure that is called *chem_data_structure*. Within this data structure, runtime related and global variables are stored. These variables are generally specified in the beginning of the simulation and will stay constant throughout the simulation. These variables are used to control the simulator.

Since the simulation domain is discretized into hundreds of elements, the physical and chemical properties of each element are organized into a single class that is called *vol_conc_type* (volume/concentration data type). In this class, the volumetric properties such as bottom area, water height, porosity, saturation and temperature are stored, visited and updated in every time step. In general, RT simulator relies on Flux-PIHM to update these physical variables. Concentrations of chemical species are also stored here. In each time step, RT solves for the advection-diffusion-reaction equation and updates the concentrations accordingly.

RT uses a connection-based finite volume method to solve for the differential equations. A key component of this connection-based method is the definition of connection class *face_type*.

In *face_type* instance, the information on the upstream, downstream nodes is recorded. RT also stores some dynamic variables, such as the flow velocity in this data type.

For the chemical reaction calculation, each of the chemical species is realized by using a *species_type* data structure. Key chemical parameters such as the molar weight, charge, species names are stored in this data class. Additional data structure is also used to store the information on kinetic reactions (*Kinetic_reaction_structure*).

For details of the data structures, developers should refer to the source code and code comments. Most of the data types within data structures are quite self-explanatory or explained in the comments.

2. RT component main code <rt.c>

This is the source code for data exchange between RT and Flux-PIHM, as well as many controlling functions:

chem_alloc:

This is the function that allocation memory spaces for and initialize the chemical data structure, reading input files and look up chemical reaction network from the chemical database.

fluxtrans:

This function imports flow field information from Flux-PIHM at the end of every Flux-PIHM time step. The data be transferred include: surface flow, subsurface flow, water storage in the saturated and unsaturated zone, evapotranspiration, net precipitation, infiltration, recharge. This function also calls os3d for the advection diffusion dispersion calculation.

Monitor:

This function performs a mass balance check on the imported Flux-PIHM water distribution and flow rates.

PrintChem:

This function outputs the RT variables into output files at a predefined frequency.

AdptTime:

This function handles the adaptive time stepping in RT for the reaction step. Initially, the reaction time step is set to be equal to the time step of Flux-PIHM simulation. If a certain element failed to converge in the reaction step, time step will be reduced by a half until it converges.

3. Transport functions <os3d.c>

The source code os3d.c, as the name implies, utilizing the operator splitting (3D) method to solve for the mass transfer part of the advection diffusion equation (Steefel et al., 2014; Zysset et al., 1994). Such a separation in solving process is made possible by carefully controlling the time step (Jacques et al., 2006). This function also handles the additional source/ sink of chemical species.

4. Reaction Functions <react.c>

The react.c code contains mainly three functions: 1) *Lookup* function to help the code read the chemical database; 2) *Speciation* function to calculate the chemical equilibrium status from the given set of primary and secondary species and their corresponding total concentration; 3) *React* function that is responsible for calculation of kinetic reactions, which will be called at every RT-Flux-PIHM time step.

Lookup:

When the user specifies a chemical species in the input file, it usually only have two components: the name of the chemical species and the total concentration. It becomes the code's job to find out the right chemical parameters for this given chemical species. Therefore, the code

searches for the name of the chemical species in the appropriate section of the database file. *Lookup* function is designed for this purpose.

Speciation:

The speciation function is used to calculate the concentrations of individual species from the total concentrations and thermodynamic parameters. The calculation follows an iterative manner as detailed in section 3.8.

RT-Flux-PIHM currently supports two modes of speciation: 1) speciation from total concentrations and 2) speciation from total concentration and pH. The method of the first mode could be found in section 3.8. In the second mode, total concentrations for all the other species are given except for hydrogen. Instead of specifying the total concentration of hydrogen ion, pH is specified, which is actually the activity of hydrogen ion. This specification actually reduces the number of total unknowns in the system from N_c to N_c-1. Therefore, we are only required to solve for this system with N_c-1 total concentrations. Once this system is solved and the concentrations for all other primary species are obtained, we calculate back the total concentration of hydrogen ion and store it.

React:

In each time step, the reaction rate of the kinetic reaction is calculated based on TST rate law and the current concentration of all species. Based on this reaction rate, an increase in product concentration is derived so as a reduction in the reactant concentration. Note that the concentrations derived here is still total concentrations. After this step, the system use speciation method to determine the exact concentrations of primary and secondary species. With the new concentrations of all species, the kinetic reaction rate is calculated again. This process could also be conceptualized in such a way: in every incremental time step, kinetic reactions will only

generate total concentration for primary species. Then the primary species will automatically equilibrate with the secondary species.

Appendix C

Examples of RT-Flux-PIHM Input Files

In this section, we provide several examples of RT-Flux-PIHM inputs files that cover the non-reactive transport of chloride and the reactive transport of magnesium in SSHCZO. Only the main input files for RT (.chem) are included in this section (.prep file for Cl case as well, data retrieved from NADP (TDEP, 2015)). Since the other input files and the input files for the Flux-PIHM model are either very lengthy or contains large time series data that cannot be conveniently included here, they are uploaded to a GITHUB repository for free access. The address of this repository is:

https://github.com/architectds/RT_Flux_PIHM_input_files

To interpret the input files included here, please refer to the Appendix A or to the commenting lines starting with a # symbol. For helps on Flux-PIHM input files, please refer to Flux-PIHM input file manual, which could also be found in the above repository. The credit of the Flux-PIHM input file manual belongs to Yuning, Shi.

1. Chloride Non-Reactive Transport

shp.chem file:

```
##########################################################
# FILE       : PIHM_RT CHEM INPUT FILE EXAMPLE          #
# DEVELOPPER : Chen Bao (baochen.d.s@gmail.com          #
##########################################################

TITLE
shp
END

RUNTIME
# runtime variables
tvd       true
# whether to use tvd in calculation the advective concentration flux
output     24
```

```
# set output interval to # hours
activity   1
# enable the correction of activity using Debye-Huckel Equaion (1) or using no correction (0)
act_coe_delay 0
# define whether to delay the calculation of activity coefficients (0) for delay and (1) for no delay
thermo     0
# whether (1) or not (0) to couple the thermo modeling of pihm
relmin     1
# whether mineral volume fraction is relative (1) or absolute (0)
effads     0
# whether (1) or not (0) to use the effective adsorption model (MIM + ADSORPTION + RT)
transport_only  1
# whether (0) or not (1) to include the reactive calculation. 0 for turn on reactions and 1 for turn off. Suitable for stable tracer transport problem.
precipitation  2
# whether (1) or not (0) precipitation will be specified, 2 to specify Pconc by file *.prep.
RT_delay  2
Condensation    1.8
AvgScl    30
END

GLOBAL
t_species    4
# total species including 1) primary speices, 2) primary minerals, 3) primary adsorptions. The number of species that are put into the condition blocks
s_species    0
# the number of species that are put into the secondary_species block.
minerals     0
# the number of species that are minerals in the condition blocks.
adsorption   0
# the number of species that are primary surface complexation, note that secondary surface complexation goes to secondary species
cation_exchange 0
# the nubmer of species that are primary cation exchange
mineral_kinetic  0
# the number of mineral kinetic reactions
aqueous_kinetic  0
# the number of aqueous kinetic reactions
diffusion    1E-5
# fixed diffusion coefficient, in cm2/s
dispersion   0.10
# fixed dispersion coefficient, in m
cementation  1
# cementation factor
temperature  25
# assumed temperature for thermo decouple mode
END

INITIAL_CONDITIONS FILE shp.cini
RT      1-1070
# Assign the conditions to blocks, supported separators are "," and "-". Named condition need be specified using Condition keyword
MS      1071-1112
VF      1050
END

OUTPUT 1
1110
END

Condition RT
# concentrations and names of species of condition X.
# recommanded order: aqueous primary, adsorption, cation exchange, mineral
H2              0.016338445
O18             0.110175714
```

```
Cl-              3.69E-5
Na+          19.0E-6
END

Condition MS
H2           0.016338445
O18           0.110175714
Cl-          3.12E-5
Na+           18.5E-6
END

Condition VF
H2           0.018338445
O18           0.110175714
Cl-          3.93E-5
Na+           26.7E-6
END

PRECIPITATION
H2           0.015560424
O18           0.110175714
Cl-          1.93E-5
Na+           1.0E-5
END


SECONDARY_SPECIES
# Basis switching is not supported in this version of PIHM_RT
END

MINERALS
# rate constant log10(rate, units mol/m^2/s)
END
```

shp.prep file (solute concentration in precipitation, time series file)

From the left to the right starting from the second row of this file: date, time, concentration of H2, O18, Cl^-, Na^+.

```
Pconc     4    125
2006-11-26 00:00:00 0.01568 0.1097  1.211e-06   1.21E-6
2008-01-01 00:00:00 0.01568 0.1097  2.500e-06   2.50E-6
2008-01-15 00:00:00 0.01568 0.1097  2.98e-06   2.98E-6
2008-01-22 00:00:00 0.01568 0.1097  7.50e-06   7.50E-6
2008-01-29 00:00:00 0.01568 0.1097  2.92e-06   2.92E-6
2008-02-05 00:00:00 0.01568 0.1097  5.94e-06   5.94E-6
2008-02-12 00:00:00 0.01568 0.1097  14.16e-06   14.16E-6
2008-02-19 00:00:00 0.01568 0.1097  3.12e-06   3.12E-6
2008-02-25 00:00:00 0.01568 0.1097  8.05e-06   8.05E-6
2008-03-04 00:00:00 0.01568 0.1097  3.15e-06   3.15E-6
2008-03-11 00:00:00 0.01568 0.1097  8.59e-06   8.59E-6
2008-03-18 00:00:00 0.01568 0.1097  15.15e-06   15.15E-6
2008-03-25 00:00:00 0.01568 0.1097  1.50e-06   1.50E-6
2008-04-01 00:00:00 0.01568 0.1097  1.70e-06   1.70E-6
2008-04-08 00:00:00 0.01568 0.1097  6.50e-06   6.50E-6
2008-04-15 00:00:00 0.01568 0.1097  3.40e-06   3.40E-6
2008-04-22 00:00:00 0.01568 0.1097  4.535e-06   4.535E-6
2008-04-29 00:00:00 0.01568 0.1097  4.31e-06   4.31E-6
2008-05-06 00:00:00 0.01568 0.1097  1.32e-06   1.32E-6
2008-05-13 00:00:00 0.01568 0.1097  1.60e-06   1.60E-6
2008-05-20 00:00:00 0.01568 0.1097  2.22e-06   2.22E-6
2008-05-26 00:00:00 0.01568 0.1097  2.32e-06   2.32E-6
```

2008-06-03 00:00:00 0.01568 0.1097 2.50e-06 2.50E-6
2008-06-10 00:00:00 0.01568 0.1097 3.63e-06 3.634E-6
2008-06-17 00:00:00 0.01568 0.1097 4.84e-06 4.84E-6
2008-06-23 00:00:00 0.01568 0.1097 2.81e-06 2.81E-6
2008-07-01 00:00:00 0.01568 0.1097 1.74e-06 1.74E-6
2008-07-08 00:00:00 0.01568 0.1097 4.05e-06 4.05E-6
2008-07-15 00:00:00 0.01568 0.1097 4.70e-06 4.70E-6
2008-07-22 00:00:00 0.01568 0.1097 1.64e-06 1.64E-6
2008-07-28 00:00:00 0.01568 0.1097 8.17e-06 8.17E-6
2008-08-05 00:00:00 0.01568 0.1097 6.33e-06 6.33E-6
2008-08-12 00:00:00 0.01568 0.1097 4.33e-06 4.33E-6
2008-08-19 00:00:00 0.01568 0.1097 7.52e-06 7.52E-6
2008-08-26 00:00:00 0.01568 0.1097 4.222e-06 4.22E-6
2008-09-02 00:00:00 0.01568 0.1097 2.76e-06 2.76E-6
2008-09-09 00:00:00 0.01568 0.1097 1.38e-06 1.38E-6
2008-09-23 00:00:00 0.01568 0.1097 0.90e-06 0.90E-6
2008-09-30 00:00:00 0.01568 0.1097 7.69e-06 7.69E-6
2008-10-07 00:00:00 0.01568 0.1097 2.70e-06 2.70E-6
2008-10-14 00:00:00 0.01568 0.1097 11.41e-06 11.41E-6
2008-10-21 00:00:00 0.01568 0.1097 7.01e-06 7.01E-6
2008-10-28 00:00:00 0.01568 0.1097 2.64e-06 2.64E-6
2008-11-04 00:00:00 0.01568 0.1097 6.76e-06 6.76E-6
2008-11-11 00:00:00 0.01568 0.1097 4.73e-06 4.73E-6
2008-11-18 00:00:00 0.01568 0.1097 2.25e-06 2.25E-6
2008-11-25 00:00:00 0.01568 0.1097 1.211e-06 1.21E-6
2008-12-03 00:00:00 0.01582 0.1101 1.211e-06 1.21E-6
2008-12-12 00:00:00 0.01628 0.1103 3.070e-06 3.07E-6
2008-12-23 00:00:00 0.01677 0.1107 3.606e-06 3.60E-6
2008-12-31 00:00:00 0.01527 0.1095 1.814e-05 1.21E-6
2009-01-06 00:00:00 0.01527 0.1095 3.44E-6 1.35E-6
2009-01-13 00:00:00 0.01541 0.1098 1.72e-05 1.02E-5
2009-01-23 00:00:00 0.01469 0.1095 4.87E-6 2.52E-6
2009-02-03 00:00:00 0.01668 0.1107 4.873e-06 2.52E-6
2009-02-17 00:00:00 0.01666 0.1106 4.535e-06 3.09E-6
2009-02-24 00:00:00 0.0155 0.1097 1.52e-05 1.80E-5
2009-03-02 00:00:00 0.01658 0.1105 2.079e-05 2.15E-5
2009-03-10 00:00:00 0.01606 0.1101 6.338e-06 6.70E-6
2009-03-17 00:00:00 0.01673 0.1106 6.338e-06 6.70E-6
2009-04-07 00:00:00 0.0169 0.1108 3.831e-06 3.30E-6
2009-04-13 00:00:00 0.01709 0.1111 1.44e-06 0.957E-6
2009-04-21 00:00:00 0.01608 0.1103 2.51e-06 8.70E-7
2009-04-28 00:00:00 0.01704 0.1109 4.79e-06 3.87E-6
2009-05-04 00:00:00 0.01625 0.1105 9.578e-07 3.04E-7
2009-05-12 00:00:00 0.01707 0.111 5.100e-06 4.61E-6
2009-05-26 00:00:00 0.01675 0.1107 2.112e-06 1.22E-6
2009-06-02 00:00:00 0.01672 0.1107 3.352e-06 4.35E-7
2009-06-09 00:00:00 0.01722 0.1111 1.92E-6 6.52E-7
2009-06-16 00:00:00 0.01665 0.1106 1.80E-6 1.22E-6
2009-06-23 00:00:00 0.01637 0.1105 5.831e-06 1.87E-6
2009-06-30 00:00:00 0.01606 0.1102 5.408e-06 2.17E-6
2009-07-07 00:00:00 0.01671 0.1107 3.18e-06 6.26E-6
2009-07-14 00:00:00 0.01671 0.1107 1.0E-6 6.26E-6
2009-08-04 00:00:00 0.01699 0.111 3.52e-06 4.83E-6
2009-08-11 00:00:00 0.01689 0.1109 1.21e-06 2.61E-7
2009-08-18 00:00:00 0.01709 0.111 2.03e-06 1.48E-6
2009-08-25 00:00:00 0.01691 0.1108 1.155e-06 6.09E-7
2009-09-01 00:00:00 0.01615 0.1101 1.155e-06 6.09E-7
2009-09-08 00:00:00 0.01615 0.1101 1.15E-6 8.70E-7
2009-09-15 00:00:00 0.01615 0.1101 1.15E-6 4.13E-5
2009-09-22 00:00:00 0.01615 0.1101 1.38E-6 7.39E-7
2009-09-29 00:00:00 0.01615 0.1101 1.75E-6 10E-7
2009-10-06 00:00:00 0.01661 0.1105 1.633e-06 8.26E-7
2009-10-13 00:00:00 0.01558 0.1097 4.225e-07 8.70E-8
2009-10-20 00:00:00 0.01699 0.1108 1.803e-06 1.61E-6
2009-10-27 00:00:00 0.01604 0.1102 5.352e-07 2.17E-7

```
2009-11-03 00:00:00 0.01705 0.1108  9.268e-06   2.83E-6
2009-11-17 00:00:00 0.01692 0.1108  1.076e-05   9.22E-6
2009-11-24 00:00:00 0.01692 0.1108  3.66E-6     6.52E-7
2009-12-01 00:00:00 0.01465 0.1091  3.352e-06   2E-6
2009-12-08 00:00:00 0.01528 0.1096  7.324e-07   3.48E-7
2009-12-15 00:00:00 0.01358 0.1084  2.986e-06   1.83E-6
2009-12-22 00:00:00 0.01637 0.1105  4e-06       2.91E-6
2009-12-29 00:00:00 0.0152 0.1097  9.58E-7      8.70E-7
2010-01-05 00:00:00 0.0153 0.1097  5.32e-06       2E-6
2010-01-12 00:00:00 0.0153 0.1097  1.04e-06       2E-6
2010-01-19 00:00:00 0.01561 0.1102  5.20e-06       2E-6
2010-01-26 00:00:00 0.01678 0.1107  2e-06       2E-6
2010-02-02 00:00:00 0.0153 0.1097   1.63e-06       2E-6
2010-02-09 00:00:00 0.0153 0.1097  2.22e-06       2E-6
2010-02-23 00:00:00 0.0153 0.1097  5.60e-06       2E-6
2010-03-02 00:00:00 0.0153 0.1097  2.22e-06       2E-6
2010-03-09 00:00:00 0.0153 0.1097  1.88e-06       2E-6
2010-03-16 00:00:00 0.0153 0.1097  14.98e-06       2E-6
2010-03-23 00:00:00 0.0153 0.1097  7.26e-06       2E-6
2010-03-30 00:00:00 0.0153 0.1097  8.17e-06       2E-6
2010-04-06 00:00:00 0.0153 0.1097  2.22e-06       2E-6
2010-04-20 00:00:00 0.0153 0.1097  1.55e-06       2E-6
2010-04-27 00:00:00 0.0153 0.1097  1.72e-06       2E-6
2010-05-04 00:00:00 0.0153 0.1097  2.56e-06       2E-6
2010-05-11 00:00:00 0.0153 0.1097  3.80e-06       2E-6
2010-05-18 00:00:00 0.0153 0.1097  1.32e-06       2E-6
2010-05-25 00:00:00 0.0153 0.1097  7.0e-06       2E-6
2010-06-01 00:00:00 0.0153 0.1097  2.22e-06       2E-6
2010-06-08 00:00:00 0.0153 0.1097  0.70e-06       2E-6
2010-06-14 00:00:00 0.0153 0.1097  5.0e-06       2E-6
2010-06-22 00:00:00 0.0153 0.1097  2.36e-06       2E-6
2010-07-20 00:00:00 0.0153 0.1097  4.59e-06       2E-6
2010-07-26 00:00:00 0.0153 0.1097  4.14e-06       2E-6
2010-08-03 00:00:00 0.0153 0.1097  1.90e-06       2E-6
2010-08-12 00:00:00 0.0153 0.1097  2e-06       2E-6
2014-01-22 00:00:00 0.01678 0.1107  2e-06       2E-6
```

2. Magnesium Reactive Transport

shp.chem file

```
##########################################################
# FILE       : PIHM_RT CHEM INPUT FILE EXAMPLE                    #
# DEVELOPPER : Chen Bao (baochen.d.s@gmail.com                    #
##########################################################

TITLE
shp
END

RUNTIME
# runtime variables
tvd        true
# whether to use tvd in calculation the advective concentration flux
output     24
# set output interval to # hours
activity   1
# enable the correction of activity using Debye-Huckel Equaion (1) or using no correction (0)
act_coe_delay 0
```

```
# define whether to delay the calculation of activity coefficients (0) for delay and (1) for no delay
thermo     0
# whether (1) or not (0) to couple the thermo modeling of pihm
relmin     1
# whether mineral volume fraction is relative (1) or absolute (0)
effads     0
# whether (1) or not (0) to use the effective adsorption model (MIM + ADSORPTION + RT)
transport_only  0
# whether (0) or not (1) to include the reactive calculation. 0 for turn on reactions and 1 for turn off. Suitable for stable tracer transport problem.
precipitation  2
# whether (1) or not (0) precipitation will be specified.
RT_delay   2
Condensation          1.5
AvgScl     15
SUFEFF     1
END

GLOBAL
t_species    17
# total species including 1) primary speices, 2) primary minerals, 3) primary adsorptions. The number of species that are put into the condition blocks
s_species    9
# the number of species that are put into the secondary_species block.
minerals     8
# the number of species that are minerals in the condition blocks.
adsorption   0
# the number of species that are !primary! surface complexation, note that secondary surface complexation goes to secondary species
cation_exchange 1
# the nubmer of species that are !primary! cation exchange
mineral_kinetic  5
# the number of mineral kinetic reactions
aqueous_kinetic  0
# the number of aqueous kinetic reactions
diffusion    1E-5
# fixed diffusion coefficient, in cm2/s
dispersion   0.1
# fixed dispersion coefficient, in m
cementation  1
# cementation factor
temperature  25
# assumed temperature for thermo decouple mode
END

OUTPUT   1
1110
END

PUMP    1
# position  species  total_influx  influx_concentration
# unit              moles/year    mole/L
1100       Mg++     800.0          172E-6
END

INITIAL_CONDITIONS FILE shp.cini
RT      1-1070
# Assign the conditions to blocks, supported separators are "," and "-". Named condition need be specified using Condition keyword
MS      1071-1112
VF      1050
END

Condition RT
# concentrations and names of species of condition X.
```

```
# recommanded order: aqueous primary, adsorption, cation exchange, mineral
pH              4.56
HCO3-           0.28
Mg++            5.49E-4
Ca++          5.2E-4
Cl-             3.69E-5
H4SiO4          1.00E-4
K+              2.19E-5
Na+           19.0E-4
shillite      0.2845     -ssa         0.80
shchlorite      0.0690               -ssa         0.01
CO2(*g)       1.00E-3    -ssa     70.0
Dolomite      1.00E-10  -ssa     0.02
Calcite       1.00E-10  -ssa     2E-4
Kaolinite     0.0266   -ssa         1.48
Quartz          0.6199               -ssa         1.48
FeOOH           1.00E-5              -ssa         1.48
X-              5.2E-5
END

Condition MS
pH            4.48
HCO3-         0.28
Mg++          9.4E-4
Ca++          9.7E-4
Cl-           3.12E-5
H4SiO4        1.00E-4
K+            1.53E-5
Na+           18.5E-4
shillite        0.2690     -ssa     0.80
shchlorite      0.0669     -ssa     0.01
CO2(*g)       1.00E-3 -ssa          70.0
Dolomite      1.00E-10  -ssa     0.02
Calcite       0.001   -ssa     5.0E-4
Kaolinite     0.0283     -ssa     1.48
Quartz        0.6348     -ssa     1.48
FeOOH         1.00E-5  -ssa     1.48
X-              4E-5
END

Condition VF
pH            4.70
HCO3-         0.28
Mg++          12.61E-4
Ca++          12.9E-4
Cl-           3.93E-5
H4SiO4        1.00E-4
K+            2.33E-5
Na+           26.7E-4
shillite        0.4068     -ssa     0.80
shchlorite      0.0668     -ssa     0.01
CO2(*g)       1.00E-3    -ssa     70.0
Dolomite      1.00E-10  -ssa     0.02
Calcite       0.01000  -ssa     5.0E-4
Kaolinite     0.0149     -ssa     1.48
Quartz        0.5014     -ssa     1.48
FeOOH         1.00E-5  -ssa     1.48
X-              5.8E-5
END

PRECIPITATION
pH            4.3
HCO3-         8.0E-4
Mg++          0.75E-6
Ca++          2.91E-6
```

```
Cl-           1.23E-5
H4SiO4        1.00E-4
K+            1.53E-6
Na+           2.00E-6
shillite      1.00E-10    -ssa    2.5
shchlorite    1.00E-10    -ssa    0.15
CO2(*g)       1.00E-10              -ssa          70.0
Dolomite      1.00E-10  -ssa    0.02
Calcite       1.00E-10  -ssa    0.01
Kaolinite     1.00E-10    -ssa    1.48
Quartz        1.00E-10    -ssa    1.48
FeOOH         1.00E-10  -ssa    1.48
X-          1.00E-3
END


SECONDARY_SPECIES
OH-
CO2(aq)
CO3--
MgX2
MgCO3(aq)
MgCl+
MgHCO3+
CaX2
NaX
# Basis switching is not supported in this version of PIHM_RT
END

MINERALS
# rate constant log10(rate, units mol/m^2/s)
!Calcite -label default
shillite       -label default
shchlorite       -label default
CO2(*g)    -label default
Dolomite         -label default
Calcite          -label default
END
```

Abbott, M.B., Bathurst, J.C., Cunge, J.A., O'Connell, P.E., Rasmussen, J., 1986. An introduction to the European Hydrological System—Systeme Hydrologique Europeen,"SHE", 1: History and philosophy of a physically-based, distributed modelling system. Journal of hydrology 87, 45-59.
Allard, D., 1993. On the connectivity of two random set models: the truncated Gaussian and the Boolean, Geostatistics Tróia'92. Springer, pp. 467-478.
Anderson, S.P., Dietrich, W.E., Torres, R., Montgomery, D.R., Loague, K., 1997. Concentration-discharge relationships in runoff from a steep, unchanneled catchment. Water Resources Research 33, 211-225.
Anderton, S., Latron, J., Gallart, F., 2002. Sensitivity analysis and multi‐response, multi‐criteria evaluation of a physically based distributed model. Hydrological Processes 16, 333-353.
Andrews, D.M., Lin, H., Zhu, Q., Jin, L., Brantley, S.L., 2011. Hot spots and hot moments of dissolved organic carbon export and soil organic carbon storage in the Shale Hills catchment. Vadose Zone Journal 10, 943-954.
Arbogast, T., Bryant, S., Dawson, C., Saaf, F., Wang, C., Wheeler, M., 1996. Computational methods for multiphase flow and reactive transport problems arising in subsurface contaminant remediation. Journal of Computational and Applied Mathematics 74, 19-32.
Arnold, J., Soil, G., 1994. SWAT (Soil and Water Assessment Tool). Grassland, Soil and Water Research Laboratory, USDA, Agricultural Research Service.
Atchley, A.L., Navarre-Sitchler, A.K., Maxwell, R.M., 2014. The effects of physical and geochemical heterogeneities on hydro-geochemical transport and effective reaction rates. Journal of Contaminant Hydrology 165, 53-64.
Audigane, P., Gaus, I., Czernichowski-Lauriol, I., Pruess, K., Xu, T., 2007. Two-dimensional reactive transport modeling of CO2 injection in a saline aquifer at the Sleipner site, North Sea. American Journal of Science 307, 974-1008.
Aylmore, L., Sills, I., Quirk, J., 1970. Surface area of homoionic illite and montmorillonite clay minerals as measured by the sorption of nitrogen and carbon dioxide. Clays and Clay Minerals 18, 91-96.
Bachu, S., 2000. Sequestration of CO< sub> 2</sub> in geological media: criteria and approach for site selection in response to climate change. Energy Conversion and Management 41, 953-970.
Banat, I.M., 1995. Biosurfactants production and possible uses in microbial enhanced oil recovery and oil pollution remediation: a review. Bioresource Technology 51, 1-12.
Bao, C., Li, L., Shi, Y., Sullivan, P.L., Duffy, C., Brantley, S., 2015. RT-Flux-PIHM: A Hydrogeochemical Model at the Watershed Scale. Water Resources Research, under review.
Bao, C., Wu, H., Li, L., Newcomer, D., Long, P.E., Williams, K.H., 2014. Uranium Bioreduction Rates across Scales: Biogeochemical Hot Moments and Hot Spots during a Biostimulation Experiment at Rifle, Colorado. Environmental Science & Technology 48, 10116-10127.
Beisman, J., Maxwell, R., Navarre-Sitchler, A., Steefel, C., Molins, S., 2015. ParCrunchFlow: an efficient, parallel reactive transport simulation tool for physically and chemically heterogeneous saturated subsurface environments. Computational Geosciences, 1-20.
Beven, K., 1989. Changing ideas in hydrology—the case of physically-based models. Journal of hydrology 105, 157-172.
Beven, K., 2002. Towards an alternative blueprint for a physically based digitally simulated hydrologic response modelling system. Hydrological Processes 16, 189-206.
Beven, K., Binley, A., 1992. II THE FUTURE OF DISTRIBUTED MODELS: MODEL CALIBRATION AND UNCERTAINTY PREDICTION. Hydrological processes 6, 279-298.
Beven, K., Germann, P., 1982. Macropores and water flow in soils. Water resources research 18, 1311-1325.

Brandt, F., Bosbach, D., Krawczyk-Bärsch, E., Arnold, T., Bernhard, G., 2003. Chlorite dissolution in the acid pH-range: a combined microscopic and macroscopic approach. Geochimica et Cosmochimica Acta 67, 1451-1461.

Brantley, S., White, T., White, A., Sparks, D., Richter, D., Pregitzer, K., Derry, L., Chorover, J., Chadwick, O., April, R., 2006. Frontiers in exploration of the Critical Zone: Report of a workshop sponsored by the National Science Foundation, October 24–26, 2005, Univ. Delaware, Newark.

Brantley, S.L., Holleran, M.E., Jin, L., Bazilevskaya, E., 2013a. Probing deep weathering in the Shale Hills Critical Zone Observatory, Pennsylvania (USA): the hypothesis of nested chemical reaction fronts in the subsurface. Earth Surface Processes and Landforms 38, 1280-1298.

Brantley, S.L., Jin, L., Andrews, D., Holmes, G., Bhatt, M., Holleran, M., Kaiser, N., Williams, J.Z., Herndon, E., Duffy, C.J., Sullivan, P.L., 2013b. Susquehanna Shale Hills Critical Zone Observatory Stream Water Chemistry (2009). Integrated Earth Data Applications (IEDA).

Brantley, S.L., Jin, L., Andrews, D., Holmes, G., Bhatt, M., Holleran, M., Kaiser, N., Williams, J.Z., Herndon, E., Sullivan, P.L., 2013c. Susquehanna Shale Hills Critical Zone Observatory Porewater Chemistry (2009). Integrated Earth Data Applications (IEDA).

Brunet, J.-P.L., Li, L., Karpyn, Z.T., Kutchko, B.G., Strazisar, B., Bromhal, G., 2013. Dynamic Evolution of Cement Composition and Transport Properties under Conditions Relevant to Geological Carbon Sequestration. Energy & Fuels.

Campbell, F.B., Bauder, H., 1940. A rating ‐ curve method for determining silt ‐ discharge of streams. Eos, Transactions American Geophysical Union 21, 603-607.

Cao, H., Aziz, K., 2002. Performance of IMPSAT and IMPSAT-AIM models in compositional simulation, SPE Annual Technical Conference and Exhibition. Society of Petroleum Engineers.

Chanat, J.G., Rice, K.C., Hornberger, G.M., 2002. Consistency of patterns in concentration ‐ discharge plots. Water Resources Research 38, 22-21-22-10.

Chen, F., Dudhia, J., 2001. Coupling an advanced land surface-hydrology model with the Penn State-NCAR MM5 modeling system. Part I: Model implementation and sensitivity. Monthly Weather Review 129, 569-585.

Chen, J., Wheater, H., Lees, M., 2002. Identification of processes affecting stream chloride response in the Hafren catchment, mid-Wales. Journal of Hydrology 264, 12-33.

Chorover, J., Kretzschmar, R., Garcia-Pichel, F., Sparks, D.L., 2007. Soil biogeochemical processes within the critical zone. Elements 3, 321-326.

Clow, D.W., Mast, M.A., 2010. Mechanisms for chemostatic behavior in catchments: Implications for CO2 consumption by mineral weathering. Chemical Geology 269, 40-51.

Cole, D., Rapp, M., 1981. 6. Elemental cycling in forest ecosystems. Dynamic properties of forest ecosystems, 341.

Cussler, E.L., 2009. Diffusion: mass transfer in fluid systems. Cambridge university press.

DeWalle, D., Pionke, H., 1994. Streamflow generation on a small agricultural catchment during autumn recharge: II. Stormflow periods. Journal of Hydrology 163, 23-42.

Dobrowolski, J.P., Caldwell, M.M., Richards, J.H., 1990. Basin hydrology and plant root systems, Plant Biology of the Basin and Range. Springer, pp. 243-292.

Donigian Jr, A., Bicknell, B., Imhoff, J., Singh, V., 1995. Hydrological Simulation Program-Fortran (HSPF). Computer models of watershed hydrology., 395-442.

Douglas, I., Spencer, T., Greer, T., Bidin, K., Sinun, W., Meng, W.W., 1992. The impact of selective commercial logging on stream hydrology, chemistry and sediment loads in the Ulu Segama rain forest, Sabah, Malaysia. Philosophical Transactions of the Royal Society of London. Series B: Biological Sciences 335, 397-406.

Duffy, C., 2013. CZO Dataset: Shale Hills - Precipitation (2006-2013). Retrieved 24 Apr 2015 from http://criticalzone.org/shale-hills/data/dataset/2556/.

Duffy, C., Davis, K., Kane, T., Boyer, E., 2009. The Shale Hills Critical Zone Observatory for Embedded Sensing and Simulation, EGU General Assembly Conference Abstracts, p. 12178.
Duffy, C., Kumar, M., Bhatt, G., Leonard, L., Yu, X., Shi, Y., Davis, K., Holmes, G., 2010. Watershed reanalysis: data assimilation from strip charts to embedded sensor networks, AGU Fall Meeting Abstracts, p. 06.
Duffy, C., Shi, Y., Davis, K., Slingerland, R., Li, L., Sullivan, P.L., Goddéris, Y., Brantley, S.L., 2014. Designing a Suite of Models to Explore Critical Zone Function. Procedia Earth and Planetary Science 10, 7-15.
Duffy, C.J., Cusumano, J., 1998. A low‐dimensional model for concentration‐discharge dynamics in groundwater stream systems. Water Resources Research 34, 2235-2247.
Eriksson, E., 1955. Air borne salts and the chemical composition of river waters. Tellus 7, 243-250.
Ertekin, T., Abou-Kassem, J.H., King, G.R., 2001. Basic applied reservoir simulation. Richardson, TX: Society of Petroleum Engineers.
Evans, C., Davies, T.D., 1998. Causes of concentration/discharge hysteresis and its potential as a tool for analysis of episode hydrochemistry. Water Resources Research 34, 129-137.
Eyring, H., 1935. The activated complex in chemical reactions. The Journal of Chemical Physics 3, 107.
Fang, Y., Yabusaki, S.B., Morrison, S.J., Amonette, J.P., Long, P.E., 2009. Multicomponent reactive transport modeling of uranium bioremediation field experiments. Geochimica et Cosmochimica Acta 73, 6029-6051.
Ferguson, R., 1986. River loads underestimated by rating curves. Water Resources Research 22, 74-76.
Flueckinger, L.A., 1969. Geology of a Portion of the Allensville Quadrangle, Centre and Huntingdon Counties, Pennsylvania. Commonwealth of Pennsylvania, State Planning Board, Bureau of Topographic and Geologic Survey.
Frye, E., Bao, C., Li, L., Blumsack, S., 2012. Environmental controls of cadmium desorption during CO2 leakage. Environmental science & technology 46, 4388-4395.
Gan, T.Y., Gusev, Y., Burges, S.J., Nasonova, O., Andréassian, V., Hall, A., Chahinian, N., Schaake, J., 2006. Performance comparison of a complex physics-based land surface model and a conceptual, lumped-parameter hydrological model at the basin-scale. Large sample basin experiments for hydrological model parameterization: results of the model parameter experiment (MOPEX), 196-208.
Gautelier, M., Oelkers, E.H., Schott, J., 1999. An experimental study of dolomite dissolution rates as a function of pH from− 0.5 to 5 and temperature from 25 to 80 C. Chemical Geology 157, 13-26.
Gelhar, L.W., Welty, C., Rehfeldt, K.R., 1992. A critical review of data on field‐scale dispersion in aquifers. Water resources research 28, 1955-1974.
Gelhar, L.W., Wilson, J.L., 1974. Ground‐Water Quality Modelinga. Groundwater 12, 399-408.
Goddéris, Y., Brantley, S.L., 2013. Earthcasting the future Critical Zone. Elem. Sci. Anth. 1, 000019.
Goddéris, Y., Williams, J.Z., Schott, J., Pollard, D., Brantley, S.L., 2010. Time evolution of the mineralogical composition of Mississippi Valley loess over the last 10kyr: Climate and geochemical modeling. Geochimica et Cosmochimica Acta 74, 6357-6374.
Godsey, S.E., Kirchner, J.W., Clow, D.W., 2009. Concentration–discharge relationships reflect chemostatic characteristics of US catchments. Hydrological Processes 23, 1844-1864.
Goldberg, A., Higuchi, W., 1969. Mechanisms of interphase transport II: Theoretical considerations and experimental evaluation of interfacially controlled transport in solubilized systems. Journal of pharmaceutical sciences 58, 1341-1352.

Goldberg, A., Higuchi, W., Ho, N., Zografi, G., 1967. Mechanisms of interphase transport I. Theoretical considerations of diffusion and interfacial barriers in transport of solubilized systems. Journal of pharmaceutical sciences 56, 1432-1437.
Gottardi, G., Venutelli, M., 1993. A control-volume finite-element model for two-dimensional overland flow. Advances in water resources 16, 277-284.
Gupta, A.D., Lake, L., Pope, G., Sepehrnoori, K., King, M., 1991. High-resolution monotonic schemes for reservoir fluid flow simulation. In Situ;(United States) 15.
Gupta, H., Bastidas, L., Sorooshian, S., Shuttleworth, W., Yang, Z., 1999. Parameter estimation of a land surface scheme using multicriteria methods. Journal of Geophysical Research 104, 19491-19503.
Hargreaves, G.H., Samani, Z.A., 1982. Estimating potential evapotranspiration. Journal of the Irrigation and Drainage Division 108, 225-230.
Hasenmueller, E., Jin, L., Smith, L., Kaye, M., Lin, H., Brantley, S., Kaye, J., 2013. Depth and Topographic Controls on Soil Gas Concentrations and Fluxes in a Small Temperate Watershed, AGU Fall Meeting Abstracts, p. 0876.
Hedin, L.O., Armesto, J.J., Johnson, A.H., 1995. Patterns of nutrient loss from unpolluted, old-growth temperate forests: evaluation of biogeochemical theory. Ecology 76, 493-509.
Helgeson, H.C., Murphy, W.M., Aagaard, P., 1984. Thermodynamic and kinetic constraints on reaction rates among minerals and aqueous solutions. II. Rate constants, effective surface area, and the hydrolysis of feldspar. Geochimica et Cosmochimica Acta 48, 2405-2432.
Herndon, E., Dere, A., Sullivan, P., Norris, D., Reynolds, B., Brantley, S., 2015. Biotic controls on solute distribution and transport in headwater catchments. Hydrology and Earth System Sciences Discussions 12, 213-243.
Hindmarsh, A.C., Brown, P.N., Grant, K.E., Lee, S.L., Serban, R., Shumaker, D.E., Woodward, C.S., 2005. SUNDIALS: Suite of nonlinear and differential/algebraic equation solvers. ACM Transactions on Mathematical Software (TOMS) 31, 363-396.
Holder, A.W., Bedient, P.B., Dawson, C.N., 2000. FLOTRAN, a three-dimensional ground water model, with comparisons to analytical solutions and other models. Advances in Water Resources 23, 517-530.
Hooper, R.P., Christophersen, N., Peters, N.E., 1990. Modelling streamwater chemistry as a mixture of soilwater end-members—An application to the Panola Mountain catchment, Georgia, USA. Journal of Hydrology 116, 321-343.
Jacques, D., Šimůnek, J., Mallants, D., van Genuchten, M.T., 2006. Operator-splitting errors in coupled reactive transport codes for transient variably saturated flow and contaminant transport in layered soil profiles. Journal of contaminant hydrology 88, 197-218.
James, A.L., Roulet, N.T., 2007. Investigating hydrologic connectivity and its association with threshold change in runoff response in a temperate forested watershed. Hydrological Processes 21, 3391-3408.
Jamieson-Hanes, J.H., Amos, R.T., Blowes, D.W., 2012. Reactive Transport Modeling of Chromium Isotope Fractionation during Cr(VI) Reduction. Environmental Science & Technology 46, 13311-13316.
Jawahar, P., Kamath, H., 2000. A high-resolution procedure for Euler and Navier–Stokes computations on unstructured grids. Journal of Computational Physics 164, 165-203.
Jencso, K.G., McGlynn, B.L., Gooseff, M.N., Wondzell, S.M., Bencala, K.E., Marshall, L.A., 2009. Hydrologic connectivity between landscapes and streams: Transferring reach‐ and plot‐scale understanding to the catchment scale. Water Resources Research 45.
Jin, L., Andrews, D.M., Holmes, G.H., Lin, H., Brantley, S.L., 2011a. Opening the “black box”: Water chemistry reveals hydrological controls on weathering in the Susquehanna Shale Hills Critical Zone Observatory. Vadose Zone Journal 10, 928-942.

Jin, L., Ogrinc, N., Yesavage, T., Hasenmueller, E.A., Ma, L., Sullivan, P.L., Kaye, J., Duffy, C., Brantley, S.L., 2014. The CO< sub> 2</sub> consumption potential during gray shale weathering: Insights from the evolution of carbon isotopes in the Susquehanna Shale Hills critical zone observatory. Geochimica et Cosmochimica Acta 142, 260-280.
Jin, L., Ravella, R., Ketchum, B., Bierman, P.R., Heaney, P., White, T., Brantley, S.L., 2010. Mineral weathering and elemental transport during hillslope evolution at the Susquehanna/Shale Hills Critical Zone Observatory. Geochimica et Cosmochimica Acta 74, 3669-3691.
Jin, L., Rother, G., Cole, D.R., Mildner, D.F., Duffy, C.J., Brantley, S.L., 2011b. Characterization of deep weathering and nanoporosity development in shale—A neutron study. American Mineralogist 96, 498-512.
Johnson, D., Richter, D., Lovett, G., Lindberg, S., 1985. The effects of atmospheric deposition on potassium, calcium, and magnesium cycling in two deciduous forests. Canadian Journal of Forest Research 15, 773-782.
Johnson, J.W., Nitao, J.J., Knauss, K.G., 2004. Reactive transport modeling of CO2 storage in saline aquifers to elucidate fundamental processes, trapping mechanisms and sequestration partitioning. Geological storage of carbon dioxide 233, 107-128.
Johnson, N.M., Likens, G.E., Bormann, F.H., Fisher, D.W., Pierce, R.S., 1969. A Working Model for the Variation in Stream Water Chemistry at the Hubbard Brook Experimental Forest, New Hampshire. Water Resources Research 5, 1353-1363.
Jordan, D., Stecker, J., Cacnio-Hubbard, V., Li, F., Gantzer, C., Brown, J., 1997. Earthworm activity in no-tillage and conventional tillage systems in Missouri soils: a preliminary study. Soil Biology and Biochemistry 29, 489-491.
Kirchner, J.W., 2003. A double paradox in catchment hydrology and geochemistry. Hydrological Processes 17, 871-874.
Kirchner, J.W., 2006. Getting the right answers for the right reasons: Linking measurements, analyses, and models to advance the science of hydrology. Water Resources Research 42.
Kirchner, J.W., Feng, X., Neal, C., 2000. Fractal stream chemistry and its implications for contaminant transport in catchments. Nature 403, 524-527.
Kirchner, J.W., Feng, X., Neal, C., 2001. Catchment-scale advection and dispersion as a mechanism for fractal scaling in stream tracer concentrations. Journal of Hydrology 254, 82-101.
Kirkner, D.J., Reeves, H., 1988. Multicomponent mass transport with homogeneous and heterogeneous chemical reactions: effect of the chemistry on the choice of numerical algorithm: 1. Theory. Water Resources Research 24, 1719-1729.
Köhler, S.J., Bosbach, D., Oelkers, E.H., 2005. Do clay mineral dissolution rates reach steady state? Geochimica et cosmochimica acta 69, 1997-2006.
Köhler, S.J., Dufaud, F., Oelkers, E.H., 2003. An experimental study of illite dissolution kinetics as a function of pH from 1.4 to 12.4 and temperature from 5 to 50 C. Geochimica et Cosmochimica Acta 67, 3583-3594.
Kollet, S.J., Maxwell, R.M., 2006. Integrated surface-groundwater flow modeling: A free-surface overland flow boundary condition in a parallel groundwater flow model. Advances in Water Resources 29, 945-958.
Kumar, M., Bhatt, G., Duffy, C.J., 2009a. An efficient domain decomposition framework for accurate representation of geodata in distributed hydrologic models. International Journal of Geographical Information Science 23, 1569-1596.
Kumar, M., Duffy, C.J., Salvage, K.M., 2009b. A Second-Order Accurate, Finite Volume–Based, Integrated Hydrologic Modeling (FIHM) Framework for Simulation of Surface and Subsurface Flow All rights reserved. No part of this periodical may be reproduced or transmitted in any form or by any means, electronic or mechanical, including photocopying, recording, or any information

storage and retrieval system, without permission in writing from the publisher. Vadose Zone J. 8, 873-890.
Lamb, D., Bowersox, V., 2000. The national atmospheric deposition program: an overview. Atmospheric Environment 34, 1661-1663.
Lasaga, A.C., 1984. Chemical kinetics of water-rock interactions. Journal of Geophysical Research 89, 4009-4025.
Lasaga, A.C., 1998. Kinetic theory in the earth sciences. Princeton University Press, Princeton.
Li, L., Gawande, N., Kowalsky, M.B., Steefel, C.I., Hubbard, S.S., 2011. Physicochemical heterogeneity controls on uranium bioreduction rates at the field scale. Environmental Science & Technology 45, 9959-9966.
Li, L., Salehikhoo, F., Brantley, S.L., Heidari, P., 2014. Spatial zonation limits magnesite dissolution in porous media. Geochimica Et Cosmochimica Acta 126, 555-573.
Li, L., Steefel, C.I., Kowalsky, M.B., Englert, A., Hubbard, S.S., 2010. Effects of physical and geochemical heterogeneities on mineral transformation and biomass accumulation during biostimulation experiments at Rifle, Colorado. Journal of Contaminant Hydrology 112, 45-63.
Li, L., Steefel, C.I., Williams, K.H., Wilkins, M.J., Hubbard, S.S., 2009. Mineral transformation and biomass accumulation during uranium bioremediation at Rifle, Colorado. Environ. Sci. Technol. 43, 5429-5435. doi: 5410.1021/es900016v.
Li, S., Duffy, C.J., 2012. Fully-Coupled Modeling of Shallow Water Flow and Pollutant Transport on Unstructured Grids. Procedia Environmental Sciences 13, 2098-2121.
Lichtner, P.C., 1985. Continuum Model for Simultaneous Chemical-Reactions and Mass-Transport in Hydrothermal Systems. Geochimica Et Cosmochimica Acta 49, 779-800.
Lin, H., 2006. Temporal stability of soil moisture spatial pattern and subsurface preferential flow pathways in the Shale Hills Catchment. Vadose Zone Journal 5, 317-340.
Lockwood, P., McGarity, J., Charley, J., 1995. Measurement of chemical weathering rates using natural chloride as a tracer. Geoderma 64, 215-232.
Lu, C., Lichtner, P.C., 2005. PFLOTRAN: Massively parallel 3-D simulator for CO2 sequestration in geologic media, DOE-NETL Fourth Annual Conference on Carbon Capture and Sequestration.
Ma, L., Chabaux, F., Pelt, E., Blaes, E., Jin, L., Brantley, S., 2010. Regolith production rates calculated with uranium-series isotopes at Susquehanna/Shale Hills Critical Zone Observatory. Earth and Planetary Science Letters 297, 211-225.
Maher, K., Chamberlain, C., 2014. Hydrologic regulation of chemical weathering and the geologic carbon cycle. science 343, 1502-1504.
Maxwell, R.M., Miller, N.L., 2005. Development of a coupled land surface and groundwater model. Journal of Hydrometeorology 6, 233-247.
Mayer, K.U., Frind, E.O., Blowes, D.W., 2002. Multicomponent reactive transport modeling in variably saturated porous media using a generalized formulation for kinetically controlled reactions. Water Resources Research 38, 1174.
McDonnell, J., Sivapalan, M., Vaché, K., Dunn, S., Grant, G., Haggerty, R., Hinz, C., Hooper, R., Kirchner, J., Roderick, M., 2007. Moving beyond heterogeneity and process complexity: A new vision for watershed hydrology. Water Resources Research 43.
McGuire, K.J., McDonnell, J.J., 2010. Hydrological connectivity of hillslopes and streams: Characteristic time scales and nonlinearities. Water Resources Research 46.
Michaelides, K., Chappell, A., 2009. Connectivity as a concept for characterising hydrological behaviour. Hydrological Processes 23, 517-522.
Moore, D.M., Reynolds, R.C., 1989. X-ray Diffraction and the Identification and Analysis of Clay Minerals. Oxford university press Oxford.

Moore, J., Lichtner, P.C., White, A.F., Brantley, S.L., 2012. Using a reactive transport model to elucidate differences between laboratory and field dissolution rates in regolith. Geochimica Et Cosmochimica Acta 93, 235-261.
Moriasi, D., Arnold, J., Van Liew, M., Bingner, R., Harmel, R., Veith, T., 2007. Model evaluation guidelines for systematic quantification of accuracy in watershed simulations. Trans. ASABE 50, 885-900.
Morrice, J.A., Valett, H., Dahm, C.N., Campana, M.E., 1997. Alluvial characteristics, groundwater–surface water exchange and hydrological retention in headwater streams. Hydrological Processes 11, 253-267.
Navarre-Sitchler, A., Brantley, S., 2007. Basalt weathering across scales. Earth and Planetary Science Letters 261, 321-334.
Navarre-Sitchler, A.K., Maxwell, R.M., Siirila, E.R., Hammond, G.E., Lichtner, P.C., 2013. Elucidating geochemical response of shallow heterogeneous aquifers to CO2 leakage using high-performance computing: Implications for monitoring of CO2 sequestration. Advances in Water Resources 53, 45-55.
Neal, C., Hill, T., Alexander, S., Reynolds, B., Hill, S., Dixon, A.J., Harrow, M., Neal, M., Smith, C.J., 1997. Stream water quality in acid sensitive UK upland areas; an example of potential water quality remediation based on groundwater manipulation. Hydrology and Earth System Sciences Discussions 1, 185-196.
Nielsen, D., Biggar, J., 1986. Water flow and solute transport processes in the unsaturated zone. Water resources research 22, 89S-108S.
Pan, H.-L., Mahrt, L., 1987. Interaction between soil hydrology and boundary-layer development. Boundary-Layer Meteorology 38, 185-202.
Panday, S., Huyakorn, P.S., 2004. A fully coupled physically-based spatially-distributed model for evaluating surface/subsurface flow. Advances in water Resources 27, 361-382.
Parkhurst, D.L., Stollenwerk, K.G., Colman, J.A., 2003. Reactive-transport simulation of phosphorus in the sewage plume at the Massachusetts Military Reservation, Cape Cod, Massachusetts. US Department of the Interior, US Geological Survey.
Penman, H.L., 1948. Natural evaporation from open water, bare soil and grass, Proceedings of the Royal Society of London A: Mathematical, Physical and Engineering Sciences. The Royal Society, pp. 120-145.
Perrochet, P., Bérod, D., 1993. Stability of the standard Crank-Nicolson-Galerkin Scheme applied to the diffusion-convection equation: Some new insights. Water Resources Research 29, 3291-3297.
Person, M., Raffensperger, J.P., Ge, S., Garven, G., 1996. Basin‐scale hydrogeologic modeling. Reviews of Geophysics 34, 61-87.
Peters, N.E., Ratcliffe, E.B., Tranter, M., 1998. Tracing solute mobility at the Panola Mountain Research Watershed, Georgia, USA: variations in Na^+, Cl^-, and H~ 4SiO~ 4 concentrations. IAHS PUBLICATION, 483-490.
Pionke, H., Hoover, J., Schnabel, R., Gburek, W., Urban, J., Rogowski, A., 1988. Chemical‐hydrologic interactions in the near‐stream zone. Water Resources Research 24, 1101-1110.
Pitzer, K.S., 1977. Electrolyte theory-improvements since Debye and Hückel. Accounts of Chemical Research 10, 371-377.
Pokhrel, P., Gupta, H.V., 2010. On the use of spatial regularization strategies to improve calibration of distributed watershed models. Water Resources Research 46.
Pokrovsky, O.S., Golubev, S.V., Schott, J., 2005. Dissolution kinetics of calcite, dolomite and magnesite at 25° C and 0 to 50 atm< i> p</i> CO< sub> 2</sub>. Chemical Geology 217, 239-255.

Polkowska, Ż., Astel, A., Walna, B., Małek, S., Mędrzycka, K., Górecki, T., Siepak, J., Namieśnik, J., 2005. Chemometric analysis of rainwater and throughfall at several sites in Poland. Atmospheric Environment 39, 837-855.
Priestley, C., Taylor, R., 1972. On the assessment of surface heat flux and evaporation using large-scale parameters. Monthly weather review 100, 81-92.
Qiao, C., Li, L., Johns, R., Xu, J., 2014a. Compositional Modeling of Reaction-Induced Injectivity Alteration During CO2 Flooding in Carbonate Reservoirs.
Qiao, C., Li, L., Johns, R., Xu, J., 2014b. A Mechanistic Model for Wettability Alteration by Chemically Tuned Water Flooding in Carbonate Reservoirs.
Qu, Y., Duffy, C.J., 2007. A semidiscrete finite volume formulation for multiprocess watershed simulation. Water Resources Research 43, W08419.
Quinn, P., Beven, K., Chevallier, P., Planchon, O., 1991. The prediction of hillslope flow paths for distributed hydrological modelling using digital terrain models. Hydrological processes 5, 59-79.
Reddy, J.N., 1993. An introduction to the finite element method. McGraw-Hill New York.
Runkel, R.L., Kimball, B.A., 2002. Evaluating remedial alternatives for an acid mine drainage stream: application of a reactive transport model. Environmental science & technology 36, 1093-1101.
Saito, H., Šimůnek, J., Mohanty, B.P., 2006. Numerical analysis of coupled water, vapor, and heat transport in the vadose zone. Vadose Zone Journal 5, 784-800.
Salehikhoo, F., Li, L., 2015. The role of magnesite spatial distribution patterns in determining dissolution rates: When do they matter? Geochimica et Cosmochimica Acta 155, 107-121.
Santhi, C., Arnold, J.G., Williams, J.R., Dugas, W.A., Srinivasan, R., Hauck, L.M., 2001. VALIDATION OF THE SWAT MODEL ON A LARGE RWER BASIN WITH POINT AND NONPOINT SOURCES1. Wiley Online Library.
Scheibe, T.D., Mahadevan, R., Fang, Y., Garg, S., Long, P.E., Lovley, D.R., 2009. Coupling a genome-scale metabolic model with a reactive transport model to describe in situ uranium bioremediation. Microbial Biotechnology 2, 274-286.
Shah, D.O., 1977. Improved oil recovery by surfactant and polymer flooding. Elsevier.
Sherman, L.A., Barak, P., 2000. Solubility and Dissolution Kinetics of Dolomite in Ca–Mg–HCO/CO Solutions at 25° C and 0.1 MPa Carbon Dioxide. Soil Science Society of America Journal 64, 1959-1968.
Shi, Y., Baldwin, D.C., Davis, K.J., Yu, X., Duffy, C.J., Lin, H., 2015. Simulating high resolution soil moisture patterns in the shale hills watershed using a land surface hydrologic model. Hydrological Processes, n/a-n/a.
Shi, Y., Davis, K.J., Duffy, C.J., Yu, X., 2013a. Development of a Coupled Land Surface Hydrologic Model and Evaluation at a Critical Zone Observatory. Journal of Hydrometeorology 14, 1401-1420.
Shi, Y., Davis, K.J., Duffy, C.J., Yu, X., 2013b. Development of a Coupled Land Surface Hydrologic Model and Evaluation at a Critical Zone Observatory. Journal of Hydrometeorology 14.
Shi, Y., Davis, K.J., Zhang, F., Duffy, C.J., 2013c. Evaluation of the Parameter Sensitivities of a Coupled Land Surface Hydrologic Model at a Critical Zone Observatory. Journal of Hydrometeorology.
Shi, Y., Davis, K.J., Zhang, F., Duffy, C.J., Yu, X., 2014. Parameter estimation of a physically based land surface hydrologic model using the ensemble Kalman filter: A synthetic experiment. Water Resources Research 50, 706-724.

Šimůnek, J., Jarvis, N.J., Van Genuchten, M.T., Gärdenäs, A., 2003. Review and comparison of models for describing non-equilibrium and preferential flow and transport in the vadose zone. Journal of Hydrology 272, 14-35.
Singh, V.P., 1995. Computer models of watershed hydrology. Water Resources Publications.
Stallard, R.F., 1998. Terrestrial sedimentation and the carbon cycle: Coupling weathering and erosion to carbon burial. Global Biogeochemical Cycles 12, 231-257.
Stallard, R.F., Murphy, S.F., 2014. A Unified Assessment of Hydrologic and Biogeochemical Responses in Research Watersheds in Eastern Puerto Rico Using Runoff–Concentration Relations. Aquatic Geochemistry 20, 115-139.
Steefel, C.I., 2008. CrunchFlow. Software for Modeling Multicomponent Reactive Flow and Transport. User's Manual. Earth Sciences Division, Berkeley (USA), Lawrence Berkeley National Laboratory, 90pp.
Steefel, C.I., Appelo, C.A.J., Arora, B., Jacques, D., Kalbacher, T., Kolditz, O., Lagneau, V., Lichtner, P.C., Mayer, K.U., Meeussen, J.C.L., Molins, S., Moulton, D., Shao, H., Šimůnek, J., Spycher, N., Yabusaki, S.B., Yeh, G.T., 2014. Reactive transport codes for subsurface environmental simulation. Computational Geosciences, 1-34.
Steefel, C.I., DePaolo, D.J., Lichtner, P.C., 2005. Reactive transport modeling: An essential tool and a new research approach for the Earth sciences. Earth and Planetary Science Letters 240, 539-558.
Steefel, C.I., Lasaga, A.C., 1994. A Coupled Model for Transport of Multiple Chemical-Species and Kinetic Precipitation Dissolution Reactions with Application to Reactive Flow in Single-Phase Hydrothermal Systems. American Journal of Science 294, 529-592.
Stenback, G.A., Crumpton, W.G., Schilling, K.E., Helmers, M.J., 2011. Rating curve estimation of nutrient loads in Iowa rivers. Journal of Hydrology 396, 158-169.
Svensson, T., Lovett, G.M., Likens, G.E., 2012. Is chloride a conservative ion in forest ecosystems? Biogeochemistry 107, 125-134.
Tang, G., Watson, D.B., Wu, W.-M., Schadt, C.W., Parker, J.C., Brooks, S.C., 2013. U (VI) Bioreduction with Emulsified Vegetable Oil as the Electron Donor–Model Application to a Field Test. Environmental science & technology 47, 3218-3225.
Tang, Y., Reed, P., Wagener, T., 2006. How effective and efficient are multiobjective evolutionary algorithms at hydrologic model calibration? Hydrology and Earth System Sciences Discussions 10, 289-307.
TDEP, 2015. TDEP - Total Deposition Science Committee. National Atmospheric Deposition Program.
Thomas, E.M., Lin, H., Duffy, C.J., Sullivan, P.L., Holmes, G.H., Brantley, S.L., Jin, L., 2013. Spatiotemporal patterns of water stable isotope compositions at the Shale Hills Critical Zone Observatory: Linkages to subsurface hydrologic processes. Vadose Zone Journal 12.
Tockner, K., Pennetzdorfer, D., Reiner, N., Schiemer, F., Ward, J., 1999. Hydrological connectivity, and the exchange of organic matter and nutrients in a dynamic river–floodplain system (Danube, Austria). Freshwater Biology 41, 521-535.
Toro, E.F., 1992. Riemann problems and the WAF method for solving the two-dimensional shallow water equations. Philosophical Transactions of the Royal Society of London A: Mathematical, Physical and Engineering Sciences 338, 43-68.
Van der Lee, J., Ledoux, E., De Marsily, G., 1992. Modeling of colloidal uranium transport in a fractured medium. Journal of Hydrology 139, 135-158.
Van Genuchten, M.T., 1980. A closed-form equation for predicting the hydraulic conductivity of unsaturated soils. Soil science society of America journal 44, 892-898.

van Meerveld, I.T., McDonnell, J.J., 2005. Comment to “Spatial correlation of soil moisture in small catchments and its relationship to dominant spatial hydrological processes, Journal of Hydrology 286: 113–134”. Journal of Hydrology 303, 307-312.

VanderKwaak, J.E., Loague, K., 2001. Hydrologic‐response simulations for the R‐5 catchment with a comprehensive physics‐based model. Water Resources Research 37, 999-1013.

Voss, C.I., 1984. A finite-element simulation model for saturated-unsaturated, fluid-density-dependent ground-water flow with energy transport or chemically-reactive single-species solute transport. US Geological Survey.

Walsh, M., Bryant, S., Schechter, R., Lake, L., 1984. Precipitation and dissolution of solids attending flow through porous media. AIChE Journal 30, 317-328.

Western, A.W., Blöschl, G., Grayson, R.B., 2001. Toward capturing hydrologically significant connectivity in spatial patterns. Water Resources Research 37, 83-97.

Western, A.W., Zhou, S.-L., Grayson, R.B., McMahon, T.A., Blöschl, G., Wilson, D.J., 2004. Spatial correlation of soil moisture in small catchments and its relationship to dominant spatial hydrological processes. Journal of Hydrology 286, 113-134.

White, A.F., Brantley, S.L., 2003. The effect of time on the weathering of silicate minerals: why do weathering rates differ in the laboratory and field? Chemical Geology 202, 479-506.

White, M.D., McGrail, B.P., 2005. Stomp (subsurface transport over multiple phase) version 1.0 addendum: Eckechem equilibrium-conservationkinetic equation chemistry and reactive transport. Pacific Northwest National Laboratory, Richland, Washington.

White, M.D., Oostrom, M., 2000. STOMP: Subsurface Transport Over Multiple Phases (Version 2.0): Theory Guide, Richland, WA.

Wolery, T.J., 1992. EQ3/6: A software package for geochemical modeling of aqueous systems: Package overview and installation guide (version 7.0). Lawrence Livermore National Laboratory Livermore, CA.

Wu, W.M., Carley, J., Fienen, M., Mehlhorn, T., Lowe, K., Nyman, J., Luo, J., Gentile, M.E., Rajan, R., Wagner, D., 2006. Pilot-scale in situ bioremediation of uranium in a highly contaminated aquifer. 1. Conditioning of a treatment zone. Environmental Science & Technology 40, 3978-3985.

Xu, T., Samper, J., Ayora, C., Manzano, M., Custodio, E., 1999. Modeling of non-isothermal multi-component reactive transport in field scale porous media flow systems. Journal of Hydrology 214, 144-164.

Xu, T., Sonnenthal, E., Spycher, N., Pruess, K., 2008. TOUGHREACT User's Guide: A Simulation Program for Non-isothermal Multiphase Reactive Geochemical Transport in Variably Saturated Geologic Media, V1. 2.1. Ernest Orlando Lawrence Berkeley National Laboratory, Berkeley, CA (US).

Xu, T., White, S., Pruess, K., Brimhall, G., 2000. Modeling of Pyrite Oxidation in Saturated and Unsaturated Subsurface Flow Systems. Transport in Porous Media 39, 25-56.

Xu, T.F., Apps, J.A., Pruess, K., 2003. Reactive geochemical transport simulation to study mineral trapping for CO2 disposal in deep arenaceous formations. Journal of Geophysical Research-Solid Earth 108.

Yabusaki, S.B., Fang, Y., Williams, K.H., Murray, C.J., Ward, A.L., Dayvault, R.D., Waichler, S.R., Newcomer, D.R., Spane, F.A., Long, P.E., 2011. Variably saturated flow and multicomponent biogeochemical reactive transport modeling of a uranium bioremediation field experiment. Journal of contaminant hydrology 126, 271-290.

Yang, J., Li, B., Shiping, L., 2000. A large weighing lysimeter for evapotranspiration and soil‐water‐groundwater exchange studies. Hydrological processes 14, 1887-1897.

Yeh, G., Sun, J., Jardine, P., Burgos, W., Fang, Y., Li, M., Siegel, M., 2004. HYDROGEOCHEM 5.0: A three-dimensional model of coupled fluid flow, thermal transport, and hydrogeochemical transport through variably saturated conditions. Version 5.0. ORNL/TM-2004/107, Oak Ridge National Laboratory, Oak Ridge, TN 37831.

Yeh, G., Tripathi, V., 1989. A critical evaluation of recent developments in hydrogeochemical transport models of reactive multichemical components. Water resources research 25, 93-108.

Zachara, J.M., Smith, S.C., Liu, C., McKinley, J.P., Serne, R.J., Gassman, P.L., 2002. Sorption of Cs+ to micaceous subsurface sediments from the Hanford site, USA. Geochimica et Cosmochimica Acta 66, 193-211.

Zoppou, C., Roberts, S., 1999. Catastrophic collapse of water supply reservoirs in urban areas. Journal of Hydraulic Engineering 125, 686-695.

Zysset, A., Stauffer, F., Dracos, T., 1994. Modeling of chemically reactive groundwater transport. Water Resources Research 30, 2217-2228.

VITA

Chen Bao

Education

The Pennsylvania State University University Park, PA Aug. 2011-May. 2016

Ph.D. candidate, Petroleum and Natural Gas Engineering, Minor, Computational Science

Peking University Peking University

M.S, Environmental Sciences Jul. 2011

B.S, Chemistry Jul. 2008

Experiences

Teaching and Research Assistant Department of Energy and Mineral Engineering

Awards

EMS Centennial Research Travel Award Graduate Merit Award

Selected Conference Talks and Publications

* Bao, C., Li, L., Shi, Y., Sullivan, P., Duffy, C., Brantley, S., RT-Flux-PIHM: A Model Integrating Hydrological, Land Surface Interactions, and Reactive Transport Processes at the Watershed Scale. Submitted to Water Resources Research, 2015

* Bao, C., Wu, H., Li, L., Williams, K., Steefel, C., Uranium Bioreduction Rates across Scales: Biogeochemical Hot Moments and Hot Spots during a Biostimulation Experiment at Rifle, Colorado Journal of Environmental Science and Technology,(2014).

* Bao, C., Li, L., Shi, Y., Qiao, C., Sullivan, P., Brantley, S., Duffy, C., Understanding the hydrological controls on the water chemistry at the watershed scale using an integrated hydro-thermo-geochemical model PIHM-RT. American Geophysical Union Fall Meeting, (2013)

* Qiao, C., Li, L., Bao, C., Hu, X., Johns, R., Xu, J., Development of a New and Fast Linear Solver for Multi-component Reactive Transport Simulation. American Geophysical Union Fall Meeting, (2013)

* Frye, E., Bao, C., Li, L., Blumsack, S. Environmental Controls on Cadmium Desorption during CO2 Leakage. Journal of Environmental Science and Technology (2012)